Ph.D. Dissertation of Engineering

Modulation of Ion Dynamics in Ionic Artificial Synapses via Interfacial Dipole Engineering

계면 쌍극자에 의한 이온 작동 인공 시냅스에서의 이온 동역학 제어

February 2025

Program in Nano Science and Technology
Graduate School of Convergence Science and Technology
Seoul National University

Minho Jin

Modulation of Ion Dynamics in Ionic Artificial Synapses via Interfacial Dipole Engineering

Advisor: Youn Sang Kim

Submitting a Ph.D. Dissertation of Engineering

January 2025

Program in Nano Science and Technology
Graduate School of Convergence Science and Technology
Seoul National University

Minho Jin

Confirming the Ph.D. Dissertation written by
Minho Jin

January 2025

Chair ______________________(Seal)
Vice Chair ______________________(Seal)
Examiner ______________________(Seal)
Examiner ______________________(Seal)
Examiner ______________________(Seal)

Abstract

Numerous studies have highlighted electrolyte-gated transistors (EGTs) as a promising candidate for artificial synapses in analog neuromorphic computing due to their exceptional characteristics, such as fast ion response, low energy consumption, and applicability to flexible electronics. However, EGTs face a critical limitation as artificial synapses due to abrupt changes in ion movement under instantaneously applied electric fields. Their inherent nature causes conventional EGTs to exhibit poor long-term synaptic plasticity and nonlinear/asymmetric conductance updates, hindering their practical application as artificial synapses. Therefore, addressing the inherent issue in EGTs is necessary through a comprehensive understanding of electrostatic interactions for precisely modulating the ion dynamics. Herein, the novel methods are introduced to precisely control ion dynamics through coulombic interactions with cations by incorporating an interlayer with dipoles at the channel/electrolyte interface in EGTs. Organic materials with dipole moments, capable of coulombic interactions with cations, are used as the interlayer; (i) fluorinated self-assembled monolayer (F-SAM) and (ii) ferroelectric polymer.

First, F-SAM is introduced as an ion receptor, inducing strong ion-dipole interactions between cations and the negatively charged F-SAM at the channel/electrolyte interface in EGTs. With the incorporation of F-SAM, cations can be effectively trapped at the interface, allowing the EGTs to maintain nearly linear, tunable multimodal conductance states. Electrical and chemical analyses confirm that fluoroalkyl chains enable sequential ion trapping at the channel-electrolyte interface through Coulombic attraction between cations and fluorocarbons. Consequently, the electrical retention of EGTs with F-SAM is enhanced, resulting in stable, non-volatile channel conductance updates with high linearity and symmetry.

Second, EGTs integrated with PVDF-TrFE ferroelectric polymer as a channel/electrolyte interlayer are presented. The polarized domains of PVDF-TrFE enhance the transport of cations at the interface, allowing for effective penetration of cations into the channel. Additionally, the downward polarized domains suppress the self-diffusion of cations from the channel back into the electrolyte. As a result, these EGTs exhibit essential synaptic characteristics, including excitatory postsynaptic current, long-term synaptic plasticity, and a near-linear conductance update.

This study introduces novel methodological approaches to modulating ion dynamics at the interface, aimed at advancing practical applications for artificial synapses and neuromorphic computing systems. While prior researches have explored the application of EGTs as artificial synapses, these studies focused on understanding the fundamental ion dynamics have been limited. Hence, this work emphasizes the pivotal importance of modulating ion dynamics and highlights that a comprehensive understanding of ions and charge interactions is essential for providing key insights into the application of EGTs as artificial synapses.

Keyword: Neuromorphic computing, artificial synapse, electrolyte-gated transistors, ion-dipole interaction, ion dynamics

Student Number: 202023990

Table of Contents

Chapter 1. Introduction 1

1.1 Introduction of artificial synapse 1

1.2 Comparison of characteristics between candidates for artificial synapses 4

1.3 The potential and limitation of electrolyte-gated transistors 7

1.4 Dipole engineering in EGTs for modulating ion dynamics 8

Chapter 2. Ion-trapping fluorinated self-assembled monolayer in EGTs 11

2.1 Introduction 11

2.2 Investigating the ion-trapping effect by F-SAM 13

2.2.1 Device configuration 13

2.2.2 Synaptic characteristics of FAS-modified EGT 19

2.2.3 Effect of the magnitude of dipole moment 28

2.2.4 Elucidating working mechanism of FAS-modified EGT . 32

2.2.5 Conductance update in FAS-modified EGT 43

2.2.6 Inference tasks using artificial neural network 50

2.2.7 Experimental method 53

2.3 Verification of the ion-dipole force induced by F-SAM 57

2.3.1 Rationale for changing F-SAM 57

2.3.2 Device configuration 58

2.3.3 Analysis of electrical characteristics in FLEGT 63

2.3.4 Analysis of ion-dipole force 71

2.3.5 Inference tasks for device performance using CNN 85

2.3.6 Experimental method 88

2.4 Conclusion 91

Chapter 3. Ferroelectrically modulated ion dynamics for analog computing 92
3.1 Introduction 92
3.2 Device configuration 93
3.3 Analysis of the working mechanism of Li^+ FP-EGT 100
3.4 Synaptic characteristics in Li^+ FP-EGT 108
3.5 Identifying the origin of LTP characteristics 112
3.6 Conductance update in Li^+ FP-EGT 114
3.7 Mechanical and environmental stability test 117
3.8 Application for inference tasks using CNN 122
3.9 Experimental method 125
3.10 Conclusion 128

Chapter 4. Conclusion and outlook 129

Bibliography 132

List of publications 147

Abstract in Korean 149

List of table and figures

Figure 1.1. (a) Ranking of the qualitative device requirements for three prospective applications. A larger value on a given axis indicates a higher requirement in terms of the corresponding metric. (b–h) Schematic illustrations of device requirements for computing: (b) analog states, (c) on/off ratio, (d) linearity, (e) symmetry, (f) endurance, (g) retention and (h) yield. The dashed and solid curves in b–e indicate the conductance tuning of an analog non-volatile memory (NVM) device. The conductance updates of a NVM device in the training process are usually in the partial scope rather than in the full range of the conductance window, shown in (f). After NVM devices are tuned to different conductance levels, the conductance of the devices can fluctuate over time and two levels may overlap, shown in (g). The NVM devices that cannot be tuned to the target conductance level are considered failed devices, shown in (h). Figures reprinted with permission from Ref. [1]

Figure 1.2. (a–c) Two-terminal NVM devices for synaptic weights: (a) RRAM, (b) PCM and (c) MRAM. The two-terminal synaptic devices exhibit both of the weight tuning and synaptic inference operation in the top-bottom path. (d–f) Three-terminal NVM devices for synaptic weights: (d) flash memory, (e) FeFET and (f) ECRAM. Figures reprinted with permission from Ref. [1]

Figure 2.1. (a) Schematic images of the biological synapse and 1H,1H,2H,2H-Perfluorooctyltriethoxysilane (PFOTS$_5$)-treated ZnO (PFOTS$_5$/ZnO) EGT, respectively. The functional configurations of EGT corresponding to biological synapse are named in (a), respectively. (b) Schematic image of the channel region of PFOTS$_5$/ZnO EGT. (c) C 1s XPS spectrum of PFOTS$_5$/ZnO layer. (d) Optical image

of $PFOTS_5$/ZnO EGT. Scale bar = 500 μm.

Table 2.1. Chemical structures and nomenclatures of FAS used in this study. The subscript in nomenclatures is the number of fluoroalkyl chains.

Figure 2.2. AFM surface image of the (a) bare ZnO and (b) $PFOTS_5$/ZnO. The difference of root-mean-square roughness (R_{rms}) before and after $PFOTS_5$ deposition is 0.107 nm.

Figure 2.3. (a) Electrolyte components and (b) fabrication steps of UV cross-linked polymer electrolyte. The electrolyte solution was made by mixing the HMOPP-added PEGDMA solution with Li salts aqua solution. We applied the electrolyte solution on the device by drop-casting, and then cross-linked the electrolyte using UV irradiation to solidify the electrolyte. (c) Linear sweep voltammetry of water, water in PEGDMA, and Li^+ electrolyte in this work. thickness: 0.4 mm, the radius of contacted area: 4.7 mm. (d) Electrochemical Impedance Spectroscopy (EIS) data of Li^+ electrolyte at room temperature. The ionic conductivity of Li^+ is calculated by $\sigma_{ion} = \frac{d}{(R-R_0)\,A}$, where d is the thickness of the electrolyte, A is the contact area, R_0 is the interfacial resistance between electrode and electrolyte, and R is the internal resistance of the electrolyte.

Figure 2.4. EPSC responses and decay behaviors of (a,b) bare ZnO EGT and (c,d) $PFOTS_5$/ZnO EGT from peak value, respectively ($V_G = 3$ V, $V_{DS} = 0.1$ V, Pulse width (t_w) = 50 ms). In (b,d), decay behaviors associated with the different mechanisms are divided into two regions from the transient temporal length (Δτ, red dash line). The white region indicates diffusion of Li^+ ions from the channel-electrolyte interface to the bulk of the electrolyte after the formation of the EDL (relaxation of EDL) and

the yellow region indicates a steady-state with the constant of the channel current, which refers to none of the changes in concentration of Li^+ ions at the interface.

Figure 2.5. (a) EPSC responses by gate voltage pulse with amplitudes of 1 V to 4 V (t_w = 50 ms) at V_{DS} = 0.1 V. (b) Dependence of change ratio (Δw) of the channel current as a function of the amplitude of the gate voltage pulse. $\Delta w = ((I - I_0) / I_0) \times 100\%$, where I_0 and I are the channel current before a gate pulse (initial state) and after applying a gate pulse, respectively. The blue region and the brown region indicate the volatile channel current, and the non-volatile channel current, respectively. (c) Retention test as a function of the amplitude of the gate voltage pulse for 1800 s. (d) EPSC responses by gate voltage pulse with widths of 25 ms to 200 ms (V_G = 3V) at V_{DS} = 0.1 V. (e) Dependence of change ratio (Δw) of the channel current as a function of the width of the gate voltage pulse. (f) LTP characteristic as a function of the numbers of gate pulses (#) (T_{int} = 50 ms).

Figure 2.6. (a) EPSC responses by gate voltage pulse with widths of 1 ms to 10 ms (V_G = 3 V) at V_{DS} = 0.1 V. (b) Retention test as a function of the width of the gate voltage pulse for 1800 seconds. (c) Comparison of changes in transient temporal length and non-volatile weight ratio as a function of the pulse width at V_G = 3 V.

Figure 2.7. (a) Paired-pulse facilitation (PPF) by 2 consecutive gate pulses of 3 V amplitude and 50 ms pulse interval (T_{int}). (b) PPF dependence on T_{int}.

Figure 2.8. Transfer curves of (a) bare ZnO EGT, (b) Trimethoxy(3,3,3-trifluoropropyl)silane (TFP_0)-treated ZnO (TFP_0/ZnO) EGT, (c) 1H,1H,2H,2H-Perfluorooctyltriethoxysilane ($PFOTS_5$)-treated ZnO ($PFOTS_5$/ZnO) EGT, and (d) 1H,1H,2H,2H-Perfluorodecyltriethoxysilane ($PFDTS_7$)-treated ZnO ($PFDTS_7$/ZnO)

EGT at a 0.8 V s^{-1} fixed scan rate (V_{DS} = 0.1 V). The voltage range of the hysteresis window (ΔV) is the full width at half maximum (FWHM) of the transfer curve. (e) Surface zeta potential of different FAS-treated ZnOs under a pH 7 solution. (f) Areal capacitances of Li^+ electrolyte with different FASs.

Figure 2.9. EPSC responses (left) and decay behaviors (right) of (a,b) TFP_0/ZnO EGT and (c,d) $PFDTS_7$/ZnO EGT (V_{DS} = 0.1 V, V_G = 3 V, t_w = 50 ms). (e) Changes of transient response time and non-volatile weight ratio by different FAS.

Figure 2.10. O 1s XPS spectra evolution of $PFOTS_5$/ZnO layer by different etch times. Judging from the XPS data, Li_2O peak (528.8 eV) is not identified.

Figure 2.11. Li elemental depth profile of (a) bare ZnO layer and (b) $PFOTS_5$/ZnO layer under initial state and after applying positive gate bias of 4V amplitude for 10 s. (c) Li 3D mapping image of $PFOTS_5$/ZnO layer. Sputtering rate: 0.025 nm s^{-1}. d) F 1s XPS spectrum of $PFOTS_5$/ZnO layer. (e,f) C 1s XPS spectrum of $PFOTS_5$/ZnO layer. Each peak is deconvoluted as a Gaussian-Lorentzian function.

Figure 2.12. (a) Transfer curve of $PFOTS_5$/ZnO EGT with Cs^+ electrolyte at a 0.8 V s^{-1} fixed scan rate. and (b) EPSC responses by gate voltage pulse with amplitudes of 1 V to 4 V (t_w = 50 ms) at V_{DS} = 0.1 V. (c) EPSC responses by gate voltage pulse with widths of 50 ms to 500 ms (V_G = 3V) at V_{DS} = 0.1 V. (d) Retention test as a function of the width of the gate voltage pulse for 1800 seconds. Dash line: initial state.

Figure 2.13. (a) Chemical structure of Triethoxyoctylsilane (TEOOS). (b) Transfer curve of TEOOS-treated ZnO (TEOOS/ZnO) EGT at a fixed rate of 0.8 V s^{-1}. (c) EPSC response of TEOOS/ZnO EGT by a single gate pulse (V_G = 3 V, t_w = 50 ms)

at V_{DS} = 0.1 V. (d) EPSC response of TEOOS/ZnO EGT by 20 consecutive gate pulses (T_{int} = 50 ms).

Figure 2.14. The dynamics of Li^+ ion of (a) bare ZnO EGT and (b) $PFOTS_5$/ZnO EGT. After a positive gate pulse is applied to the electrolyte in bare ZnO EGT, Li^+ ions quickly return to the equilibrium state, but $PFOTS_5$/ZnO EGT exhibits a non-volatile channel current because some Li^+ ions cannot return to the equilibrium state due to ion-trapping sites at $PFOTS_5$. Moreover, when gate pulses are consecutively applied to the electrolyte, more amounts of Li^+ ions are sequentially trapped in $PFOTS_5$, resulting in a higher excited non-volatile current.

Figure 2.15. (a) Channel conductance update by consecutive gate pulses of 60 potentiation and 60 depression (V_G = 4 V for potentiation, V_G = -4 V for depression, t_w = 50 ms, T_{int} = 50 ms). (b) 100 cycles of conductance update measured under the same condition with (a). The dashed square indicates the 5th cycle of conductance update, shown in (a). (c) The cycle-to-cycle variation during 100 cycles. The calculated variation of conductance is based on (b). The 50 device-to-device distribution of (d) nonlinearity of potentiation (black) and depression (blue) and (e) maximum (red) and minimum (blue) conductance.

Figure 2.16. (a) Comparison of conductance update of FAS-treated EGTs by identical pulses. The parameters compared through the conductance data are (b) nonlinearity and (c) dynamic range.

Figure 2.17. (a) Channel conductance update by non-identical consecutive gate pulses of 60 potentiation and 60 depression (V_G from 1.64 V to 4 V with increment of 0.04 V for potentiation and from -1.64 V to -4 V with decrement of -0.04 V for

depression, $t_w = 50$ ms, $T_{int} = 50$ ms). (b) 100 cycles of conductance update measured under the same condition with (a).

Figure 2.18. (a) Schematic illustration of 3-layer artificial neural network (ANN) consisted of 400 input neurons, 125 hidden neurons, and 10 output neurons for image recognition simulation. A 20 × 20 pixel Modified National Institute of Standards and Technology (MNIST) data set of handwritten digits is used for simulation. (b) Circuit diagram showing a synapse layer composed of EGT arrays and the peripheral circuit. (c) The recognition accuracy of the ideal device (gray) and real device (red, blue) in simulations using ANN. The accuracy of the ideal device is a case where nonlinearity is 0, which indicates conductance update with ideal linearity and symmetry. (d) Visualization images of the accuracy of each epoch during the learning process in simulation. (e) 32 × 32 binarized image programming in arrays of $PFOTS_5$/ZnO EGTs and bare ZnO EGTs and their data retention test

Figure 2.19. Recognition accuracies of FAS-treated ZnO EGTs in simulations using ANN. bare ZnO EGT (black), TFP_0/ZnO EGT (red), $PFOTS_5$/ZnO EGT (blue), $PFDTS_7$/ZnO EGT (green).

Figure 2.20. (a) Schematic illustration of FLEGT and components of its device. (b) C 1s XPS spectrum of F_{21}-DDPA layer. (c) Measured surface zeta potential of each modified surface at pH = 7.

Figure 2.21. Measured surface morphology profile of (a) a-IGZO and (b) F_{21}-DDPA-modified a-IGZO by atomic force microscopy (AFM) measurement.

Figure 2.22. Optical image of FLEGT. Scale bar: 100 μm.

Figure 2.23. Transfer curves for EGTs with each modified surface at fixed gate bias (V_G) scan rate of a 0.8 V s^{-1} (V_{DS} = 0.1 V)

Figure 2.24. Transfer curves by applying 10 consecutive V_G biases. (a) positive bias. (b) negative bias. (V_{DS} = 0.1 V, scan rate: 0.8 V s^{-1})

Figure 2.25. Measured leakage current (I_{GS}) through the electrolyte. (V_{DS} = 0.1 V, scan rate: 0.8 V s^{-1}) The inset figure shows a leakage current in FLEGT.

Figure 2.26. (a,b) Current responses by a single V_G pulse with amplitudes varying from 1 V to 3 V (t_w= 10 ms, V_{DS} = 0.1 V) in (a) LEGT and (b) FLEGT. The figures located to the right of the current response depict the decay behavior following the application of a single pulse, revealing differences in the write-read delay. The purple dashed line indicates the write-read delay. (c) Energy consumption per spike in each EGT. The energy consumption is calculated by $V_{DS} \times I_{DS} \times t_w$. (d) Potentiation and depression process with 5 consecutive V_G pulses (t_w = 10 ms, T_{int} = 5 s). (e) Retention characteristics of the 10 states. Each state is switched by randomly applying consecutive V_G pulses with varying pulse numbers (#) of 10-200 and amplitudes of 1-3 V. Pulse width (t_w) and interval (T_{int}) are fixed at 10 ms.

Figure 2.27. (a-f) Conductance updates in FLEGT with varying (a) pulse number of 128 and 256, (b) V_G amplitudes from ±1 V to ±3 V, (c) pulse width and interval from 500 μs to 10 ms, and (d-f) their respective parameters including LTP/LTD nonlinearity and dynamic range. The gray dashed line indicates perfect linearity, corresponding to NL of 0. (g) Comparison conductance update between LEGT and FLEGT. (h) Cycle-to-cycle variation for 100 cycles. The input parameters are described in the figure. (i) Device-to-device variation across 20 devices. The data are

collected from the 10th cycle in each device.

Figure 2.28. (a) Schematic illustration of LEGT. (b) I_{DS} response by 30 consecutive V_G pulses in LEGT. (c) Conductance updates in LEGT with fixed input parameters (V_G = 3 V, # = 256, T_{int}, t_{w} = 10 ms).

Figure 2.29. (a, b) Schematic illustration of working mechanisms in (a) LEGT and (b) FLEGT. (c) Crystal structure of spinel-IGZO for DFT calculation. pink: indium (In), green: gallium (Ga), black: zinc (Zn), red: oxygen (O).[2]

Figure 2.30. (a) Schematic image of each lithium migration path for calculating binding energy (ΔE) derived from density functional theory (DFT) calculation. (b) Differential charge density (Δρ) associated with each migration path of lithium in F_{21}-DDPAs. purple: lithium (Li), black: carbon (C), orange: fluorine (F), brown: phosphorus (P), yellow: hydrogen (H), red: oxygen (O), green: zinc (Zn), pink: indium (In), gray: gallium (Ga), purple background: IGZO region. Yellow and blue graphics indicate charge accumulation and depletion, respectively. isosurface: 0.002 e $Å^{-3}$. The surface of crystalline spinel-IGZO is (111) for simplifying DFT calculation.[2] (c) Calculated ΔE according to lithium migration path. (d) Differential Δρ associated with the absorption of lithium on the surface of IGZO. isosurface: 0.001 e $Å^{-3}$. (e) XPS spectra of F 1s in the initial state and the state after applying positive bias for 30 s of F_{21}-DDPA.

Figure 2.31. (a) Areal capacitance and (b) impedance as a function of applied AC voltage frequency. (c) Nyquist plot of the MIM structures.

Figure 2.32. (a) Schematic illustration of the ionic liquid ($[EMIM]^+[TFSI]^-$)-gated a-IGZO transistor with F_{21}-DDPA interlayer. (b) Transfer curve for the ionic liquid-

gated a-IGZO transistor at a fixed scan rate of 0.8 V s^{-1} (V_{DS} = 0.1 V). (c) Current responses by a single gate pulse with amplitudes varying from 1 V to 3 V (t_w= 10 ms, V_{DS} = 0.1 V). (d) Conductance updates in LEGT with fixed input parameters (V_G = 3 V, # = 256, T_{int}, t_w = 10 ms).

Figure 2.33. (a) The configuration of each layer in CNN and process steps for training and testing tasks of input data. The input data is derived from the CIFAR-10 dataset, which consists of 10 classes of images, each sized 32 x 32 pixels and featuring 3 colors (red, green, blue). The gray dashed line indicates a schematic illustration of the artificial neural network composed of the EGT devices in a crossbar circuit, corresponding to the fully connected layer (7, 8). (b) Inference accuracy and (c) maximum accuracy during training and classification tasks for both an ideal device (gray) and an experimental device (red). An ideal device is defined by a nonlinearity of 0, and a deviation value of the device being 0 %.

Figure 3.1. (a) Schematic illustration of 3-terminal Li^+ FP-EGT. Al is used as the electrode for the source and drain, and the Au probe tip is used as an electrode for the gate. (b) XRD spectrum of PVDF-TrFE thin film annealed at 135 ℃. (c) Capacitance-electric field analysis of PVDF-TrFE capacitors with a structure of metal-ferroelectric-metal (MFM) at an AC voltage frequency of 1 kHz and a double sweep of an electric field from -1 MV cm^{-1} to 1 MV cm^{-1}. (d) Transfer curve for Li^+ FP-EGT at a 0.8 V s^{-1} fixed scan rate (V_{DS} = 0.1 V). (e) Changes in I_{DS} during 5 consecutive V_G double sweeps (0 V → 1 V → 0 V).

Figure 3.2. Surface morphology profiles of PVDF-TrFE annealed at (a) 60 ℃, (b) 100 ℃, (c) 135 ℃, and (d) 185 ℃ by AFM measurement.

Figure 3.3. Transfer curves of Li^+ FP-EGTs with varying annealing temperatures of (a) 60 °C, (b) 100 °C, (c) 135 °C, and (d) 185 °C of PVDF-TrFE at a scan rate of 0.8 V s^{-1} (V_{DS} = 0.1 V).

Figure 3.4. Elemental depth profile of Li FP-EGT (a) in an initial state and (b) after applying positive gate bias. To confirm the difference in Li intensity, a gate bias of 3 V amplitude is applied for 10 s. (c) XPS depth profile of F 1s region in PVDF-TrFE layer. (d) Working mechanisms of Li^+ FP-EGT. The partial polarization switching occurs sequentially in the ferroelectric domains of PVDF-TrFE by the applied gate pulses and Li^+ ions are also transported from the electrolyte to ZnO. Polarized domains also suppress the self-diffusion of Li^+ ions electrochemically doped in the ZnO layer.

Figure 3.5. (a) Areal capacitance and (b) impedance as a function of applied AC voltage frequency. The capacitance and impedance of electrolyte/PVDF-TrFE/ZnO are measured with a 2-terminal structure, ITO/insulator/ITO. Inset values indicate the value of $\frac{d\log|Z|}{d\log f}$ in each process. In electrolyte/PVDF-TrFE/ZnO (blue points), When the changes in capacitance are almost constant, $\frac{d\log|Z|}{d\log f}$ shows a value of about -0.60 (fully charged EDL shows a value of -0.58). Reduced $\frac{d\log|Z|}{d\log f}$ indicates the capacitance is affected by a specific process by Li^+ ions.

Figure 3.6. (a) Equivalent circuit for analysis of the difference in charge transfer resistance (R_{ct}). (b) Nyquist plot of the electrolyte/PVDF-TrFE/ZnO with 2-terminal structure, ITO/insulator/ITO.

Figure 3.7. (a) EPSC responses by a single gate voltage pulse with amplitudes of 0.5 to 2 V (t_w = 10 ms) at channel voltage (V_{DS}) = 0.1 V. Dependence of ratio of channel current as a function of (b) the amplitude of the gate voltage pulse and (c) the width (t_w) of the gate voltage pulse. (d) Dependence of paired-pulse facilitation (PPF) on pulse interval (T_{int}) by 2 consecutive gate pulses. (e) LTP characteristics as a function of the amplitudes of gate voltage pulses and (f) its retention tests for 500 s.

Figure 3.8. Electrical characteristics of Li^+ EGT without PVDF-TrFE. (a) Transfer curve of Li^+ EGT at 0.8 V s^{-1} fixed scan rate (V_{DS} = 0.1 V). (b) STP characteristics by a single gate voltage pulse with amplitudes of 0.5 to 3 V (t_w = 10 ms) at channel voltage (V_{DS}) = 0.1 V. (c) LTP characteristic by 30 consecutive gate pulses.

Figure 3.9. Electrical characteristics of IL FP-EGT. (a) Schematic illustration of IL FP-EGT. (b) Transfer curve of IL FP-EGT at a 0.8 V s^{-1} fixed scan rate (V_{DS} = 0.1 V). (c) STP characteristics by a single gate voltage pulse with amplitudes of 1 to 3 V (t_w = 10 ms) at channel voltage (V_{DS}) = 0.1 V. (d) LTP characteristic by 50 consecutive gate pulses.

Figure 3.10. (a) LTP/LTD characteristics with varying amplitudes and numbers (#) of gate voltage pulses. (b) Cycle-to-cycle distribution test over 100 cycles. Extracted parameter values from Fig. 4(a), including (c,d) nonlinearity on the LTP/LTD side (NL_P/NL_D), (e,f) asymmetry (AS), and (g,h) dynamic range (G_{max}/G_{min}) in each measurement condition of conductance update. (i) The 20 device-to-device distributions of conductance update at the 100th cycle.

Figure 3.11. (a) Actual image of Li^+ FP-EGT on the polyimide (PI) substrate. (b) LTP/LTD characteristics in each bent condition at bending radii 1.0 cm, 0.8 cm, and

0.6 cm. Extracted parameter values from Figure 3.11b, including (c) dynamic range and (d,e) nonlinearity on the LTP/LTD side. (f) Comparison of the difference in conductance update between the initial state and the state after bending 1000 cycles. (g) Relative comparison of each parameter value from Figure 3.11f, where relative parameter values in the initial state are 100%.

Figure 3.12. Thermal stability test for Li^+ FP-EGT at a temperature of (a) 40 °C, (b) 60 °C, (c) 80 °C, and (d) 100 °C. The measured electrical condition is the same as Figure 3.10b.

Figure 3.13. Humidity stability test for Li^+ FP-EGT at a relative humidity (RH) of (a) 30%, (b) 50%, (c) 80%, and (d) 80% with device encapsulation. The measured electrical condition is the same as Figure 3.10b. Here, for encapsulation, we use epoxy to cover the entire device and Au wire is used as a gate electrode.

Figure 3.14. (a) Convolution neural networks consisted of convolution layers, pooling layers, and fully connected layers. (b) Circuit diagram showing fully connected layers composed of Li^+ FP-EGT arrays and the peripheral circuit. (c) Inference accuracies in the ideal case of the device (gray) and the experimental case of the device (red). An ideal device indicates a case where nonlinearity is 0 and cycle-to-cycle distribution and device-to-device distribution are 0%. (d) Inference accuracies in the bent case of the device (blue) and bent case after bending 1000 cycles of the device (green).

Chapter 1. Introduction

1.1. Introduction of artificial synapse

With increasing demands of artificial intelligence (AI) and processing of big data, neuromorphic computing which leverages the biological synaptic functions between adjacent neurons at a synapse has been proposed to handle large amounts of data at low energy consumption, where conventional computing with von-Neumann architecture may face a significant bottleneck at low energy efficiency.[3], [4] Specifically, conventional computing hardware relies on the von Neumann architecture, where processing and memory units are physically distinct. While this design is effective for tasks like complicated computing, which require high-precision data representation and accurate Boolean operations, it proves inefficient for large amount tasks and AI-related tasks.[1]

Neuromorphic computing system mimic the structure and functional principles of the human brain, presenting a promising pathway for advancing intelligent computing. Compared to conventional computing systems, these systems are anticipated to provide significant benefits in terms of energy efficiency and computational power, particularly when handling AI tasks.[1], [5] At the biological synapses, the synaptic functions are based on the variation of membrane potential across the two neurons, where the finite potential difference depends on the spatiotemporal change of spikes of input potential (i.e., action potential). In the synaptic functions, the long-term change of membrane potential (i.e., long-term synaptic plasticity) by triggering the series of spikes of the action potential.[6] The number of released neurotransmitters associated with the number of spikes is related to the origin of learning and remembrance in the biological system.

Similar to biological synapses, in neuromorphic system, this innovative architecture performs computation and memory operations simultaneously within a specific resistor, termed an 'artificial synapse', which is different from the von Neumann architecture. These artificial synapses, structured in parallel circuits, are distinguished by their tunable analog electrical conductance. Artificial synapses function in the behavior of biological synapses, such as short/long-term synaptic plasticity (STP/LTP), through the variation of electrical conductance in response to external stimuli.[4] For application in neuromorphic accelerators, artificial synapses must possess the capability to variably tune synaptic weights linearly and symmetrically with high dynamic range, and they should be capable of maintaining updated synaptic weights for inference and learning process (Figure 1.1).

Neuromorphic devices are not intended to replace traditional CPUs or GPUs but are more suitable for handling large volumes of data associated with artificial intelligence (AI) tasks. While CPUs and GPUs are designed for general-purpose computing with high processing speeds and versatility, neuromorphic systems are inspired by the structure of biological neural networks and excel in tasks involving pattern recognition, deep learning, and non-linear data processing. Neuromorphic devices offer advantages in energy efficiency, adaptability, and parallel processing, making them ideal for specific AI applications. However, they do not possess the same broad computational capabilities as traditional systems. Instead, neuromorphic and conventional computing technologies are expected to complement each other, with neuromorphic systems playing a key role in processing large-scale data for AI tasks, while CPUs and GPUs handle more general computational needs.

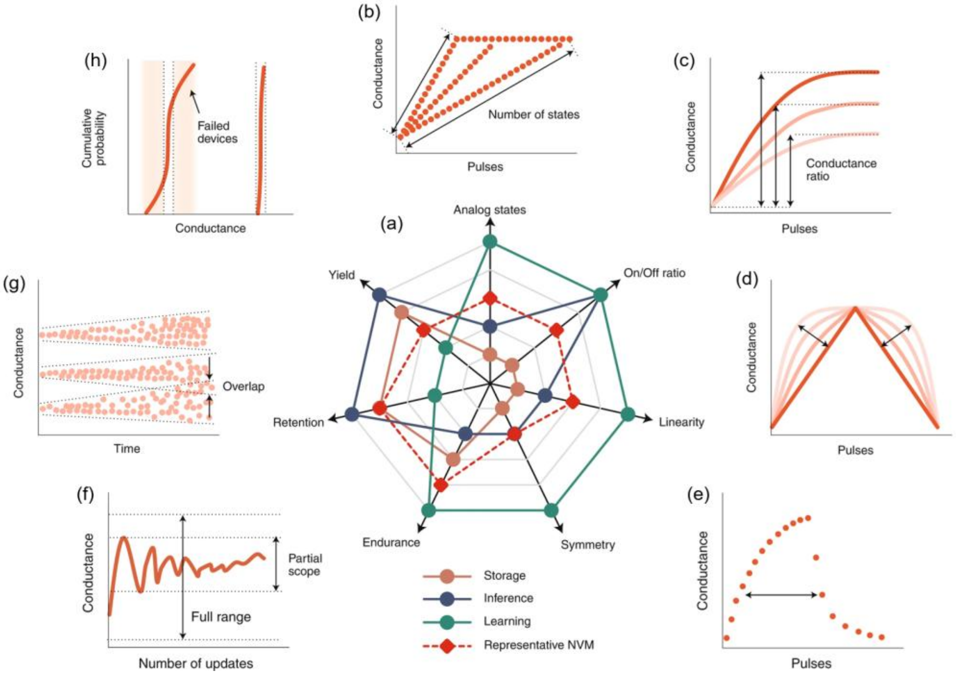

Figure 1.1. (a) Ranking of the qualitative device requirements for three prospective applications. A larger value on a given axis indicates a higher requirement in terms of the corresponding metric. (b–h) Schematic illustrations of device requirements for computing: (b) analog states, (c) on/off ratio, (d) linearity, (e) symmetry, (f) endurance, (g) retention and (h) yield. The dashed and solid curves in b–e indicate the conductance tuning of an analog non-volatile memory (NVM) device. The conductance updates of a NVM device in the training process are usually in the partial scope rather than in the full range of the conductance window, shown in (f). After NVM devices are tuned to different conductance levels, the conductance of the devices can fluctuate over time and two levels may overlap, shown in (g). The NVM devices that cannot be tuned to the target conductance level are considered failed devices, shown in (h). Figures reprinted with permission from Ref. [1]

1.2. Comparison of characteristics between candidates for artificial synapses

Developing artificial synapse with suitable electrical characteristics is a key factor in constructing brain-inspired architecture. As shown in Figure 1.2, several candidates based on two-terminal memory devices with various operating mechanisms, such as resistive switching random access memory (RRAM)[7]–[9], phase-change random access memory (PCRAM)[10], magnetic random access memory (MRAM)[11] have been reported. One of the primary benefits is that two-terminal devices typically have fewer components compared to more complex multi-terminal devices, making them easier to integrate into large-scale neuromorphic systems. Additionally, two-terminal devices can provide non-volatile storage, meaning they retain information even when power is removed, which is crucial for long-term memory retention in artificial neural networks. The two-terminal devices have, however, fundamental problems in the application of artificial synapses due to structural and mechanistic limitations such as interference of written conductance, sneak currents, and conductance updates with low linearity and poor cycle-to-cycle variations.[12], [13] Also, linearly and symmetrically updating the electrical conductance across the two terminals is very challenging as the two-terminal devices have to write and read memory via the same terminals. The reading process in two-terminal devices can change the written electrical conductance, which is supposed to be kept in a long-term period.[14],[15]

To overcome the limitations in two-terminal devices, synaptic devices based on field-effect transistors (FETs) have been proposed with the advantages of separated terminals for writing and reading.[12], [16], [17] Various types of FETs have been proposed as candidates for artificial synapses, among which devices with memory characteristics, such as floating-gate[18]–[20], ferroelectric transistors[21], [22], and electrolyte-gated transistors, have gained significant attention as potential candidates. Among these, the floating-gate transistor exhibits excellent memory characteristics; however, it has the disadvantage of requiring a high writing voltage to trap charges in the floating gate, which leads to poor energy efficiency. Also, the ferroelectric transistor suffers from the limitation that due to the physical constraints of the ferroelectric domain, it cannot switch in a stepwise manner, hindering the linear tuning of electrical conductance.

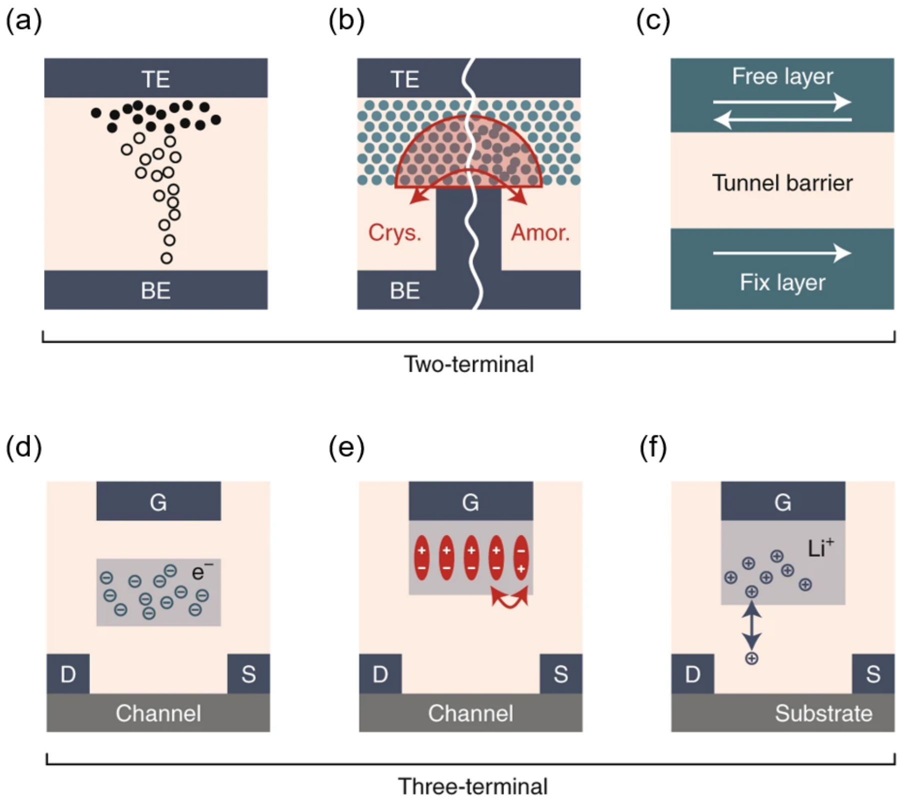

Figure 1.2. (a–c) Two-terminal NVM devices for synaptic weights: (a) RRAM, (b) PCM and (c) MRAM. The two-terminal synaptic devices exhibit both of the weight tuning and synaptic inference operation in the top-bottom path. (d–f) Three-terminal NVM devices for synaptic weights: (d) flash memory, (e) FeFET and (f) ECRAM. Figures reprinted with permission from Ref. [1]

1.3. The potential and limitation of electrolyte-gated transistors

Electrolyte-gated transistors (EGTs) are considered as a potential candidate due to their low switching voltage attributed to the high capacitance of the electrolyte, fast response, and the high flexibility in device configuration.[23]–[25] The working mechanism of EGT involves changing the channel conductance through physical or chemical interactions of cations (e.g., H^+, Li^+, or $EMIM^+$) or anions (e.g., OH^-, O_2^-, or $TFSI^-$) in the electrolyte with the channel, thereby representing changes in synaptic weight. Fundamentally, as the electrical potential is applied to the electrolyte, ions move to the channel-electrolyte interface, forming an electric double layer (EDL). When a high potential or sufficient longer potential is applied, ions positioned at the interface are electrochemically doped into the semiconductor channel. Such formation of EDL and electrochemical reaction occur changes in channel conductance indicating STP and LTP, respectively.[26], [27]

EGTs can be classified as follows based on their working mechanisms, which rely on physical or chemical interactions between ions and semiconductor channel: intercalation, alloying reaction by electrochemical reaction, and the formation of EDL. For EGT with intercalation channels, such as WO_3,[28], [29] LiPON,[30] and $LiCoO_2$,[31], [32] a notable advantage is the outstanding retention of switchable conductance states, attributed to the phase changes occurring within intercalation channels. However, these devices face difficulties in exhibiting low dynamic range and relatively high energy consumption. Additionally, EGTs operated by electrochemical doping present critical limitations, including their low linearity and poor reliability due to repetitive chemical reactions.[33]–[35] Consequently, approaches to mitigating these limitations have to consider manipulating the reversibility of changes in channel conductance by forming an EDL as physisorption at the channel/electrolyte interface.

However, given the inherent characteristic of electrolytes to equilibrate charges, an EDL formed at the interface by an instantaneously applied electric field is likely to be abrupt and transient.[36], [37] Therefore, considering charge interactions with ions at the interface becomes crucial for achieving tunable conductance with high linearity and long-term retention.

1.4. Dipole engineering in EGTs for modulating ion dynamics

As discussed in 1.3, the ions at the interface can be abruptly dissipated into the bulk of electrolyte when the electric field from the gate is removed, which is the fundamental shortcoming to ensure long-term synaptic plasticity and conductance update with linearity and symmetry. To overcome this problem, considering charge interactions with ions is essential to hold ions near the surface of the channel or to precisely penetrate ions to the channel, resulting in potentially controlling electrical conductance with long-term retention in EGTs.

One approach to enhancing the performance of EGTs is the introduction of an interlayer with a dipole moment at the channel/electrolyte interface. This modification can change ion movement, providing a solution to the presented issues. The coulomb force F, also called the electrostatic force, is the amount of force between two electrically charged particles or points, which is followed by

$$F = k_e \frac{q_1 q_2}{r^2} \qquad (1.1)$$

where k_e is a constant, q_1 and q_2 are the quantities of each charge, and the scalar

r is the distance between the charges. Therefore, if the two charged points have charges of opposite signs, the force makes them attract. In the current system, when multiple discrete charges exist on a macroscopic scale, the total coulomb force $\mathbf{F(r)}$ can be expressed as follows,

$$\mathbf{F(r)} = \frac{q}{4\pi\varepsilon_0}\sum_{i=1}^{n} q_i \frac{r_i}{|r_i|^3} \tag{1.2}$$

where q_i is the magnitude of the ith charge, r_i is the vector from its position to r, and constant ε_0 is the vacuum electric permittivity. By artificially creating sites at the interface where localized coulombic interactions between ions and dipoles can act, it becomes possible to trap ions at the interface or allow for gradual penetration to the channel, thereby controlling the ion dynamics.

From this perspective, this dissertation aims to propose the potential use of EGTs as artificial synapses by introducing an interlayer with a dipole moment and to highlight the effectiveness of utilizing ion-dipole interactions. In this dissertation, cations are the primary focus, with lithium ions being selected. The reason for this is that among alkali ions, lithium ions have the highest charge density, the lowest ionic mass among alkali ions, and the highest ion conductivity. Also, although various materials could be selected as candidates for the interlayer, the following reasons led to the selection presented in this dissertation: (i) it is electrically insulating, (ii) it has a thickness on the nm-scale, and (iii) it possesses a strong dipole moment capable of interacting with cations. The composition of this dissertation is described as follows. In Chapter 2, a fluorinated self-assembled monolayer (F-SAM), which induces negative charges and has a sub-10nm thickness, is introduced that induces ion trapping by leveraging coulombic attraction between lithium ions and F-SAMs. To demonstrate the effect of ion trapping, the trapping mechanism is analyzed through both electrical and chemical characterization, and the attraction force was calculated using ab initio calculations. Additionally, inference tasks are conducted using a convolutional neural network (CNN) to highlight the potential application of the EGT device. In Chapter 3, the interaction between ions and ferroelectric domains is investigated by introducing a ferroelectric polymer in the EGT device. In this ferroelectric structure, changes in ion movement by domain switching under an electric field are observed, and improvements in synaptic characteristics for analog computing are also analyzed. In the final Chapter 4, overall summary and conclusion of this dissertation are discussed, with an emphasis on the research significance of these works.

Chapter 2. Ion-trapping fluorinated self-assembled monolayer in EGTs

2.1. Introduction

As discussed in Chapter 1.3, approaches to mitigating limitations in EGT have to consider manipulating the reversibility of changes in channel conductance by forming an EDL as physisorption at the channel/electrolyte interface. Nevertheless, given the inherent characteristic of electrolytes to equilibrate charges, an EDL formed at the interface by an instantaneously applied electric field is likely to be abrupt and transient.[36], [37] Therefore, considering charge interactions with ions at the interface becomes crucial for achieving tunable conductance with high linearity and long-term retention.

In this chapter, fluorinated self-assembled monolayer (F-SAM) as an interfacial ion receptor is introduced in EGT, specifically emphasizing its role in the physisorption of ions induced by large dipole moment at the channel/electrolyte interface.[38], [39] The advantage for using F-SAM is that it consists of fluoroalkyl chains and a trifluoromethyl group, which result in a large dipole moment, thereby enabling strong coulombic interactions with lithium ions, despite a molecular length of sub-2 nm. The device incorporates zinc oxide (ZnO) and amorphous indium gallium zinc oxide (a-IGZO) as the channel material, noteworthy for its low off-current and high field-effect mobility in n-type thin-film transistors.[40]–[42] Also, water-in-bisalt lithium electrolyte is used as the polymer dielectric, which is remarkable for its high areal capacitance and large electrochemical window.[43], [44] With the introduction of F-SAM in EGT, robust ion-dipole force is observed between the lithium ions and F-SAM, resulting in the immobilization of lithium ions at the channel/electrolyte interface. The lithium EGT with F-SAM shows, therefore, exceptional synaptic characteristics, such as switching conductance with near-linearity and long-term retention (>30 min), even at a switching voltage below 4 V. Specifically, through chemical analysis and density functional theory (DFT) calculations, lithium ions become strongly trapped within the van der Waals gap of F-SAM. This chapter propose an EGT-based artificial synapse with multimodal behavior by suggesting a method of integration for F_{21}-DDPA, indicating its considerable applicability in neuromorphic accelerators performing both training and inference tasks.

In Section 2.2, by incorporating silane-based F-SAM into EGT, this section aims to investigate the interactions between lithium ions and investigate the electrical characteristics of artificial synapses. Here, to further examine the effect of coulombic interactions based on the magnitude of the dipole moment, the length of the fluoroalkyl chains in the F-SAM is varied to observe the resulting changes in characteristics. In Section 2.3, phosphonic acid-based F-SAM is introduced into the EGT to enhance the performance of artificial synapses and optimize the fabrication process. Additionally, the binding energy between ions and F-SAM was analyzed using DFT calculations with projector augmented wave (PAW) method to elucidate the working mechanism.

2.2. Investigating the ion-trapping effect by F-SAM

2.2.1. Device configuration

Figure 2.1a shows a biological synapse and fluoroalkylsilane (FAS)-treated ZnO EGT, where the insets indicate the similarity in terms of each functional configuration. To make sure of the long-term synaptic plasticity with linearly updating the channel conductance in EGTs, FAS is introduced, as it can potentially capture the Li^+ ions and then is likely to maintain the EDL at the channel-electrolyte interface without the electric field by the gate electrode. For FAS, This device includes 1H,1H,2H,2H-Perfluorooctyltriethoxysilane (referred to as $PFOTS_5$, see Table 2.1 for the molecular structure), which can be deposited on the surface of ZnO via the chemical vapor deposition method (Figure 2.1b). In the X-ray photoelectron spectroscopy (XPS) spectrum of the $PFOTS_5$-treated ZnO surface (referred to as $PFOTS_5$/ZnO), the peaks of fluoroalkyl chains ($C-F_2$, 290.81 eV), trifluoromethyl group ($C-F_3$, 293.50 eV), and silane (C–Si, 283.8 eV) of $PFOTS_5$ are observed in C 1s region (Figure 2.1a). To confirm whether FAS is uniformly deposited on the surface of ZnO, atomic force microscopy (AFM) is introduced to investigate the roughness of the surface of $PFOTS_5$-treated ZnO (Figure 2.2). The measured root-mean-squared roughness of the surface of $PFOTS_5$/ZnO is about 1.2 nm, which is comparable to that of the surface of bare ZnO of about 1.1 nm, indicating FAS is uniformly coated on the surface of ZnO. $PFOTS_5$/ZnO EGT has a structure of conventional thin-film transistor (TFT) with the side-gate electrode, where a solution-processed ZnO is used as the channel layer and a top-contacted aluminum (Al) is used as electrodes of source, drain, and gate. For the gate insulator, a water-in-bisalt/polymer Li^+ electrolyte is used to mimic the synaptic functions as well as take advantage of high ionic conductivity and a wide electrochemical stability window (Figure 2.1d, see Figure 2.3 for preparation details).[45], [46] LiTFSi and LiOTf exhibit very high solubility in water, which provides the advantage of fabricating solid electrolytes with a high Li^+ concentration. This, in turn, implies a high gate capacitance. Due to the hydrophobic nature of $PFOTS_5$, water in the Li^+ electrolyte is less likely to be absorbed into $PFOTS_5$.[47] Water has low electrochemical stability (its electrochemical window is theoretically about 1.23V), so water can be split into oxygen and hydrogen on the electrode surface.[48] In the water-in-bisalt/polymer Li^+ electrolyte, however, because the number of water molecules is about twice the number of salt ions, water molecules are neither oxidized nor reduced on the electrode surface but instead react with Li^+ ions and form a solvation shell of Li^+ ions.[45], [46] Therefore, the electrochemical activity of water is greatly suppressed and the electrolyte has a strongly enhanced electrochemical stability. Also, the UV curing process solidifies PEGDMA with 2-hydroxy-2-methylpropiophenone (HMOPP). PEGDMA has a methacrylate group at the end, and after UV is applied, radical polymerization occurs by HMOPP which reacts with 4 other methacrylate groups to form a cross-linked network.[49], [50] As shown in Figure 2.3c, when the voltage is swept from 0V to 10V, the redox reaction of water (split to H^+ and OH^-) occurs at the electrodes, and the current dramatically increases. However, in the case of the water-in-bisalt/polymer Li^+ electrolyte, the redox reaction is inhibited and the electrolyte is stable even when the voltage from 0V to 10V is applied.

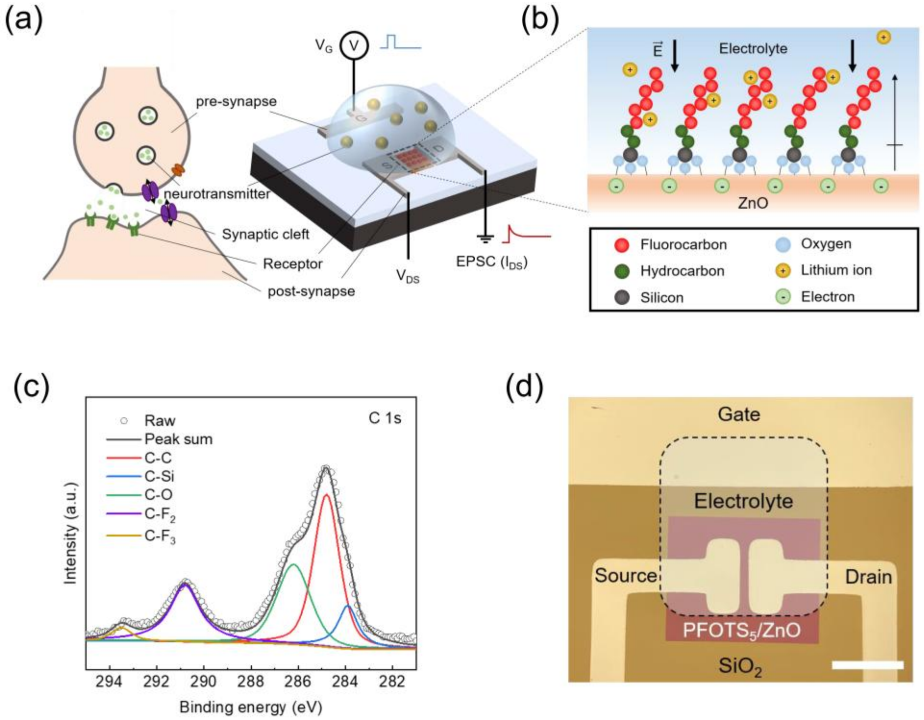

Figure 2.1. (a) Schematic images of the biological synapse and 1H,1H,2H,2H-Perfluorooctyltriethoxysilane ($PFOTS_5$)-treated ZnO ($PFOTS_5$/ZnO) EGT, respectively. The functional configurations of EGT corresponding to biological synapse are named in (a), respectively. (b) Schematic image of the channel region of $PFOTS_5$/ZnO EGT. (c) C 1s XPS spectrum of $PFOTS_5$/ZnO layer. (d) Optical image of $PFOTS_5$/ZnO EGT. Scale bar = 500 μm.

Fluoroalkylsilane	IUPAC Name	Chemical Structure
TFP_0	Trimethoxy (3,3,3-trifluoropropyl) silane	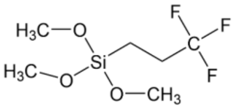 $CF_3(CH_2)_2Si(OCH_3)_3$
$PFOTS_5$	1H,1H,2H,2H-Perfluorooctyl triethoxy silane	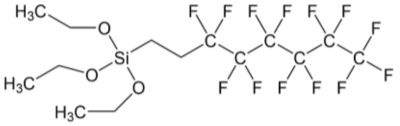 $CF_3(CF_2)_5(CH_2)_2Si(OCH_2CH_3)_3$
$PFDTS_7$	1H,1H,2H,2H-Perfluorodecyl triethoxy silane	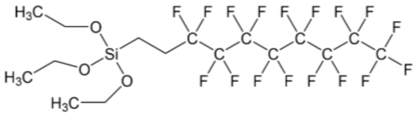 $CF_3(CF_2)_7(CH_2)_2Si(OCH_2CH_3)_3$

Table 2.1. Chemical structures and nomenclatures of FAS used in this study. The subscript in nomenclatures is the number of fluoroalkyl chains.

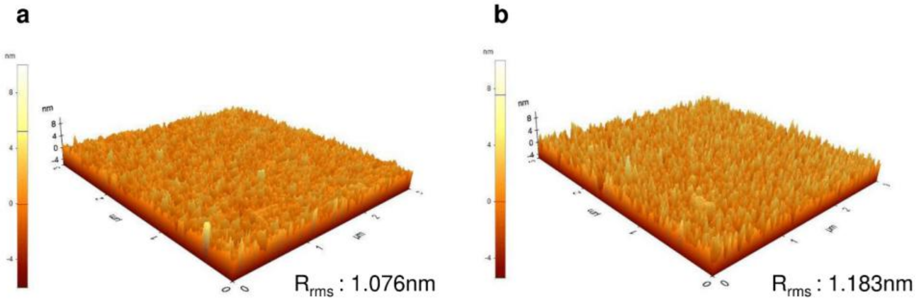

bare ZnO

PFOTS$_5$/ZnO

Figure 2.2. AFM surface image of the (a) bare ZnO and (b) PFOTS$_5$/ZnO. The difference of root-mean-square roughness (R_{rms}) before and after PFOTS$_5$ deposition is 0.107 nm.

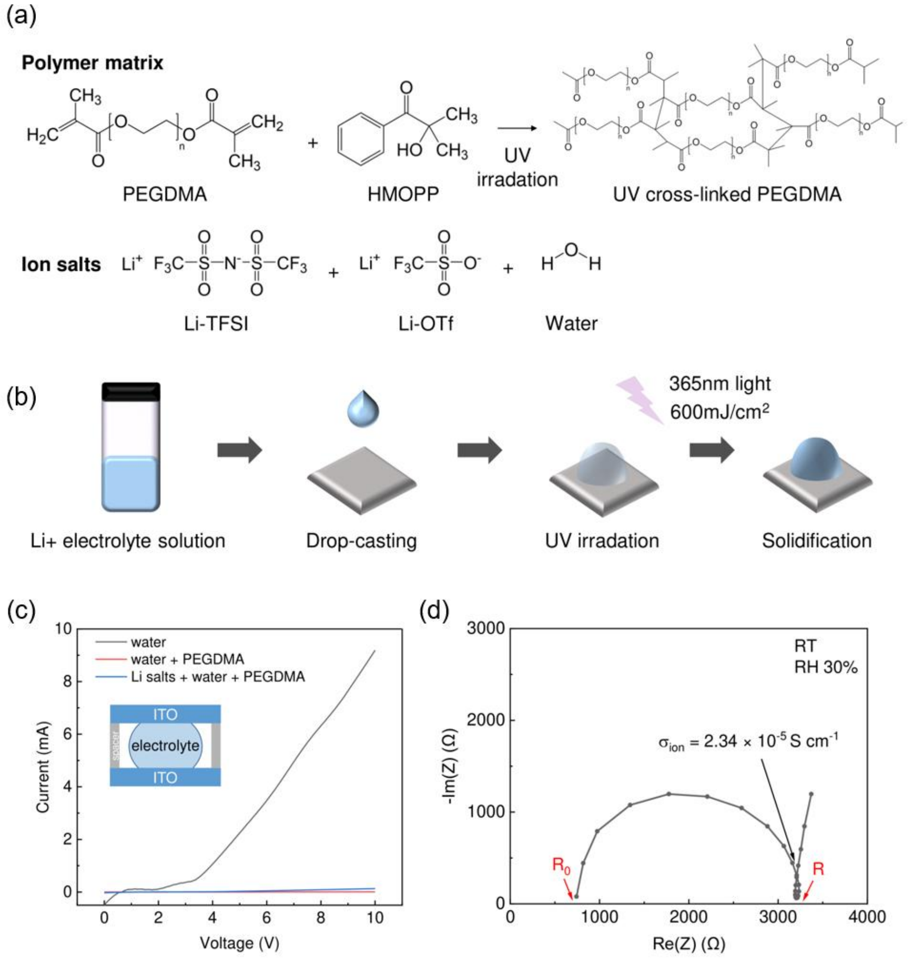

Figure 2.3. (a) Electrolyte components and (b) fabrication steps of UV cross-linked polymer electrolyte. The electrolyte solution was made by mixing the HMOPP-added PEGDMA solution with Li salts aqua solution. (c) Linear sweep voltammetry of water, water in PEGDMA, and Li^+ electrolyte in this work. thickness: 0.4 mm, the radius of contacted area: 4.7 mm. (d) Electrochemical Impedance Spectroscopy (EIS) data of Li^+ electrolyte at room temperature. The ionic conductivity of Li^+ is calculated by $\sigma_{ion} = \frac{d}{(R-R_0)\,A}$, where d is the thickness of the electrolyte, A is the contact area, R_0 is the interfacial resistance between electrode and electrolyte, and R is the internal resistance of the electrolyte.

2.2.2. Synaptic characteristics of FAS-modified EGT

The movement of Li^+ ions inside the electrolyte in an electric field can correspond to neurotransmitters in the synaptic cleft that triggers EPSC through the contact of post-synapse. In the biological synapse, short-term and long-term plasticity can be expressed associated with the intensity of EPSC.[27] In particular, emulating long-term plasticity is crucial to synaptic devices for neuromorphic computing.[5] Figure 2.4 shows EPSC responses of bare ZnO EGT and $PFOTS_5$/ZnO EGT by a single square gate pulse (V_G = 3 V, Pulse width (t_w) = 50 ms). In bare ZnO EGT with V_{DS} = 0.1 V, introducing a gate pulse yields the source-drain current (i.e., the channel current (I_{DS})) pulse, where the current rapidly increases to the peak value (~ 160 μA) and then returns to the value of the initial state (~ 46 μA) (Figure 2.4a). In contrast to the bare ZnO EGT, in $PFOTS_5$/ZnO EGT, the channel current after the peak looks like to approach a value of 2.4 μA, which is certainly higher than the value of the initial state of 1.2 μA, indicating the possibility to enable the long-term synaptic plasticity (Figure 2.4c).[51] It is noted that the overall exhibited value of the channel current of $PFOTS_5$/ZnO EGT is smaller than that of bare ZnO EGT, which may be beneficial to enable an energy-efficient synaptic device. These results of EPSC show that the $PFOTS_5$ on the surface of ZnO can be strongly effective to enable long-term synaptic plasticity.

After the gate pulse, the accumulated Li^+ ions at the channel-electrolyte interface should be diffused into the bulk of the electrolyte. Such diffusion process can influence the transient characteristic of dissipating the channel current; the change of the channel current is related to the concentration of Li^+ ions which form EDL with electrons of the channel at the interface.[52] Such transient characteristic is indicative of the second-level write-read delay in the device, reducing the write-read delay can greatly improve the operation speed of the device. Ion-induced EPSC response can be explained with the stretched exponential function and the decaying behavior can be fitted by the following equation[53]

$$I_{DS} = (I_0 - I_\infty)\exp\left[-\left(\frac{t-I_{DS}}{\tau_r}\right)^{\beta}\right] + I_\infty, \qquad (2.1)$$

where I_0 is the triggered channel current at the end of the gate pulse, I_∞ is the final value of the channel current, β is the stretch index ranging between 0 and 1, and τ_r is the length of the retention time. Accordingly, to indirectly investigate the diffusion process of Li^+ ions, I estimate the transient temporal length ($\Delta\tau$) of the channel current after the peak by taking the derivative of I_{DS} in terms of time ($\frac{\partial I_{DS}}{\partial t}$ and $\frac{\partial^2 I_{DS}}{\partial t^2}$),[26] and $\Delta\tau$ is defined when each differential value is 1 % from the peak value (Figure 2.4b,d). The $\Delta\tau$ for the $PFOTS_5$/ZnO EGT is ~ 0.23 s (indicated by the red dash lines in Figure 2.4d), which is nearly three times shorter than that of the bare ZnO EGT (~ 0.69 s). These results indicate that the $PFOTS_5$/ZnO EGT can finish the transient process faster than that of the bare EGT, implying the amounts of Li^+ ions diffused back into the electrolyte from the $PFOTS_5$/ZnO surface may be smaller than that of the bare EGT. Accordingly, it is also possible to reasonably assume that the left amount of Li^+ ions are likely to be held in $PFOTS_5$/ZnO surface, which can lead to the channel current being kept a higher value than the initial state.

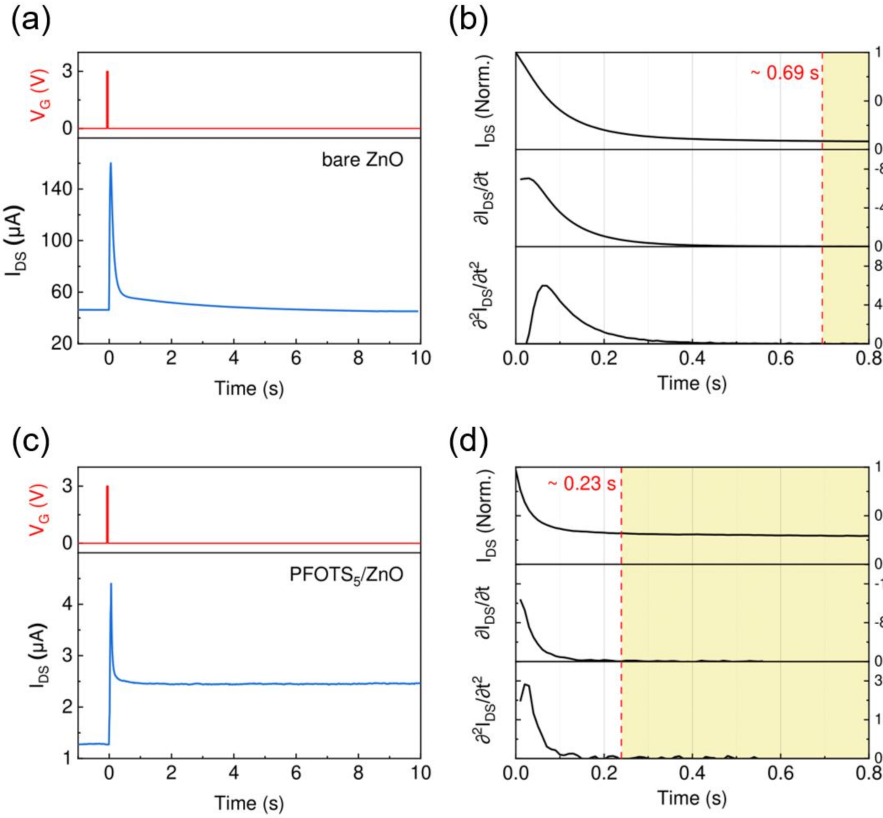

Figure 2.4. EPSC responses and decay behaviors of (a,b) bare ZnO EGT and (c,d) PFOTS$_5$/ZnO EGT from peak value, respectively (V_G = 3 V, V_{DS} = 0.1 V, Pulse width (t_w) = 50 ms). In (b,d), decay behaviors associated with the different mechanisms are divided into two regions from the transient temporal length (Δτ, red dash line). The white region indicates diffusion of Li^+ ions from the channel-electrolyte interface to the bulk of the electrolyte after the formation of the EDL (relaxation of EDL) and the yellow region indicates a steady-state with the constant of the channel current, which refers to none of the changes in concentration of Li^+ ions at the interface.

To investigate the robustness of $PFOTS_5$/ZnO EGT in the performance of synaptic plasticity, responses of the channel current is analyzed by varying input signal of EPSC in terms of amplitude, width, and the number of gate pulses. Figure 2.5a-c shows the responses of $PFOTS_5$/ZnO EGT by a single gate pulse with various amplitudes (V_G = 1, 2, 3, and 4 V) for the fixed width (t_w) = 50 ms of the gate pulse at V_{DS} = 0.1 V. For the cases with V_G = 4 V, $PFOTS_5$/ZnO EGT exhibits an obvious non-volatile characteristic of the channel current, where the channel current after the transient period can keep the value of nearly 60 % of the peak value (Figure 2.5a), showing the capability of long-term potentiation (LTP). Such effect can be also observed for the case with V_G = 3 V, but the value of non-volatile current is about 40 % of the peak value. In contrast, when the amplitude of gate pulse is reduced to 1 V or 2 V, the channel current after the peak continuously decreases and is close to the initial value, indicating short-term potentiation (STP).[54], [55] Furthermore, the peak values of the channel current increases exponentially as the amplitude of the gate pulse increases (Figure 2.5b). That is, the majority of the EDL is formed by Li^+ ions rather than atomic polarization.[56] The channel current after 5 s from the peak also shows a similar trend observed in the peak values. Interestingly, for the cases with V_G = 3 V and 4 V, the non-volatile channel current can be kept over 1800 s (Figure 2.5c). Meanwhile, for a gate pulse of 1V amplitude, the channel current returns to the value of the initial state within 300 s. I check whether the variation in the amplitude of the gate pulse affects the transient process, but the variations in the amplitude do not affect the transient temporal length (Figure S4). In addition, the value of the non-volatile channel current can be tuned with the pulse width of the gate pulse in EPSC. As shown in Figure 2.5d, $PFOTS_5$/ZnO EGT can have increased values of the non-volatile current as the pulse width is increased from 25 ms to 200 ms, and the increased values of the non-volatile current have a linear relationship with the pulse width (Figure 2.5e). Moreover, reducing the pulse width is of importance because it can improve the operation speed of the device and greatly reduce the write-read delay. To verify the minimum pulse width effectively demonstrating the non-volatile characteristic of the channel current, the EPSC response is investigated at a pulse width less than 25 ms. Even when the pulse width is 5 ms or 10 ms, the non-volatile characteristics are exhibited. When the pulse width is 2.5 ms or less, however, non-volatile characteristics are greatly suppressed (Figure 2.6a,b). To quantify the non-volatile characteristic for the pulse width, the non-volatile weight ratio is defined and compare the values (Figure 2.6c). The transient temporal length becomes shorter as the pulse width becomes shorter, which is a significant advantage of fast operation speed. The non-volatile weight ratio, however, is less than 10 % at a pulse width of 1 ms and 2.5 ms. This limitation is due to the inherent property of the Li^+ electrolyte used in the $PFOTS_5$/ZnO EGT. The ionic conductivity of the water-in-bisalt/polymer Li^+ electrolyte is about 2.34×10^{-5} S cm^{-1}, which should be further improved for fast operation speed.[57], [58] (Figure 2.3d). It is known that when an electrolyte with high ionic conductivity is used in EGTs, more excellent synaptic functions can be exhibited even with a small driving voltage and a short pulse width.[59] Therefore, non-volatile characteristics can be induced even with the pulse width of less than 5 ms with electrolytes with higher ionic conductivity.

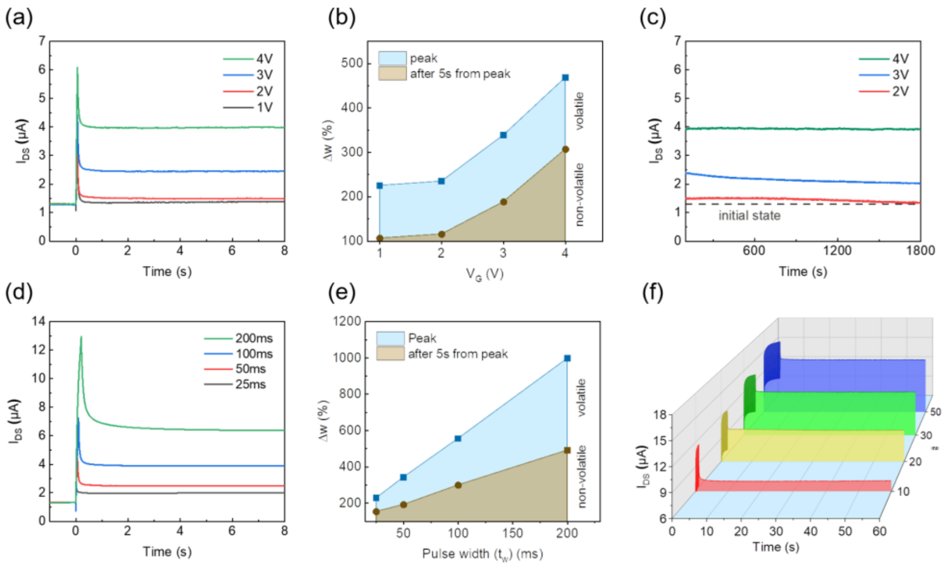

Figure 2.5. (a) EPSC responses by gate voltage pulse with amplitudes of 1 V to 4 V (t_w = 50 ms) at V_{DS} = 0.1 V. (b) Dependence of change ratio (Δw) of the channel current as a function of the amplitude of the gate voltage pulse. $\Delta w = ((I - I_0) / I_0) \times 100\%$, where I_0 and I are the channel current before a gate pulse (initial state) and after applying a gate pulse, respectively. The blue region and the brown region indicate the volatile channel current, and the non-volatile channel current, respectively. (c) Retention test as a function of the amplitude of the gate voltage pulse for 1800 s. (d) EPSC responses by gate voltage pulse with widths of 25 ms to 200 ms (V_G = 3V) at V_{DS} = 0.1 V. (e) Dependence of change ratio (Δw) of the channel current as a function of the width of the gate voltage pulse. (f) LTP characteristic as a function of the numbers of gate pulses (#) (T_{int} = 50 ms).

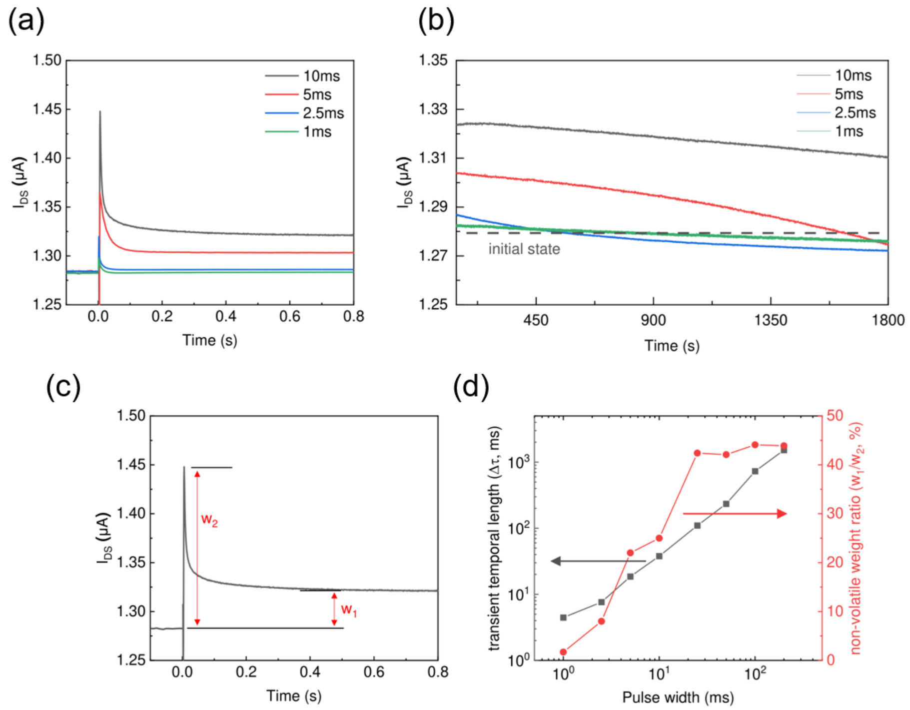

Figure 2.6. (a) EPSC responses by gate voltage pulse with widths of 1 ms to 10 ms (V_G = 3 V) at V_{DS} = 0.1 V. (b) Retention test as a function of the width of the gate voltage pulse for 1800 seconds. (c) Comparison of changes in transient temporal length and non-volatile weight ratio as a function of the pulse width at V_G = 3 V.

Paired-pulse facilitation (PPF), which is an essential factor for learning and memory functions, is demonstrated by 2 consecutive gate pulses. PPF is significantly related to decoding temporal information.[27], [60] Figure S6a shows PPF stimulated by 2 consecutive gate pulses (V_G = 3 V, t_w = 50 ms). The current induced by the second pulse (A_2) is larger than the first one (A_1) because accumulated Li^+ ions at the interface do not completely diffuse back in an interval time. PPF index is defined as

$$\text{PPF index} = \frac{A_2}{A_1} \times 100\ (\%), \qquad (2.2)$$

where A_1 and A_2 are the values of the channel current increased by the first and second positive gate pulses, respectively. As a result of measuring while changing the pulse interval (T_{int}), the PPF value was 132% for T_{int} = 20 ms and 114% for $T_{int} =$ 500 ms. As shown in Figure S6b, the PPF is related to the following double-exponential function

$$\text{PPF} = 1 + C_1 e^{-\frac{T_{int}}{\tau_1}} + C_2 e^{-\frac{T_{int}}{\tau_2}}, \qquad (2.3)$$

where C_1 and C_2 are the initial magnitudes of a fast and slow process, respectively, and τ_1 and τ_2 are characteristic relaxation times of each phase. For fitting data, C_1 and C_2 are estimated to be 12.80 % and 8.88 %, respectively. The characteristic relaxation times, τ_1 and τ_2 are respectively estimated to be 22.55 ms and 122.52 ms, which are comparable to those of biological synapses.[61]

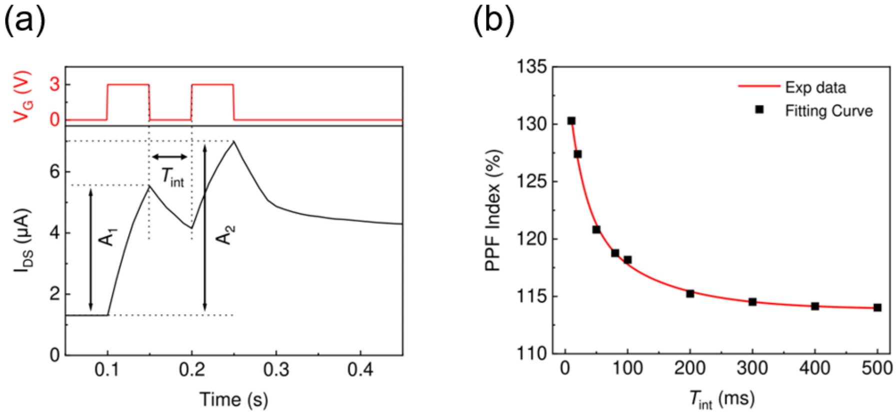

Figure 2.7. (a) Paired-pulse facilitation (PPF) by 2 consecutive gate pulses of 3 V amplitude and 50 ms pulse interval (T_{int}). (b) PPF dependence on T_{int}.

2.2.3. Effect of the magnitude of dipole moment

To investigate the role of FAS, I study the transfer characteristics of bare ZnO EGT and ZnO EGTs treated with FASs with three different lengths of fluoroalkyl chains (−CF_2−): Trimethoxy(3,3,3-trifluoropropyl)silane (TFP_0), 1H,1H,2H,2H-Perfluorooctyltriethoxysilane ($PFOTS_5$), and 1H,1H,2H,2H-Perfluorodecyltriethoxysilane ($PFDTS_7$). Detailed information on the types of FAS is in Table 2.1. At V_D = 0.1 V, the transfer curves of fabricated devices are shown in Figure 2.8a-d when the gate voltage is double swept from -4 V to 4 V with the scan rate of 0.8 V s^{-1}. The hysteresis windows (ΔV) of three types of FAS-treated ZnO EGTs are wider than that of bare ZnO EGT (1.27 V). Specifically, the ZnO EGT treated with FAS with longer fluoroalkyl chains has a wider hysteresis window. This wide hysteresis window in the transfer curve indicates non-volatile changes of the channel conductance, which is essential for emulating synaptic functions.[12], [62] The surface of bare ZnO is originally positively charged, but the surface of FAS-treated ZnOs is negatively charged by the surface dipole of FAS,[47] which is confirmed by the measurements of surface zeta potential (Figure 2.8e). Moreover, with the longer fluoroalkyl chains of FAS, the surface of FAS-treated ZnOs has a higher negative charge by the larger surface dipole moment.[63] The reason for the widened hysteresis is the changes in the movement of Li^+ ions in the electrolyte affected by an electric field.[64] The gate pulse is likely to strongly attract Li^+ ions to the surface of FAS-treated ZnO due to coulombic attraction between Li^+ ions and FAS. This effect appears more effectively on the surface of the channel with a high negative charge, resulting in widened hysteresis window in the transfer curve. EPSC responses of TFP_0/ZnO EGT and $PFDTS_7$/ZnO EGT show a similar tendency to the transfer curves (Figure 2.9a-d). TFP_0/ZnO EGT exhibits the value of the non-volatile current slightly increased from the initial state (30 % of the peak value) after the gate pulse, but $PFDTS_7$/ZnO EGT exhibits a highly increased value of the non-volatile current from the initial state (91 % of the peak value). Also, the transient temporal length is shorter as the length of the fluoroalkyl chains increases (Figure 2.9e). In this respect, the second-level write-read delay can be further reduced as the dipole moment of the FAS becomes larger.

To precisely verify the cause of lowered values of the channel current in FAS-treated EGTs, the areal capacitances of Li^+ electrolyte in each system are measured (Figure 2.8f). The capacitances of the electrolyte with FAS are 6.54 μF cm^{-2} for TPF_0, 1.87 μF cm^{-2} for $PFOTS_5$, and 1.05 μF cm^{-2} for $PFDTS_7$ at 0.2 Hz, which are much smaller than that of the electrolyte without FAS (26.78 μF cm^{-2} at 0.2 Hz). These values imply that the gating effect of Li^+ ions is weakened when FAS is on the channel-electrolyte interface because of the increased thickness of the EDL (due to the FAS interlayer).

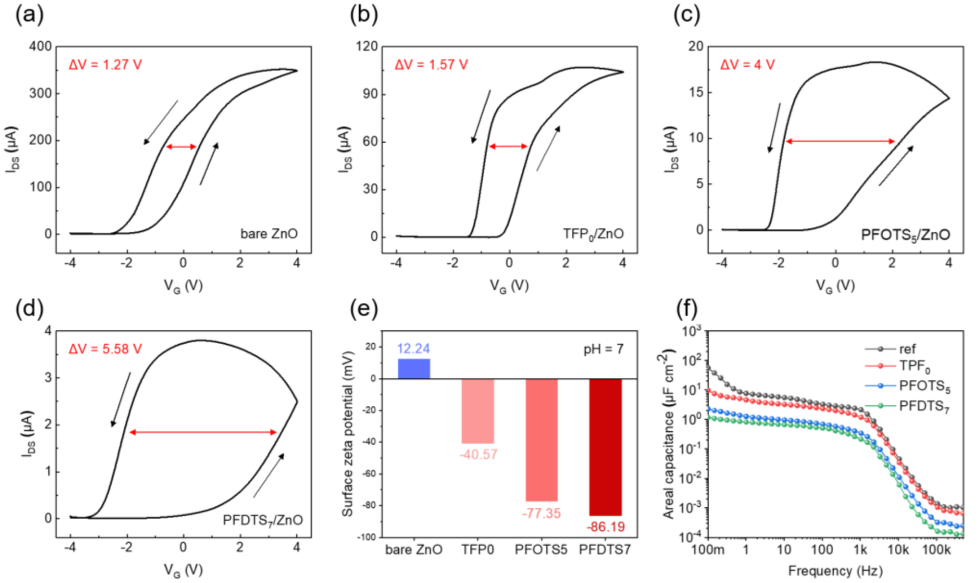

Figure 2.8. Transfer curves of (a) bare ZnO EGT, (b) Trimethoxy(3,3,3-trifluoropropyl)silane (TFP$_0$)-treated ZnO (TFP$_0$/ZnO) EGT, (c) 1H,1H,2H,2H-Perfluorooctyltriethoxysilane (PFOTS$_5$)-treated ZnO (PFOTS$_5$/ZnO) EGT, and (d) 1H,1H,2H,2H-Perfluorodecyltriethoxysilane (PFDTS$_7$)-treated ZnO (PFDTS$_7$/ZnO) EGT at a 0.8 V s^{-1} fixed scan rate (V_{DS} = 0.1 V). The voltage range of the hysteresis window (ΔV) is the full width at half maximum (FWHM) of the transfer curve. (e) Surface zeta potential of different FAS-treated ZnOs under a pH 7 solution. (f) Areal capacitances of Li$^+$ electrolyte with different FASs.

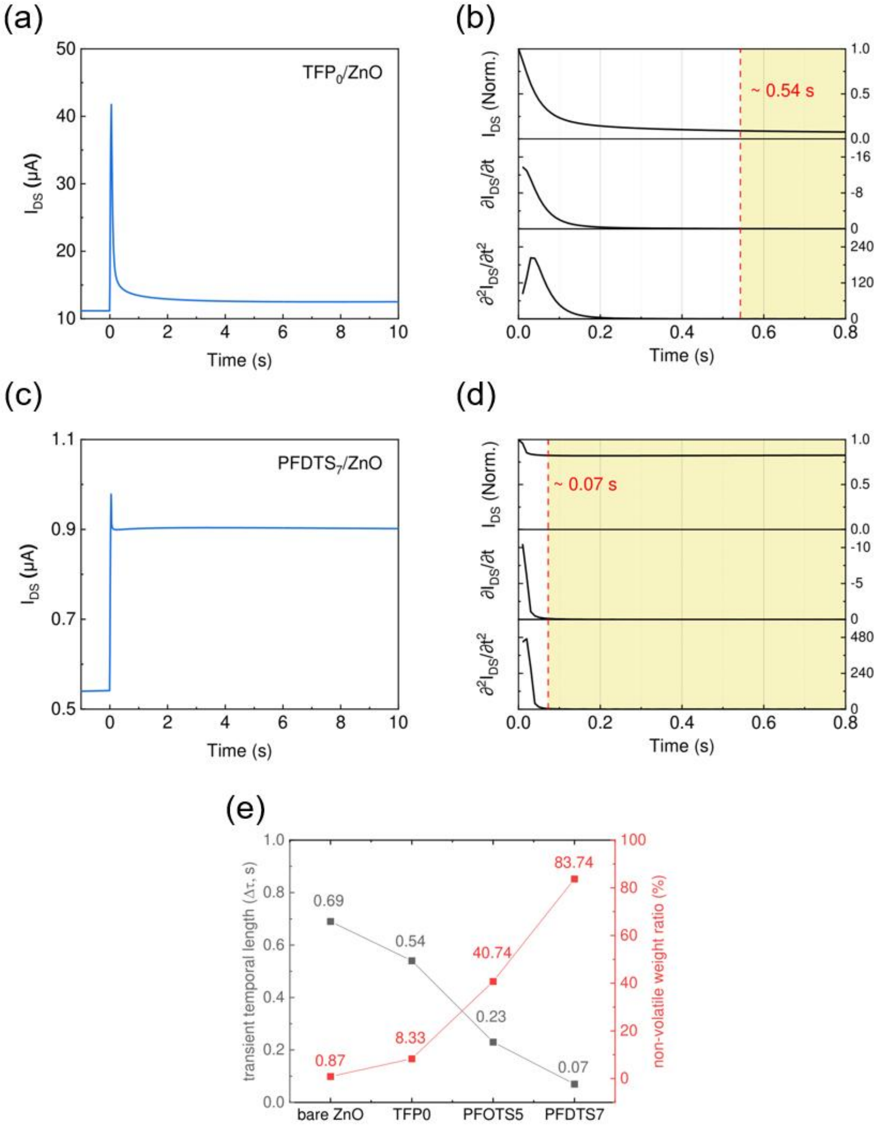

Figure 2.9. EPSC responses (left) and decay behaviors (right) of (a,b) TFP$_0$/ZnO EGT and (c,d) PFDTS$_7$/ZnO EGT (V_{DS} = 0.1 V, V_G = 3 V, t_w = 50 ms). (e) Changes of transient response time and non-volatile weight ratio by different FAS.

2.2.4. Elucidating working mechanism of FAS-modified EGT

The multiple non-volatile characteristics of the channel current may originate from the coulombic attraction between Li^+ ions and fluorocarbons ($C^{\delta+}{-}F^{\delta-}$ bonds) in $PFOTS_5$, resulting in holding Li^+ ions at $PFOTS_5$. Fluorine has a high electronegativity compared to carbon, the C−F bond, thus, is less covalent and the electron cloud in the C−F bond is directed toward fluorine.[65] Due to these properties, the dipole of the C−F bond can actively interact with other dipoles or alkali metal ions in its environment.[66], [67] Li^+ ion has a positive charge, and the Li^+ ions, thus, are possible to be trapped at $PFOTS_5$ by a positive gate pulse during forming the electrostatic force of coulombic attraction with the C−F bonds. Also, the Li^+ ions are possible to be de-trapped at $PFOTS_5$ when a negative gate pulse is applied. This trapping/de-trapping process of Li^+ ions is reversible and non-destructive because Li^+ ions are less likely to undergo a redox reaction with ZnO or $PFOTS_5$.[65], [68]

To investigate whether Li^+ ions are doped into the ZnO layer in $PFOTS_5$/ZnO EGT, I check the chemical composition of ZnO after applying positive gate bias of 4V amplitude for 10 s and removing the electrolyte film. Figure 2.10 shows O 1s XPS depth profile of the ZnO layer in $PFOTS_5$/ZnO EGT. If the major mechanism of non-volatile current is electrochemical doping, this process can be described by the following reaction [68]

$$\mathrm{xZnO} + (2\mathrm{x}+1)\mathrm{Li}^+ + (2\mathrm{x}+1)\mathrm{e}^- \leftrightarrow \mathrm{xLi_2O} + \mathrm{LiZn}_x, \tag{2.4}$$

Therefore, Li_2O will be formed as a product of the chemical reaction. Li_2O peak, however, does not appear in the depth profile; the amount of Li^+ ions where the electrochemical reaction occurred would be small. Therefore, the main cause of the changes in the channel conductance is the effect of EDL at the channel-electrolyte interface rather than the effect of electrochemical doping of Li^+ ions. The possibility of redox reaction between Li^+ ion and fluorine of $PFOTS_5$ is also low. Because the energy of the applied electric field is much weaker than the binding energy of the C−F bond, it is difficult to break the C−F bonds by gate pulses.[65]`

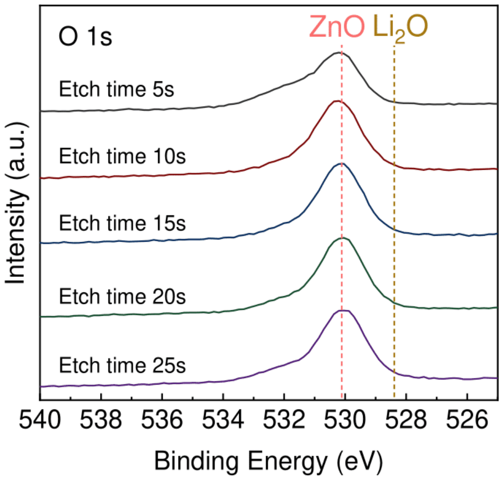

Figure 2.10. O 1s XPS spectra evolution of $PFOTS_5$/ZnO layer by different etch times. Judging from the XPS data, Li_2O peak (528.8 eV) is not identified.

Figure 2.11a-c shows the depth profile and elemental 3D depth mapping images of Li investigated through Time-of-flight Secondary Ion Mass Spectrometry (TOF-SIMS) measurement. Because of surface residue during peeling off the Li^+ electrolyte, the intensity of Li is observed in the initial state. In $PFOTS_5$/ZnO EGT, Li intensity increases in $PFOTS_5$ after applying positive bias. However, little difference is observed in bare ZnO EGT even after applying positive bias. These profiles are reasonable results, compared with the previous EPSC responses. Also, because electrons directly participating in binding in the C-F bond are sensitive to interacted cations, the effects of secondary columbic force can be confirmed by shifts of electron binding energy.[69] Figure 2.11d-f shows XPS spectra of F 1s and C 1s of the surface of $PFOTS_5$/ZnO. In the F 1s spectrum, the peak of the C−F ($C-F_2$ or $C-F_3$) bond is shifted from the initial state of 688.54 eV to 688.22 eV after applying positive bias (Figure 2.11d). Similar to F 1s spectra, binding energy shifts by columbic attraction are also observed in the C 1s peak (Figure 2.11e). After positive bias is applied, $C-F_2$ and $C-F_3$ bonds are shifted from 291.05 eV to 290.91 eV and from 293.37 eV to 293.26 eV which is similar to F 1s spectra. The phenomenon of negative peak shifts of binding energy can be considered as the electron density in the C−F bond is increased in fluorine by the positive charge density of Li^+ ions.[69], [70] C−C, C−Si, C−O bond peaks are constant due to insensitivity to the columbic attraction (Figure 2.11f).[71] These results are indirect evidence that Li^+ ions are trapped between the FAS.

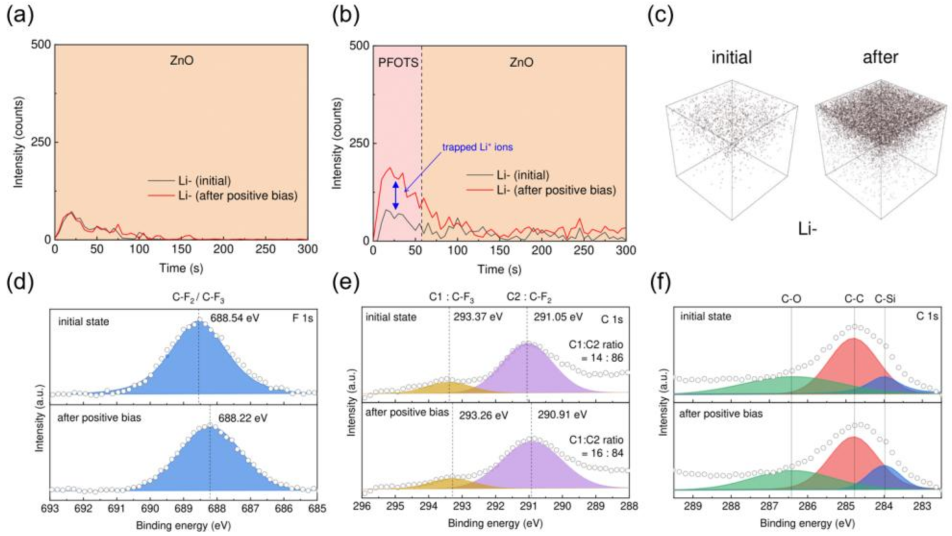

Figure 2.11. Li elemental depth profile of (a) bare ZnO layer and (b) PFOTS$_5$/ZnO layer under initial state and after applying positive gate bias of 4V amplitude for 10 s. (c) Li 3D mapping image of PFOTS$_5$/ZnO layer. Sputtering rate: 0.025 nm s^{-1}. d) F 1s XPS spectrum of PFOTS$_5$/ZnO layer. (e,f) C 1s XPS spectrum of PFOTS$_5$/ZnO layer. Each peak is deconvoluted as a Gaussian-Lorentzian function.

The dynamics of the Cs^+ ion are investigated to elucidate the ion-trapping mechanism (Figure 2.12). The major differences between the Cs^+ and Li^+ ions are the ionic radius and charge density.[72] In the case of $PFOTS_5$/ZnO EGT with the Cs^+ electrolyte, the transfer curve exhibits a small and positive-shifted hysteresis (Figure 2.12a), and EPSC response exhibits a value of the non-volatile current which is almost close to the value of the initial state (Figure 2.12b,c). Li^+ ions are likely to be easily penetrating between fluoroalkyl chains ($-CF_2-$) due to their small ionic radius (~ 90 pm, 6-coordination number) and are strongly trapped at C−F bonds due to a high charge density of Li^+ ion.[73]–[75] Cs^+ ions, however, are less likely to penetrate between fluoroalkyl chains because of their larger ionic radius (~ 181 pm). Also, coulombic attraction between Cs^+ ions and C−F bonds is much weaker than between Li^+ ions and C−F bonds because of a low charge density of Cs^+ ions. The ion-trapping effect of Cs^+ ions in FAS with fluoroalkyl chains, therefore, is likely to be much weaker than that of Li^+ ions. Although LTP characteristics can be induced in EPSC response if the amplitude or width of the gate pulse applied to the Cs^+ electrolyte is sufficiently large, the retention time is much shorter compared to the Li^+ electrolyte (Figure 2.12d). In addition, EPSC response of Li^+ ions in ZnO EGTs treated with Triethoxyoctylsilane (TEOOS) SAM which has 7 alkyl chains in the backbone is investigated (Figure 2.13). Triethoxyoctylsilane (TEOOS) has 7 alkyl chains in the backbone. To confirm the effect of ion-trapping in the alkyl chains, the transfer curve and EPSC responses of TEOOS/ZnO EGT are measured. Compared with $PFOTS_5$/ZnO EGT, the transfer curve for TEOOS/ZnO EGT shows a narrow hysteresis window. Also, the non-volatile characteristic of channel current does not appear in EPSC response by gate pulses (Figure 2.13c,d). Unlike the fluorocarbon

($C^{\delta+}$−$F^{\delta-}$ bond), the electron cloud in the hydrocarbon ($C^{\delta-}$−$H^{\delta+}$ bond) is directed toward carbon. The coulombic repulsion, therefore, will be occurred between the Li^+ ions and alkyl chains (−CH_2−). From these results, the ion-trapping effect between fluoroalkyl chains plays a key role in exhibiting the multiple non-volatile memory characteristics of the channel current.

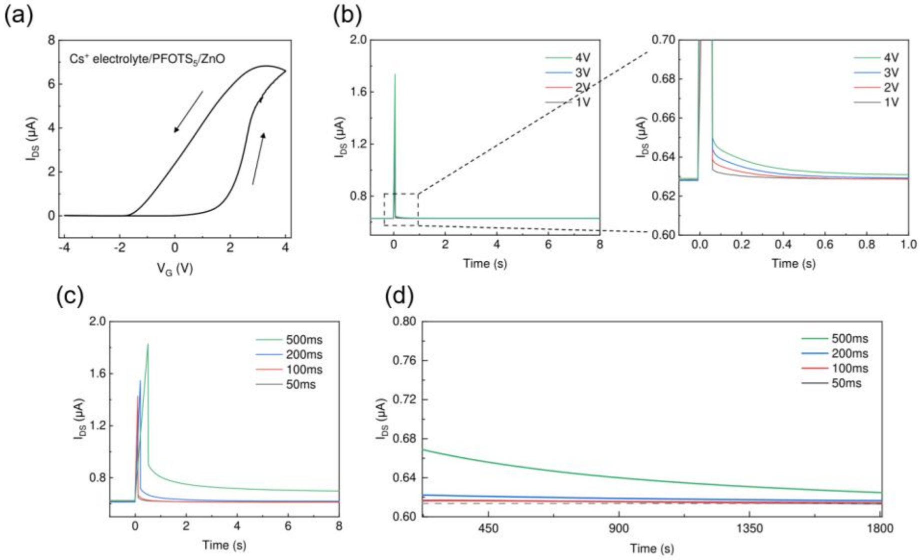

Figure 2.12. (a) Transfer curve of PFOTS$_5$/ZnO EGT with Cs$^+$ electrolyte at a 0.8 V s^{-1} fixed scan rate. and (b) EPSC responses by gate voltage pulse with amplitudes of 1 V to 4 V (t_w = 50 ms) at V_{DS} = 0.1 V. (c) EPSC responses by gate voltage pulse with widths of 50 ms to 500 ms (V_G = 3V) at V_{DS} = 0.1 V. (d) Retention test as a function of the width of the gate voltage pulse for 1800 seconds. Dash line: initial state.

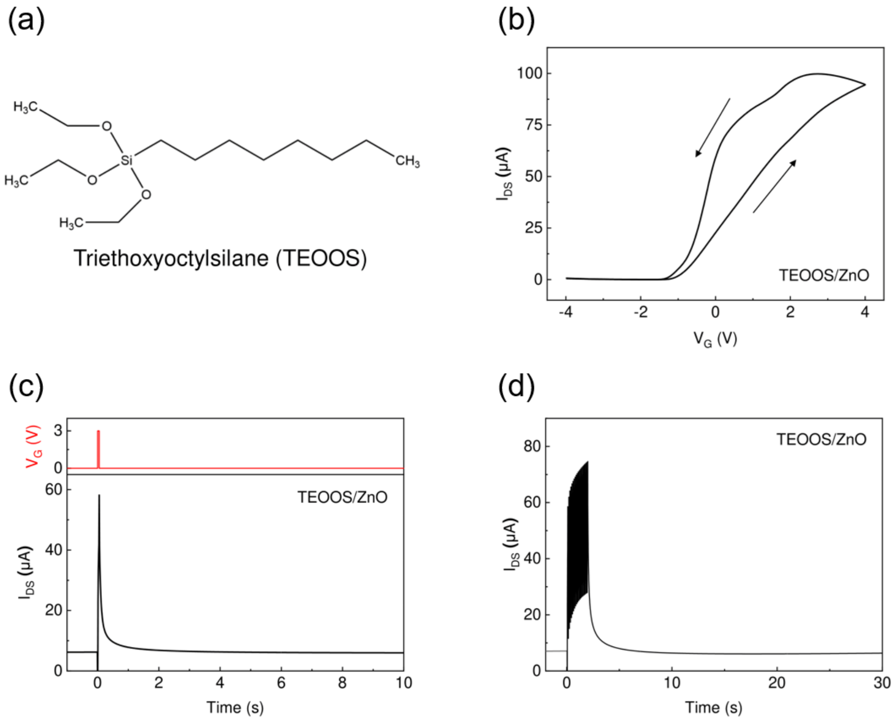

Figure 2.13. (a) Chemical structure of Triethoxyoctylsilane (TEOOS). (b) Transfer curve of TEOOS-treated ZnO (TEOOS/ZnO) EGT at a fixed rate of 0.8 V s^{-1}. (c) EPSC response of TEOOS/ZnO EGT by a single gate pulse (V_G = 3 V, t_w = 50 ms) at V_{DS} = 0.1 V. (d) EPSC response of TEOOS/ZnO EGT by 20 consecutive gate pulses (T_{int} = 50 ms).

The mechanism for the role of $PFOTS_5$ is explained in Figure 2.14. In bare ZnO EGT, when a positive gate pulse is applied to the electrolyte, the electric field accumulates Li^+ ions toward the surface of the channel. After the gate pulse, the accumulated Li^+ ions are rapidly dissipated at the interface to return to the equilibrium state of the electrolyte (Figure 2.14a). Therefore, a peak appears in EPSC response due to the instantaneously formed EDL by a gate pulse, and then the channel current returns to the value of the initial state. In $PFOTS_5$/ZnO EGT, however, because ion-trapping sites exist in $PFOTS_5$, some of the Li^+ ions cannot return to the bulk of the electrolyte and are trapped between fluoroalkyl chains even after the gate pulse is removed (Figure 2.14b). When consecutive gate pulses are applied, the more increased value of the non-volatile current from the initial state appeared because more amounts of Li^+ ions are trapped between fluoroalkyl chains. The number of Li^+ ions trapped between the fluoroalkyl chains, therefore, is a major factor in exhibiting the magnitude of the non-volatile channel currents. Also, fluoroalkyl chains can sequentially trap Li^+ ions by consecutive gate pulses, resulting in sequential increments of the non-volatile channel current.

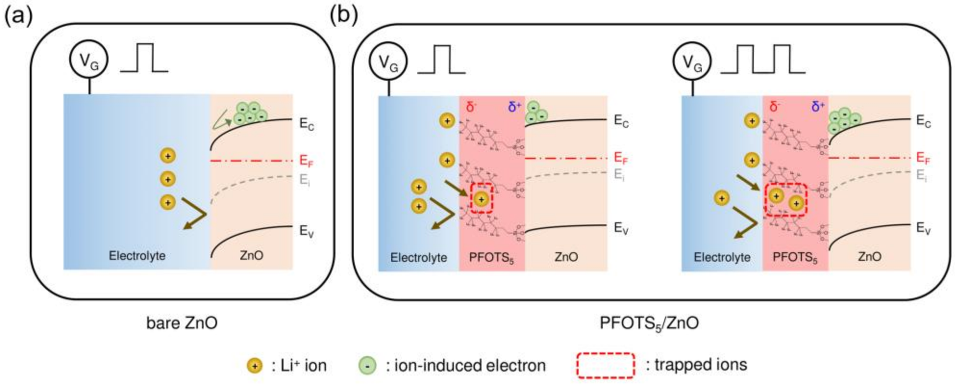

Figure 2.14. The dynamics of Li^+ ion of (a) bare ZnO EGT and (b) $PFOTS_5$/ZnO EGT. After a positive gate pulse is applied to the electrolyte in bare ZnO EGT, Li^+ ions quickly return to the equilibrium state, but $PFOTS_5$/ZnO EGT exhibits a non-volatile channel current because some Li^+ ions cannot return to the equilibrium state due to ion-trapping sites at $PFOTS_5$. Moreover, when gate pulses are consecutively applied to the electrolyte, more amounts of Li^+ ions are sequentially trapped in $PFOTS_5$, resulting in a higher excited non-volatile current.

2.2.5. Conductance update in FAS-modified EGT

Controlling multi-level channel conductance is essential to perform analog neuromorphic computing.[76] As shown in Figure 2.15a, channel conductance update of PFOTS$_5$/ZnO EGT is measured by 60 gate pulses of 4 V amplitude for potentiation and 60 gate pulses of -4 V amplitude for depression (T_{int} = 50 ms, t_w = 50 ms). The maximum (G_{max}) and minimum (G_{min}) conductance during conductance update in PFOTS$_5$/ZnO EGT are 207.80 μS and 14.74 μS, respectively, and the dynamic range (G_{max}/G_{min}) is 14.10. Also, based on the cycle of conductance update, I calculate the nonlinearity (NL) for potentiation (NL_LTP) and depression (NL_LTD). Conductance update with the number of pulses is described as follows[77]

$$G_{LTP} = \mathrm{B}\left(1 - \exp\left(-\frac{P}{A_P}\right)\right) + G_{min}, \tag{2.5}$$

$$G_{LTD} = \mathrm{B}\left(1 - \exp\left(\frac{P-P_{max}}{A_D}\right)\right) + G_{max}, \tag{2.6}$$

$$\mathrm{B} = \frac{G_{max}-G_{min}}{1-\exp\left(\frac{-P_{max}}{A}\right)}, \tag{2.7}$$

where G_{LTP} and G_{LTD} are the conductance of potentiation and depression, respectively, P_{max} is the maximum number of gate pulses, and A_P and A_D are the nonlinear parameter for conductance update of potentiation and depression, respectively. The nonlinear parameters of PFOTS$_5$/ZnO EGT are A_P = 0.378, and A_D = 0.581. Using these values, the NL corresponding to the nonlinear parameter can be obtained. The obtained NL_LTP and NL_LTD are 3.07 and 2.09, respectively. Also, PFOTS$_5$/ZnO EGT operates stably even during 100 cycles without degradation (Figure 2.15b). The average cycle-to-cycle variation, $\sigma/\Delta G$—where σ is the standard deviation of conductance update and ΔG is the mean of the conductance changes— of 100 cycles is 4.3 % for LTP and 3.2 % for LTD, which indicates the deviation of conductance values from cycle to cycle is small (Figure 2.15c). Also, the device-to-device distribution of nonlinearity and the conductance of 50 devices are shown in Figure 2.15d,e. Here, the statistical analysis in device-to-device distribution is based on the nonlinearity and conductance values in the 5th cycle of conductance update for 50 devices. The nonlinearity of $PFOTS_5$/ZnO EGTs is 3.02 ± 0.19 for LTP and from 2.01 ± 0.14 for LTD. The conductance of $PFOTS_5$/ZnO EGTs is 203.72 ± 14.06 μS for maximum value and 15.06 ± 3.15 μS for minimum value. These distributions indicate that $PFOTS_5$/ZnO EGTs have low deviation and good uniformity.[62]

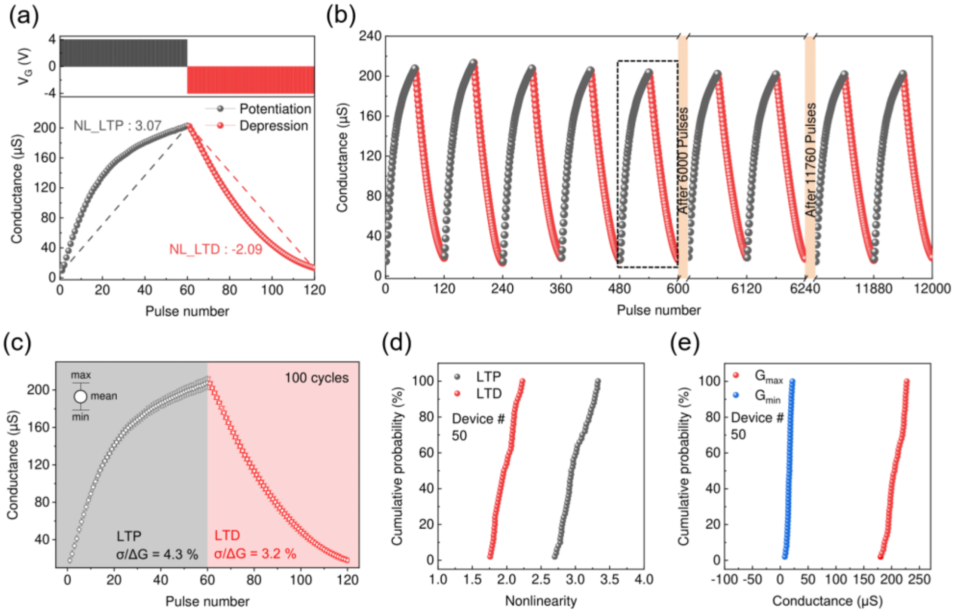

Figure 2.15. (a) Channel conductance update by consecutive gate pulses of 60 potentiation and 60 depression ($V_G = 4$ V for potentiation, $V_G = -4$ V for depression, $t_w = 50$ ms, $T_{int} = 50$ ms). (b) 100 cycles of conductance update measured under the same condition with (a). The dashed square indicates the 5th cycle of conductance update, shown in (a). (c) The cycle-to-cycle variation during 100 cycles. The calculated variation of conductance is based on (b). The 50 device-to-device distribution of (d) nonlinearity of potentiation (black) and depression (blue) and (e) maximum (red) and minimum (blue) conductance.

Figure 2.16 shows the differences in conductance update of FAS-treated ZnO EGTs by identical pulses. The longer fluoroalkyl chains of FAS enable a much closer to linear conductance update compared to the case where the fluoroalkyl chains are none or short (Figure 2.16a,b). These results are explained as the number of ion-trapping sites of FAS increase with increasing the length of fluoroalkyl chains. FAS with longer fluoroalkyl chains, therefore, can sequentially trap more amounts of Li^+ ions. Also, the dynamic range of conductance update decreases with the length of fluoroalkyl chains increases (Figure 2.16c). TFP_0/ZnO EGT, and $PFOTS_5$/ZnO EGT show a high dynamic range (> 10), but the $PFDES_7$/ZnO EGT shows a low dynamic range (8.54). The low dynamic range is insufficient to have a high recognition accuracy in simulations of ANN.[8], [77]

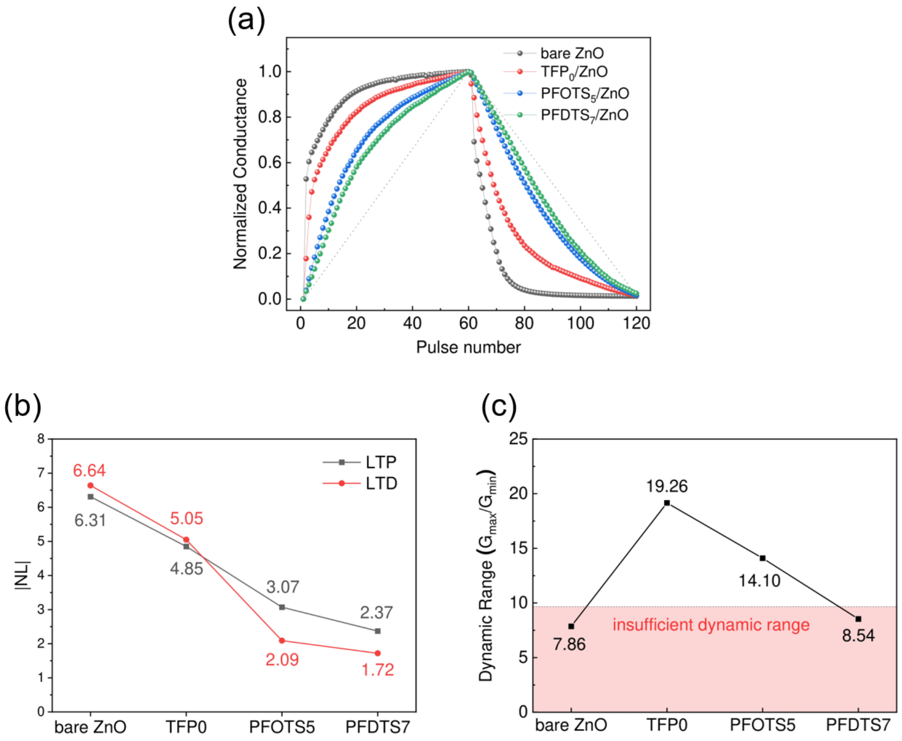

Figure 2.16. (a) Comparison of conductance update of FAS-treated EGTs by identical pulses. The parameters compared through the conductance data are (b) nonlinearity and (c) dynamic range.

Linearity of conductance update can be also improved by consecutive gate pulses of incrementally increasing or decreasing amplitude.[78], [79] As shown in Figure 2.17a, when channel conductance update in PFOTS$_5$/ZnO EGT is measured by 60 gate pulses of incrementally increasing (from 1.64 V to 4 V, increment: 0.04 V) or decreasing (from -1.64 V to -4 V, decrement: -0.04 V) amplitude, the absolute values of linearity of LTP and LTD change from 3.07 to 1.21 and from 2.09 to 0.83 compared with identical gate pulses, respectively. This difference is because, in the case of identical gate pulses, the concentration of Li$^+$ ions at the channel-electrolyte interface is abruptly saturated or dissipated over the number of gate pulses. When the amplitudes of gate pulses, however, are incrementally increased or decreased, EDL is gradually forming or relaxing at the channel-electrolyte interface, thereby improving linearity. In the case of non-identical gate pulses, the dynamic range does not change much because the concentration of Li$^+$ ions at the interface at the beginning and the end of conductance update is similar to the case of identical gate pulses (G_{max} = 198.63, G_{min} = 14.70, Dynamic range = 13.51). PFOTS$_5$/ZnO EGT also operates stably during 100 cycles by non-identical gate pulses, as shown in Figure 2.17b.

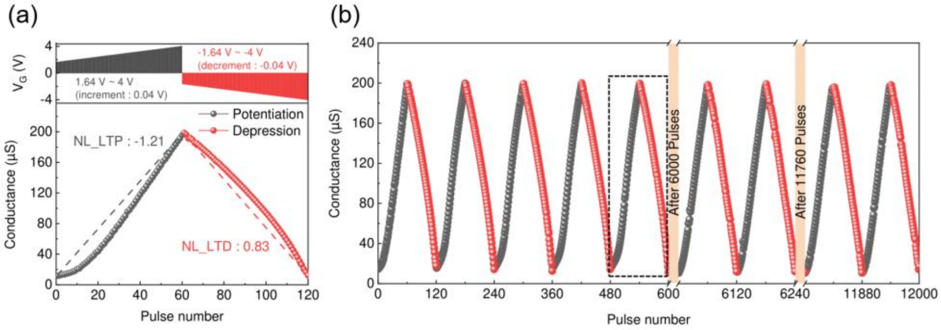

Figure 2.17. (a) Channel conductance update by non-identical consecutive gate pulses of 60 potentiation and 60 depression (V_G from 1.64 V to 4 V with increment of 0.04 V for potentiation and from -1.64 V to -4 V with decrement of -0.04 V for depression, t_w = 50 ms, T_{int} = 50 ms). (b) 100 cycles of conductance update measured under the same condition with (a).

2.2.6. Inference tasks using artificial neural network

Based on device characteristics of PFOTS$_5$/ZnO EGT, multi-layer perceptron (MLP) simulation, a class of feedforward ANN, is conducted to verify whether the device is suitable for neuromorphic computing. In the simulation, the recognition accuracy is tested based on the MNIST data set of 20 × 20 pixels handwritten digits. The 3-layer ANN used in the simulation consists of 400 input neurons corresponding to 20 × 20 MNIST digit pixels, 125 hidden neurons, and 10 output neurons corresponding to 10 classes of digits, 0 - 9 (Figure 2.18a). The diagram of the cell array circuit corresponding to the configured ANN is shown in Figure 2.18b. The accuracy of PFOTS$_5$/ZnO EGT by identical gate pulses is up to 89.71 %, and the accuracy by non-identical gate pulses is up to 91.97 %, which are close to the ideal device of 92.97 % (Figure 2.18c,d). The recognition accuracies of the bare ZnO EGT and other FAS-treated ZnO EGTs are also identified through the simulation using ANN. The recognition accuracies of bare ZnO EGT, TFP$_0$/ZnO EGT, and PFDTS$_7$/ZnO EGT are 14.43 %, 70.95 %, and 42.60 %, respectively (Figure 2.19). In addition, PFOTS$_5$/ZnO EGT has a good capability of data storing, confirmed through data retention tests of the 32 x 32 binarized image (Figure 2.18e).[80] The arrays of PFOTS$_5$/ZnO EGTs maintain programmed input data over 300 s because of its noticeably improved retention characteristic. The programmed input data of the arrays of bare ZnO EGTs, however, is degraded abruptly. Bare ZnO EGTs lose most of the input data after 15 s and almost lose input data after 30 s. These results indicate that PFOTS$_5$/ZnO EGT is considerably suitable for use in neuromorphic computing applications.

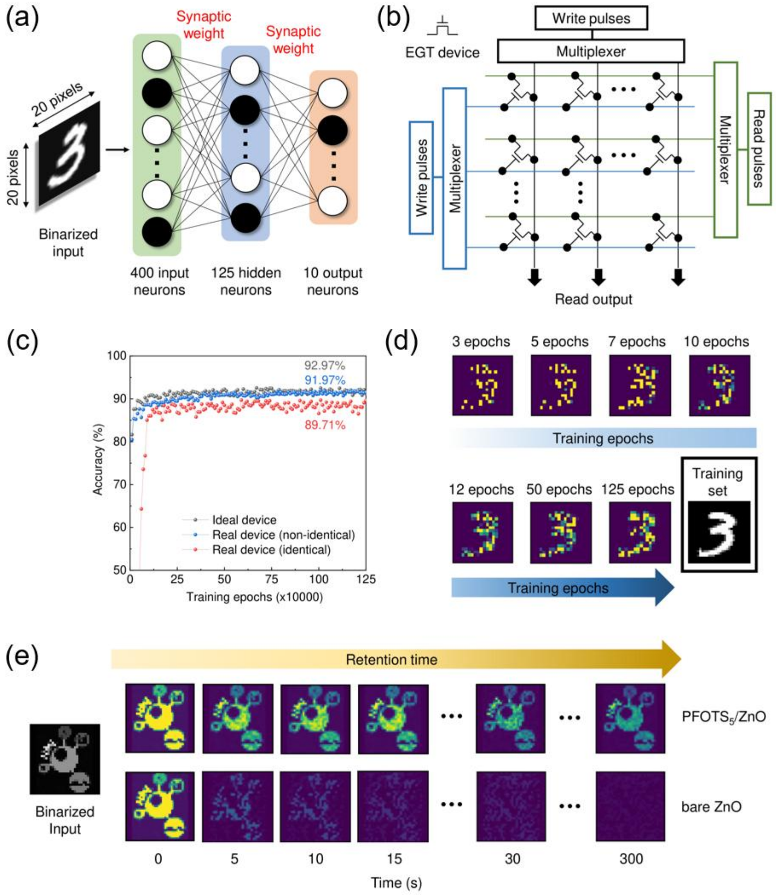

Figure 2.18. (a) Schematic illustration of 3-layer artificial neural network (ANN) consisted of 400 input neurons, 125 hidden neurons, and 10 output neurons for image recognition simulation. A 20 × 20 pixel Modified National Institute of Standards and Technology (MNIST) data set of handwritten digits is used for simulation. (b) Circuit diagram showing a synapse layer composed of EGT arrays and the peripheral circuit. (c) The recognition accuracy of the ideal device (gray) and real device (red, blue) in simulations using ANN. The accuracy of the ideal device is a case where nonlinearity is 0, which indicates conductance update with ideal linearity and symmetry. (d) Visualization images of the accuracy of each epoch during the learning process in simulation. (e) 32 × 32 binarized image programming in arrays of PFOTS$_5$/ZnO EGTs and bare ZnO EGTs and their data retention test

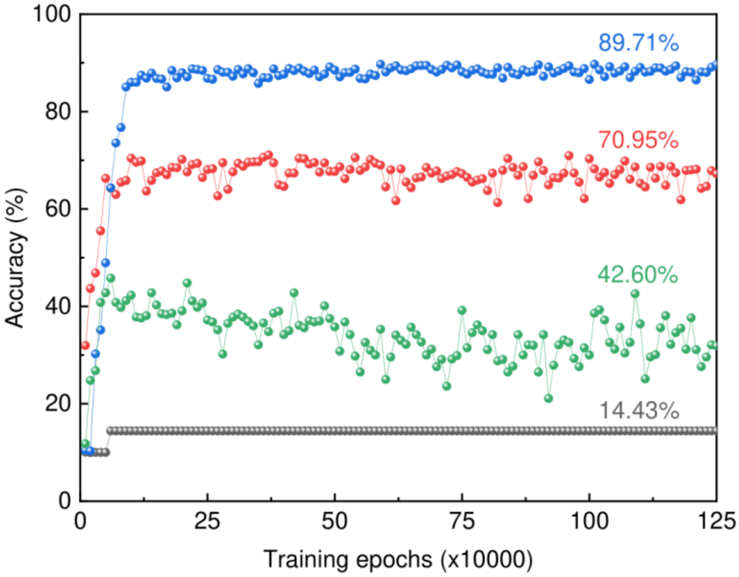

Figure 2.19. Recognition accuracies of FAS-treated ZnO EGTs in simulations using ANN. bare ZnO EGT (black), TFP_0/ZnO EGT (red), $PFOTS_5$/ZnO EGT (blue), $PFDTS_7$/ZnO EGT (green).

2.2.7. Experimental method

Materials: Boron-doped p^{++} Si wafers (< 0.001 Ω) with 200 nm-thick thermally grown SiO_2 were used as the substrate. Zinc nitrate hexahydrate ($Zn(NO_3)_2·6H_2O$, > 99 % purity), sodium hydroxide (NaOH, 99.99 % purity), lithium trifluoromethanesulfonate (LiOTf, 99.995 % purity), Poly(ethylene glycol) dimethacrylate (PEGDMA, M_w ~ 550), 2-hydroxy-2-methylpropiophenone (HOMPP, 97 %), and Triethoxyoctylsilane (TEOOS, 97.5 % purity) were purchased from Sigma-Aldrich. Ammonium hydroxide (NH_4OH, 25-28 % purity) were purchased from Daejung Chemicals. Lithium bis(trifluoromethanesulfonyl)imide (LiTFSI, > 98 % purity), Cesium(I) bis(trifluoromethanesulfonyl)imide (CsTFSI, > 98 % purity) and trimethoxy(3,3,3-trifluoropropyl)silane (TFP_0, > 98 % purity) were purchased from TCI. 1H,1H,2H,2H-Perfluorooctyltriethoxysilane ($PFOTS_5$, 97 % purity) and 1H,1H,2H,2H-Perfluorodecyltriethoxysilane ($PFDTS_7$, 97 %) were purchased from Alfa Aesar.

Preparation of the ZnO solution: 0.5 M $Zn(NO_3)_2·6H_2O$ was dissolved in 15 mL de-ionized (DI) water. 2.5 M NaOH in 10 mL DI water was added to the ZnO solution. After mixing the prepared solution, the solution was centrifuged five times with DI water at 5000 rpm for 5 min. After centrifugation, the precipitate was collected, and dissolved in 20 mL NH_4OH with 25 mL DI water.

Preparation of Li^+ and Cs^+ electrolytes: This method of the Li^+ electrolyte followed a previously reported method.[46] 21 M LiTFSI and 7 M LiOTf were dissolved in DI water, and PEGDMA was added at a weight ratio of 1:1 with the solution. To solidify by UV curing, HMOPP was added in a 2 wt% to the mixture.

Then the electrolyte mixture was stirred for 6 hr vigorously. The prepared electrolyte was stored in a refrigerator at 4 °C. In the case of Cs^+ electrolyte, 21 M CsTFSI was added instead of Li salts, and the other procedures were the same.

Fabrication of FAS-treated ZnO EGTs: The SiO_2/Si substrate was cleaned by subsequent sonication in detergent for 15 min, DI water rinsing for 15 min, sonication in acetone, isopropanol for 15 min each, followed by UVO treatment for 20 min. The prepared ZnO solution was spin-coated at 1000 rpm for 40 s on the SiO_2/Si substrate. The substrate was heated to 300 °C for 1 h to sinter the ZnO films. The thickness of the ZnO layer was about ~ 16 nm. After then, the channel region was patterned using photolithography and a wet etching process to define the channel region. The Al source, drain, and side gate electrodes were deposited to a thickness of 100 nm using thermal evaporation. The distance between the side gate electrode and the ZnO channel was 500 μm. The channel width and length were 500 μm and 100 μm, respectively. To deposit FAS on the surface of the ZnO channel, the fabricated device was subjected to UVO treatment for 20 min using a metal mask to exposure only the channel area. Subsequently, UVO-treated ZnO transistors and an open glass vessel containing 50 μL of FAS (TFP_0, $PFOTS_5$, and $PFDTS_7$) were placed in a sealed Teflon desiccator and heated at 200 °C for 30 min, followed by subsequent sonication in IPA for 15 min and DI water for 5 min to remove FAS residues. After FAS deposition, the prepared electrolyte mixture was applied between the channel and the gate electrode using the drop-casting method and then cured with a UV lamp at 365 nm (600 mJ cm^{-2}) for 10 s.

Device characterizations and measurements: The roughness of ZnO films is investigated using AFM (XE100, PSIA). Especially, the surface of the SAM layers was examined utilizing low-noise AFM. The topological AFM images were obtained in tapping mode using a silicon probe with a cantilever spring constant of 42 N m^{-1}. To characterize the surface potential of the ZnO and FAS-treated ZnO, zeta potential measurement (SurPASS™ 3, Anton Paar) was performed under a pH 7 solution. The areal capacitance of electrolytes was measured using electrochemical impedance spectroscopy under AC voltage bias of 250 mV (Biologic, VSP). The bandgap of ZnO films was measured from 300 to 800 nm using ultraviolet-visible (UV-vis) spectroscopy (Lambda 35, PerkinElmer). The chemical properties, valence band maximum, and work function of FAS-treated ZnO films were measured from X-ray photoelectron spectroscopy (XPS) and ultraviolet photoelectron spectroscopy (UPS) (AXIS SUPRA, Kratos). Work functions of each sample were obtained from a 21.22 eV He (I) excitation. ToF-SIMS analysis with the depth profile mode was performed to evaluate the ion-trapping tendency of Li^+ ions at a pressure below 3.8×10^{-9} Torr (TOF.SIMS-5, ION-TOF). A Bi^+ (30 keV, 1 pA) ion beam was used as the primary source for detecting the composition of facile-section, and sputtering with a Cs^+ ion beam (2 keV, 150 nA) was used for depth profiling analysis (analysis area; 100 × 100 μm^2, etching area; 400 × 400 μm^2). The transfer characteristics and pulse measurements of all devices were characterized by Keysight 2902B source/measure unit. STDP of $PFOTS_5$/ZnO EGT was characterized by Keithley 4200 semiconductor parameter analyzer.

Simulations of artificial neural networks: The simulation was conducted on open-source code “NeuroSim ver. 3.0” in a Linux system.[77] The recognition accuracy of 3-layer ANN with a size of 400 × 125 × 10 was calculated. A 20 × 20 MNIST digit with binarized black and white patterns was used as ANN input. The device properties, including non-ideal factors used in the simulation, are the dynamic range, the number of conductance levels, device-to-device variation, cycle-to-cycle variation, nonlinearity, write pulse voltage, and write pulse width. After training one million patterns randomly selected from 60,000 training images from the training set, the recognition accuracy is tested with 10,000 images from the testing set. The number of training images per epoch is 10,000, and the training is conducted for a total of 125 epochs.

Image programming and retention test*:* The 32 × 32 black-and-white binarized images were programmed into different EGT arrays using a closed-loop algorithm based on Python 3.10.[80] The 128-scale pixel values were mapped to conductance values between the maximum and minimum conductance of each device. Both the raw conductance value and the binarized image based on 128-scale values were used to compare data retention characteristics between bare ZnO EGTs and PFOTS$_5$/ZnO EGTs. Data in Figure 2.15d,e were used for deviation of devices during conductance update.

Statistical analysis: Statistical analysis was performed based on the standard normal distribution. The cycle-to-cycle variation (Figure 2.15c) was calculated based on 100 cycle data of PFOTS$_5$/ZnO EGT (Figure 2.15b). The calculated average variation is $\sigma/\Delta G$, where σ is the standard deviation of the conductance update and ΔG is the mean of conductance change upon a given pulse. The standard deviation is $\sigma = \sqrt{\frac{1}{N}\sum_{i=1}^{N}(x_i - \mu)^2}$, where N is the number of cycles (N = 100 in this work), x_i is the conductance of each pulse, and μ is the mean conductance of each cycle. The device-to-device distribution (Figure 2.15d,e) was calculated based on the 5th cycle of conductance update for each 50 devices (N = 50). Conditions of measurement during conductance update are the same as in Figure 2.15a,b. Data presentation was expressed as $\mu \pm \sigma$. The mean and standard deviation were calculated as same as in Figure 2.15c, where N is the number of devices, x_i is the conductance and linearity of each device, and μ is the average conductance and linearity of each device.

2.3. Verification of the ion-dipole force induced by F-SAM

2.3.1 Rationale for changing F-SAM

As presented in Section 2.2, fluorinated self-assembled monolayer (F-SAM) exhibits strong coulombic attraction with lithium ions, suggesting their potential use as interlayers in artificial synapses. Here, the differences in the electrical characteristics of artificial synapses by varying the fluoroalkyl chains in F-SAMs.

(i) As the fluoroalkyl chains of the F-SAMs are longer, the dipole moment increases (i.e., the negative charge strengthens), intensifying the attraction force with lithium ions. This implies an enhancement in nonvolatility and linearity during conductance updates.

(ii) As F-SAMs are electrical insulators, the overall capacitance of the electrolyte decreases as the thickness of the EDL increases. This also implies that as the dipole moment of the F-SAMs strengthens, it can further lower the off current.

(iii) As the attraction force between F-SAM and lithium ions strengthens, the write-read delay decreases during writing phase.

F-SAMs can have various types of anchor groups; in this section, the F-SAM with a phosphonic acid group is selected, as it can form the strongest bonds with metal oxides. Additionally, among the commercially available F-SAMs with the longest fluoroalkyl chain, F_{21}-DDPA is selected due to its largest dipole moment and its strong interactions with lithium ions.

Therefore, F_{21}-DDPA forms robust bonds with metal oxides, ensuring strong interfacial adhesion. This improves the mechanical stability and durability of the composite material, which is crucial for maintaining structural integrity under several operational conditions for various applications. Also, F_{21}-DDPA exhibits excellent thermal and chemical stability, making it suitable for applications under harsh conditions. So that this stability ensures the reliability of the device. For these reasons, F_{21}-DDPA was selected as the interlayer in this study.

2.3.2. Device configuration

Figure 2.20a shows a schematic illustration of an F_{21}-DDPA-modified lithium EGT. For convenience, I will refer to the lithium EGT with F_{21}-DDPA as FLEGT and the device without F_{21}-DDPA as LEGT. The channel layer is sputtered a-IGZO, and aluminum is used for the source and drain, and side-gate electrode. Subsequently, F_{21}-DDPA was deposited by immersing the constructed a-IGZO EGT in the prepared F_{21}-DDPA solution. To verify the uniform deposition of F_{21}-DDPA on the surface of a-IGZO, the surface roughness of each film through atomic force microscope (AFM) measurements is investigated. As shown in Figure 2.21, the small difference in root-mean-square roughness on the a-IGZO surface before (0.451 nm) and after F_{21}-DDPA deposition (0.504 nm) indicates uniform deposition of F_{21}-DDPA. After deposition, water-in-bisalt lithium electrolyte was applied on the a-IGZO and side-gate. The device of the optical microscope image is presented in Figure 2.22. As observed in the C 1s XPS spectrum shown in Figure 2.20b, the strong peaks of fluoroalkyl chains (–CF_2–, 290.5 eV) and trifluoromethyl group (–CF_3, 292.8 eV) peaks of F_{21}-DDPA were distinctly found.[81]

One of the notable physical properties of F_{21}-DDPA is to induce a negatively charged surface on the material.[82] Figure 2.20c shows the surface zeta potential of the surface of each respective film at pH = 7. While the bare a-IGZO exhibited a positively charged surface (9.42 mV), the surface of F_{21}-DDPA/a-IGZO demonstrated a transition to a notable negatively charged surface (-43.56 mV), attributable to the dipole moment of F_{21}-DDPA. This effect was also confirmed through the double-swept transfer curve by applying gate bias (V_G) from -3 to 3 V, presented in Figure 2.23. It is evident that FLEGT exhibited a wider hysteresis window compared to LEGT. This suggests the existence of strong electrostatic attraction between the negatively charged F_{21}-DDPA/a-IGZO surface and positively charged lithium ions. Consequently, the widened hysteresis window signifies potential advantages in terms of the characteristics of the memory device.[83] As evidenced by the repetitive V_G-induced transfer curves presented in Figure 2.24, the changes in the channel current (I_{DS}) highlight the possibility of representing specific multiple states of electrical conductance. Furthermore, as F_{21}-DDPA possesses the dielectric property,[84], [85] the reduction in the leakage current to the gate can be observed, as shown in Figure 2.25.

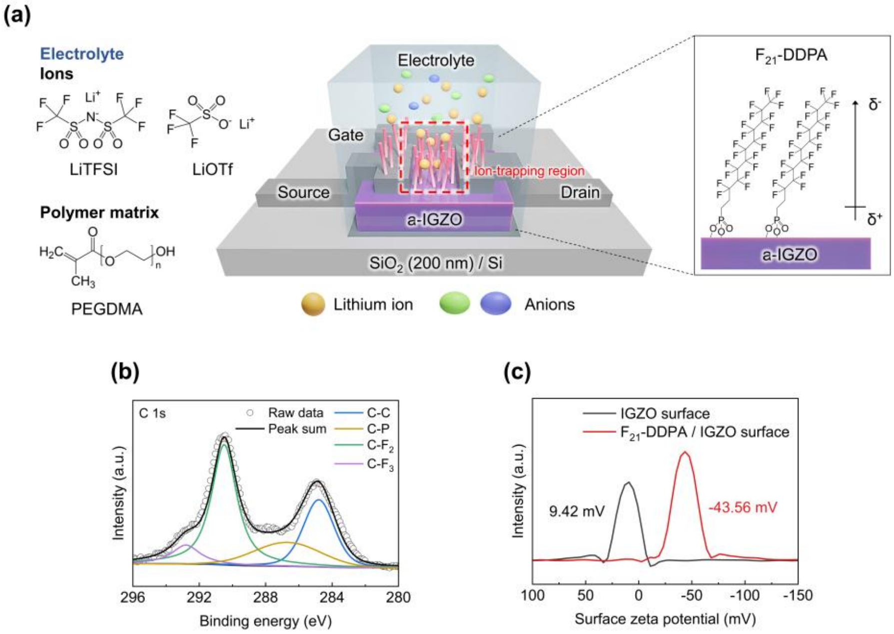

Figure 2.20. (a) Schematic illustration of FLEGT and components of its device. (b) C 1s XPS spectrum of F$_{21}$-DDPA layer. (c) Measured surface zeta potential of each modified surface at pH = 7.

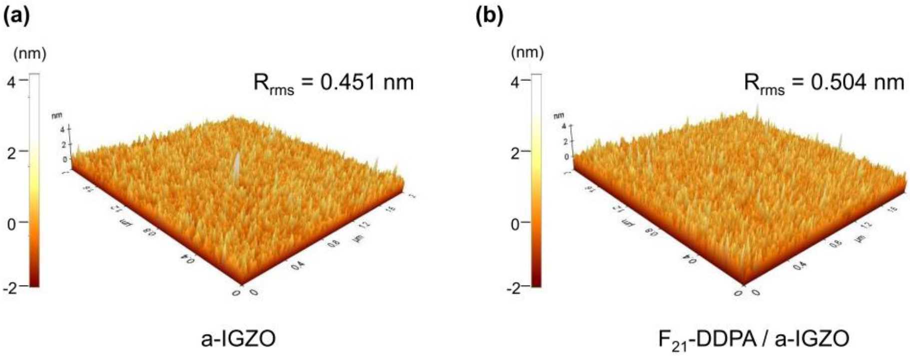

Figure 2.21. Measured surface morphology profile of (a) a-IGZO and (b) F$_{21}$-DDPA-modified a-IGZO by atomic force microscopy (AFM) measurement.

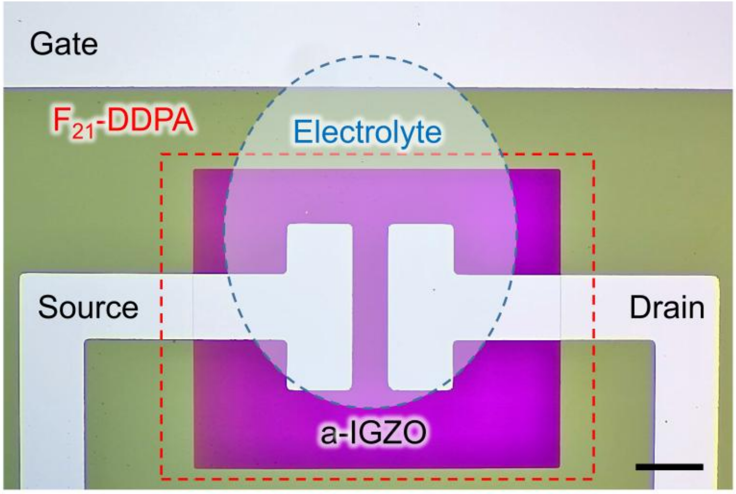

Figure 2.22. Optical image of FLEGT. Scale bar: 100 μm.

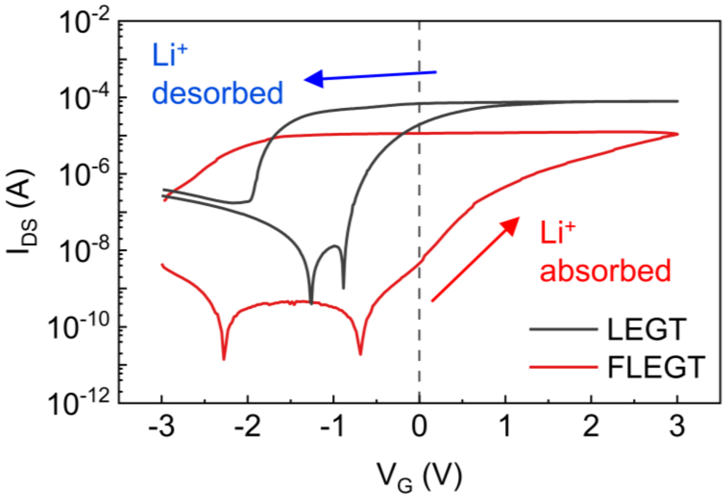

Figure 2.23. Transfer curves for EGTs with each modified surface at fixed gate bias (V_G) scan rate of a 0.8 V s^{-1} (V_{DS} = 0.1 V).

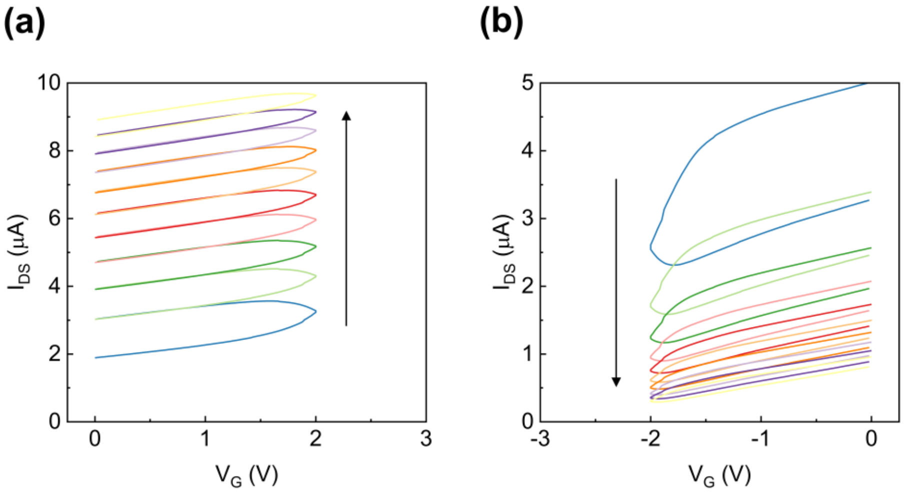

Figure 2.24. Transfer curves by applying 10 consecutive V_G biases. (a) positive bias. (b) negative bias. (V_{DS} = 0.1 V, scan rate: 0.8 V s^{-1})

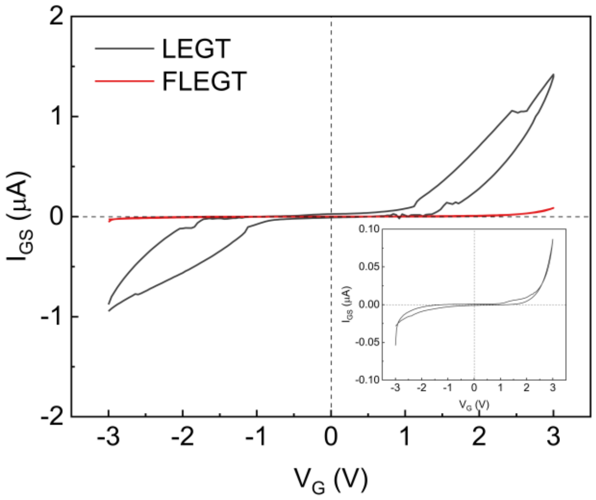

Figure 2.25. Measured leakage current (I_{GS}) through the electrolyte. (V_{DS} = 0.1 V, scan rate: 0.8 V s^{-1}) The inset figure shows a leakage current in FLEGT.

2.3.3. Analysis of electrical characteristics in FLEGT

Figure 2.26a,b shows the I_{DS} responses of LEGT and FLEGT driven by a single square V_G pulse of 1-3 V with a pulse width (t_w) of 10 ms. Here, three major changes can be found in the I_{DS} responses. Firstly, FLEGT maintained the I_{DS} value in a specific nonvolatile state after applying a single V_G pulse. In contrast, the I_{DS} response of LEGT rapidly returned to its initial state after applying a single V_G pulse. Secondly, in FLEGT, a notable reduction in the transient time for dissipating I_{DS}, which is indicative of the second-level write-read delay, can be observed when compared to LEGT.[86] Here, the write-read delay is defined as the time difference at which the rate of change in current over time becomes zero after the application of the V_G Pulse. After applying a single V_G pulse, lithium ions which have the gating effect at the interface are dissipated back into the electrolyte to maintain charge equilibrium in the electrolyte. This can be inferred from the I_{DS} behavior. The transient response of I_{DS} is represented as a second-level write-read delay, and the I_{DS} response controlled by ions is expressed as follows,[87]

$$I_{DS} = (I_0 - I_\infty)\exp\left[-\left(\frac{t-I_{DS}}{\tau_r}\right)^{\beta}\right] + I_\infty, \qquad (2.8)$$

where I_0 is the peak value of I_{DS}, I_∞ is the value of I_{DS} at the infinite point, β is the stretch index ranging between 0 and 1, and τ_r is the length of the retention time. However, since the I_{DS} response was measured with a resolution of 1 ms, it was difficult to accurately calculate the write-read delay in the transient response of each device. Therefore, the write-read delay of I_{DS} after the peak by taking the derivative of I_{DS} in terms of time as follows,[86]

$$\frac{\partial I_{DS}}{\partial t} \text{ and } \frac{\partial^2 I_{DS}}{\partial t^2} = 0 \qquad (2.9)$$

Write-read delay can be defined as when the change in I_{DS} over time is 0. the write-read delay is defined as the time corresponding to each derivative value equivalent to 1% of the peak value of I_{DS}. As shown in Figure. 2.26a,b, the LEGT has a write-read delay of approximately 140 ms and the FLEGT has a write-read delay of 40 ms, under applied a single V_G pulse of 10 ms. Therefore, comparing the two devices, introducing F_{21}-DDPA effectively reduced the write-read delay. This can be understood as the amount of lithium ions diffused back to the electrolyte reduced due to a charge interaction between F_{21}-DDPA and lithium ions. Furthermore, the write-read delay hardly changes depending on the amplitude of the applied V_G pulse.

Finally, due to the increased thickness of EDL by F_{21}-DDPA, FLEGT demonstrated a reduced overall I_{DS} value compared to LEGT, which lowers energy consumption for switching per pulse (Figure 2.26c). These facts are crucial for realizing energy-efficient neuromorphic computing and suggest that FLEGT successfully demonstrated synaptic characteristics. Furthermore, the I_{DS} states were capable of being switched to specific I_{DS} values with the retention lasting over 30 min and slight decay (Figure 2.26d,e). The presented nonvolatility is sufficient to ensure the requirements of application in analog deep learning and training, because inference process does not necessitate memorizing correct data with perfect form during the process, but rather finds generalized features within the input data.[88] Overall, these differences in I_{DS} response are attributed to the introduction of F_{21}-DDPA, demonstrating improvement in multimodal behavior.

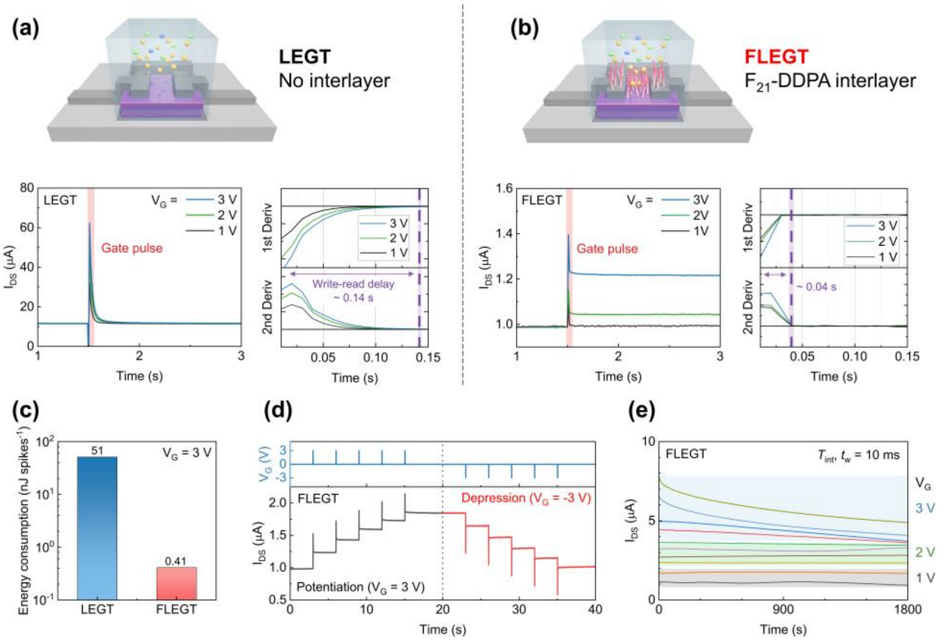

Figure 2.26. (a,b) Current responses by a single V_G pulse with amplitudes varying from 1 V to 3 V (t_w= 10 ms, V_{DS} = 0.1 V) in (a) LEGT and (b) FLEGT. The figures located to the right of the current response depict the decay behavior following the application of a single pulse, revealing differences in the write-read delay. The purple dashed line indicates the write-read delay. (c) Energy consumption per spike in each EGT. The energy consumption is calculated by $V_{DS} \times I_{DS} \times t_w$. (d) Potentiation and depression process with 5 consecutive V_G pulses (t_w = 10 ms, T_{int} = 5 s). (e) Retention characteristics of the 10 states. Each state is switched by randomly applying consecutive V_G pulses with varying pulse numbers (#) of 10-200 and amplitudes of 1-3 V. Pulse width (t_w) and interval (T_{int}) are fixed at 10 ms.

Figure 2.27 demonstrates the conductance updates in FLEGT as a response to varying parameters of V_G inputs. I examined the pulse number (#), voltage amplitude, t_w, and pulse interval (T_{int}) as V_G input variables, given that these parameters fundamentally relate to energy consumption and recognition accuracy during conducting inference tasks in artificial neural networks.[89] Figure 2.27a-c shows the conductance update corresponding to each input parameter, and Figure 2.27d-f presents the extracted output parameters, including nonlinearity (NL) in each long-term potentiation (LTP)/long-term depression (LTD) side (NL_P/NL_D) and dynamic range (G_{max}/G_{min}). Here, the conductance updates on each LTP/LTD side are fitted by[90]

$$G_{LTP} = \mathrm{B}\left(1 - \exp\left(-\frac{P}{A_P}\right)\right) + G_{min}, \quad (2.10)$$

$$G_{LTD} = \mathrm{B}\left(1 - \exp\left(\frac{P-P_{max}}{A_D}\right)\right) + G_{max}, \quad (2.11)$$

$$\mathrm{B} = \frac{G_{max}-G_{min}}{1-\exp\left(\frac{-P_{max}}{A}\right)}, \quad (2.12)$$

where G_{LTP} and G_{LTD} are the conductance state of each potentiation and depression side, respectively, P_{max} is the maximum number of gate pulses, and A_P and A_D are the nonlinear parameter for conductance update of potentiation and depression, respectively. Using A_P and A_D, NL corresponding to A_P and A_D can be obtained. For the ideal device, NL is 0, meaning that the device demonstrates linear conductance update.

Dynamic range is calculated by

$$Dynamic\ range = \frac{G_{max}}{G_{min}}, \quad (2.13)$$

where G_{max} is the maximum conductance and G_{min} is the minimum conductance during conductance updates.

The value of NL nears 0 as the conductance updates approach a perfect linearity. For the V_G input of the amplitudes of ±3 V, # of 256, t_w/T_{int} of 10 ms, FLEGT successfully achieved conductance updates with NL_P of 1.04, NL_D of 1.54, and dynamic range of 10.42. This result suggests that compared to LEGT, FLEGT was capable of demonstrating higher linearity and a larger dynamic range, as the conductance updates in LEGT are shown in Figure 2.27g and 2.28. The origin of differences in conductance updates is due to the electrostatic interaction between lithium ions and F_{21}-DDPA at the channel/electrolyte interface.[91] This included not only the trapping of ion movement at the interface but also an increment in the thickness of the EDL, providing a gating effect at the interface. Theoretically, the major gating effect on the channel induced by EDL is confined to the stern layer formed by charged ions at the interface. Since the formation of the stern layer is close to a monolayer, it can be easily saturated by continuously applied V_G pulses.[92], [93] Therefore, the thickness of the stern layer increases due to F_{21}-DDPA at the interface, and lithium ions were likely to be hardly saturated by an external electric field. This hypodissertation is supported by the values of each NL in conductance updates. As shown in Figure 2.27d-f, NL decreased as the values of input parameters–including the pulse number (#), amplitude, t_w/T_{int}– also decreased. Meanwhile, as the amplitude and t_w/T_{int} of the V_G pulse applied to the electrolyte decrease, the dynamic range is also greatly reduced. Nevertheless, FLEGT demonstrated overall conductance updates with high linearity (<1 for NL_P, <1.5 for NL_D) as lithium ions were sequentially saturated at the interface.

Figure 2.27h shows the cycle-to-cycle variation during conductance updates for

100 cycles with V_G amplitudes of ± 3 V, # of 256, and t_w/T_{int} of 10 ms. Overall, a substantial deviation in the NL cannot be observed throughout 100 cycles, except for a decrease in the dynamic range. Nevertheless, a slight degradation was observed in the dynamic range, which seems to be attributed to initial charging/discharging process by lithium ions during the initial operation. Additionally, to examine the device-to-device variation of FLEGTs, I confirmed and evaluated the conductance updates for 20 devices, as shown in Figure 2.27i. From the results, a few deviations in the dynamic range and NL can be observed. However, the slight deviations in each parameter suggested that both F_{21}-DDPA and the lithium electrolyte were uniformly well-deposited. The parameter values of G_{max}, G_{min}, NL_P, and NL_D were 94.74±4.64 μS, 0.72±1.00 μS, 1.03±0.07, 1.53±0.08, respectively. Furthermore, substantial performance deviation between devices can be avoided even when a simple fabrication process is employed.

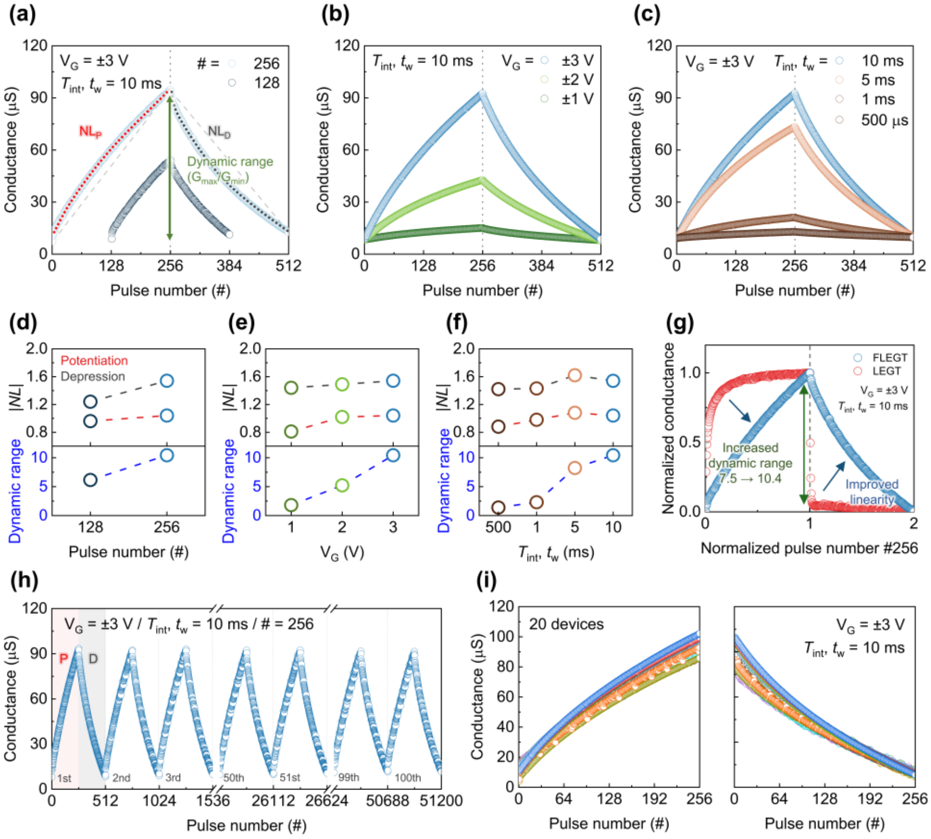

Figure 2.27. (a-f) Conductance updates in FLEGT with varying (a) pulse number of 128 and 256, (b) V_G amplitudes from ±1 V to ±3 V, (c) pulse width and interval from 500 μs to 10 ms, and (d-f) their respective parameters including LTP/LTD nonlinearity and dynamic range. The gray dashed line indicates perfect linearity, corresponding to NL of 0. (g) Comparison conductance update between LEGT and FLEGT. (h) Cycle-to-cycle variation for 100 cycles. The input parameters are described in the figure. (i) Device-to-device variation across 20 devices. The data are collected from the 10th cycle in each device.

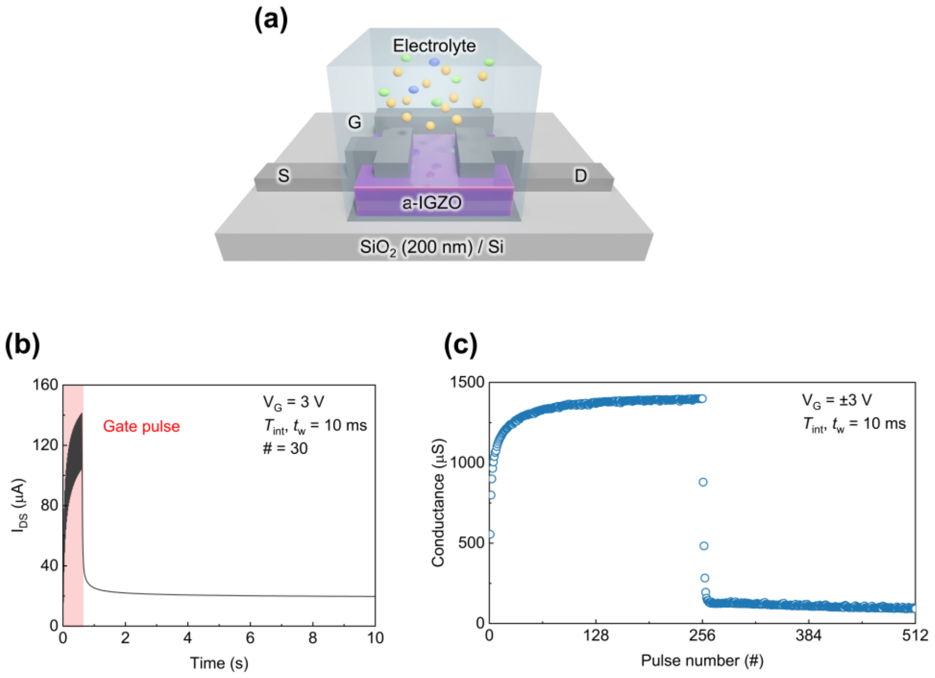

Figure 2.28. (a) Schematic illustration of LEGT. (b) I_{DS} response by 30 consecutive V_G pulses in LEGT. (c) Conductance updates in LEGT with fixed input parameters (V_G = 3 V, # = 256, T_{int}, t_w = 10 ms).

2.3.4 Analysis of ion-dipole force

Schematic illustrations elucidating the working mechanism are depicted in Figure 2.29a,b. I evidenced the presence of differences in electrical properties attributable to the incorporation of F_{21}-DDPA, suggesting robust electrostatic interactions between F_{21}-DDPA and lithium ions. This effect can potentially be hypothesized as the major reason for allowing precise control over the multiple conductance states in FLEGT, facilitated by trapping lithium ions at the interface. Nonetheless, it remained essential to ascertain the type of interactions (physical or chemical reactions) instigated by F_{21}-DDPA among lithium ions at the interface and identify specific binding sites within F_{21}-DDPA where lithium ions are majorly trapped. I investigated the charge interactions between F_{21}-DDPA and adsorbed lithium ions via density functional theory (DFT) calculations.[94] Additionally, I endeavored to elucidate the underlying principles by comparing energy differences upon adsorption of the lithium ion on the IGZO surface. I focused on changes in self-consistent field (scf) energy difference (ΔE) and the charge density (Δρ) for each structure. ΔE and Δρ were calculated as follows,

$$\Delta \mathrm{E} = -\{E_{DDPA+Li} - (E_{DDPA} + E_{Li})\} \qquad (2.14)$$

$$\Delta \rho = \rho_{DDPA+Li} - (\rho_{DDPA} + \rho_{Li}) \qquad (2.15)$$

where $E_{DDPA+Li}$, E_{DDPA}, and E_{Li} are the optimized energies of each structure, and $\rho_{DDPA+Li}$, ρ_{DDPA}, and ρ_{Li} are the charge density of each structure, respectively.

First-principle calculations were performed using Quantum Espresso V7.1 within the density functional theory (DFT) calculation, incorporating the pseudopotential of each atom through projector augmented wave (PAW).[94] The exchange-correlation functional was handled using the generalized gradient approximation (GGA), following the parametrization scheme of Perdew, Burke, and Ernzerhof (PBE). In the process of converging scf energy, calculations within the crystal were conducted using k-points of 36, and a convergence threshold was set at 2×10^{-7} Ry (about 2.721×10^{-6} eV). Here, to describe the physisorption on the surface by lithium, I incorporated the Grimme-D3 van der Waals correction during the scf energy conversion process. The charge density plot derived from these energy calculations represents the changes in electron charge density. The distribution of electron density across the x, y, and z axes was visualized through a 3D plot.

The crystal structures used for calculations were selected to be of a simple structure, considering the computational cost. The crystal structure of F_{21}-DDPA was utilized in its energetically stable linear conformation, not in helical form. Indeed, the external electric field, which influences the movement of the lithium ion, also improves the alignment of F_{21}-DDPA. Therefore, a linear conformation of F_{21}-DDPA is desirable.[95] To examine the binding energy according to the interaction position with lithium ions, DFT calculations were based on the structure containing two linear F_{21}-DDPAs. After optimizing the structure into an energetically stable formation, the distance between the two adjacent F_{21}-DDPAs was measured to be 7.28 Å, based on the each phosphorous. Charge density and energy differences were calculated within a range of 10 Å in the x, y, and z directions, respectively, based on lithium within the crystal structure.

For the IGZO crystal structure, I calculated the interaction with lithium ions implementing a spinel-IGZO as the reference.[2] Although the actual IGZO structure is amorphous, obtaining a stable energy optimization for such amorphous crystals within DFT calculations proves to be an exceptionally intricate process. I investigated, therefore, the adsorption of lithium ions utilizing a crystalline spinel-IGZO structure (Figure 2.29c) and exclusively carried out a comparison of energy and charge density differences (ΔE, Δρ) depending on the presence of F_{21}-DDPA. Additionally, for the deposition of F_{21}-DDPA in the experimental process, I performed UVO treatment on IGZO. During this treatment, oxygens near the surface of the IGZO crystal were eliminated, resulting in a large amount of oxygen vacancies on the surface. Considering this point, oxygen from the IGZO surface was removed, followed by the energetic stabilization of the crystal. Subsequently, I calculated the adsorption energy of a lithium ion on the surface of IGZO.

The position of lithium between F_{21}-DDPAs cannot be determined during calculation. This is attributed to the fact that the electron lone pair of fluorine does not contribute to the coordinate bond, instead, it participates in ion-dipole interactions with lithium. Therefore, by positioning lithium at the center of each fluorine in F_{21}-DDPA, I calculated the energy and charge density at the most stable structure. For lithium located in the van der Waals (vdW) gap, the distance to the interacting fluorine impacts the calculation results of the ΔE value.

In the calculation of lithium adsorption energy on the surface of IGZO, due to the utilization of the spinel-IGZO structure, adsorption energy was calculated for the random location of lithium ion on the (111) crystal plane. Herein, although the surface energy of IGZO does contribute to the absorption energy, the species of cation interacting upon lithium adsorption exerts a more substantial influence. Given that the structure of the channel material employed in actual experiments, however, is amorphous IGZO, the adsorption energy of lithium should be regarded as an average energy value. I performed calculations on a lithium adsorption surface, using the IGZO (111) plane as a reference. This is due to the (111) plane possessing the highest surface energy than the (100) and (110) planes.[96]

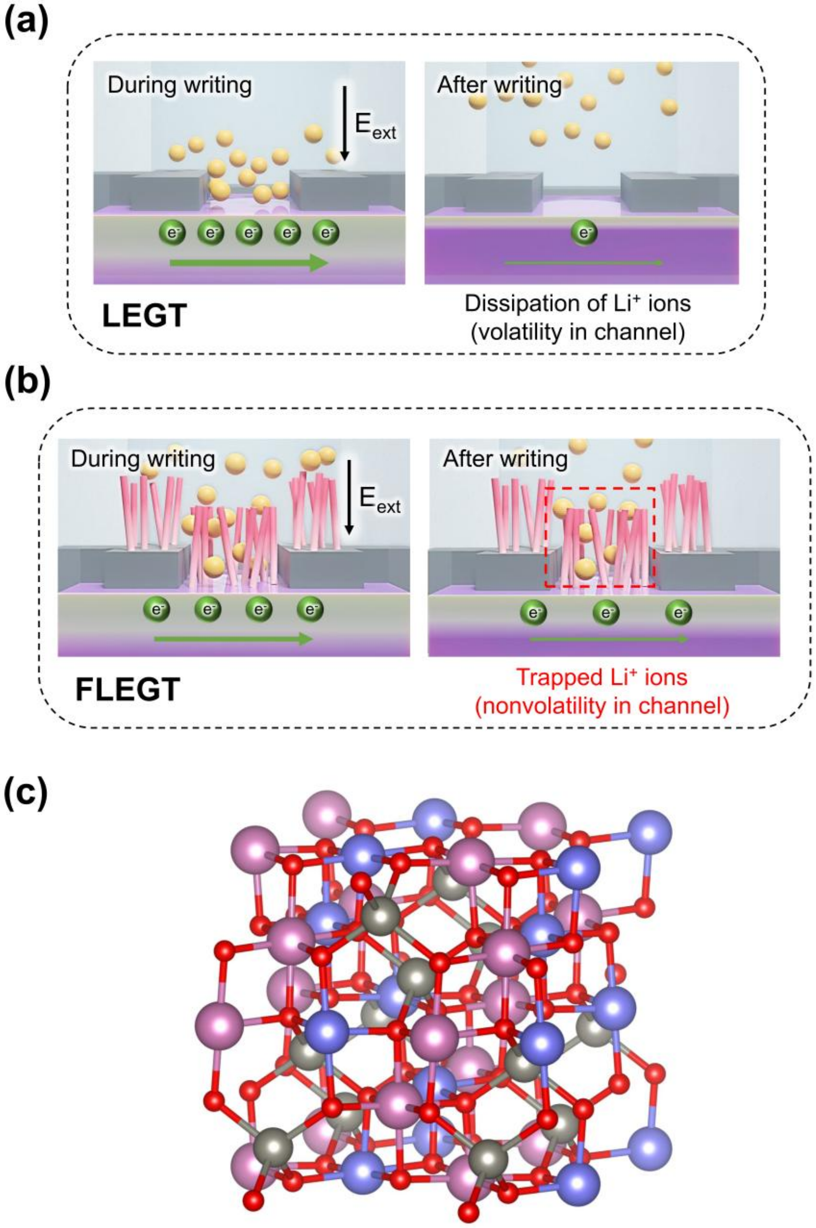

Figure 2.29. (a, b) Schematic illustration of working mechanisms in (a) LEGT and (b) FLEGT. (c) Crystal structure of spinel-IGZO for DFT calculation. pink: indium (In), green: gallium (Ga), black: zinc (Zn), red: oxygen (O).[2]

A schematic image for the coordination number corresponding to the movement of lithium ions driven by an external electric field is presented in Figure 2.30a. Considering that lithium ions migrate through F_{21}-DDPA to approach the surface of IGZO, I calculated the $\Delta\rho$ and ΔE based on the position of lithium between F_{21}-DDPAs. When lithium approaches the fluorine site in a C–F bond, charge accumulation (positive $\Delta\rho$) occurs between lithium and fluorine. Conversely, charge depletion can be found in the C–F bond, which can be explained as a weakening of the C–F binding energy (negative $\Delta\rho$). Therefore, coulombic attraction exists due to the strong ion-dipole force between lithium and the C–F bond (C–F … Li^+). This phenomenon is also applicable when lithium is adsorbed onto or exists between F_{21}-DDPAs. As shown in Figure 2.30b, charge accumulation occurs when lithium ions approach F in F_{21}-DDPA. Conversely, I also observed charge depletion in the C–F bond and inferred that the electron cloud moves in the Li ... F direction. This serves as evidence of the occurrence of the ion-dipole force. Relatively, the positive $\Delta\rho$ induced by lithium ion is most pronounced as follows; (i, ii) lithium ion is absorbed on the $-CF_3$ group < (v, vi) in close to the surface of IGZO < (iii, iv) trapped in van der Waals (vdW) gap. This implies that when lithium ions are driven to F_{21}-DDPAs by an external electric field, they tend to become more confined in the vdW gap between $-CF_2-$ rather than being adsorbed to $-CF_3$. This signifies when lithium ions are positioned within the vdW gap, the overall system achieves its highest energetic stability; in other words, the binding energy between lithium and F_{21}-DDPA is maximized (Figure 2.40c). Herein, the differences in ΔE between the vdW gap result from the variation depending on the distance between adjacent fluorine. Indeed, lithium ions hardly form coordinate bonds with the electron lone pair in fluorine.

The specific binding sites for lithium are, therefore, determined by the ion-dipole force from the C–F bond.[97] Also, as lithium ions approach the surface of IGZO, ΔE becomes smaller. This result is because the influence of the coulombic attraction between F and lithium decreases, and the charge interaction with oxygen (O) and cations (In, Ga, Zn) intensifies. Nevertheless, the fact that ΔE is larger when the lithium ion is trapped in vdW gap (iii, iv) than in close to the surface of IGZO (v, vi) and absorbed to the $-CF_3$ group (i, ii) suggests that lithium ions are likely to be more trapped when they exist between F_{21}-DDPAs. On the other hand, when lithium ion is adsorbed on the surface of IGZO without F_{21}-DDPA, ΔE is smaller than in all cases where lithium ion is adsorbed to F_{21}-DDPA, demonstrating that charge interaction with F_{21}-DDPA is favorable in trapping lithium ions at the interface.

To experimentally verify the changes in Δρ through DFT calculations, the binding energy through XPS measurements is investigated. Here, the change in Δρ was confirmed by the binding energy of fluorocarbons, as the amount of lithium ions trapped in F_{21}-DDPA is quite few. As shown in Figure 2.30e, a peak shift of fluorocarbon in F 1s was observed from 687.56 eV to 687.28 eV. This suggests that the strength of the C–F bond is weakened due to the presence of lithium ions between F_{21}-DDPA, which in turn implies that a coulombic attraction has occurred between the lithium ions and fluorine.[86], [98] Additionally, the absence of a peak corresponding to the Li–F bond (~685.0 eV) in F 1s implies that the effect of chemical reactions by electrical potential was minimal in F_{21}-DDPA.[98], [99] The finding from the XPS data corroborates that the experimentally investigated charge interaction between lithium ions and F_{21}-DDPA, as confirmed through DFT calculations, is in alignment with the experimental result.

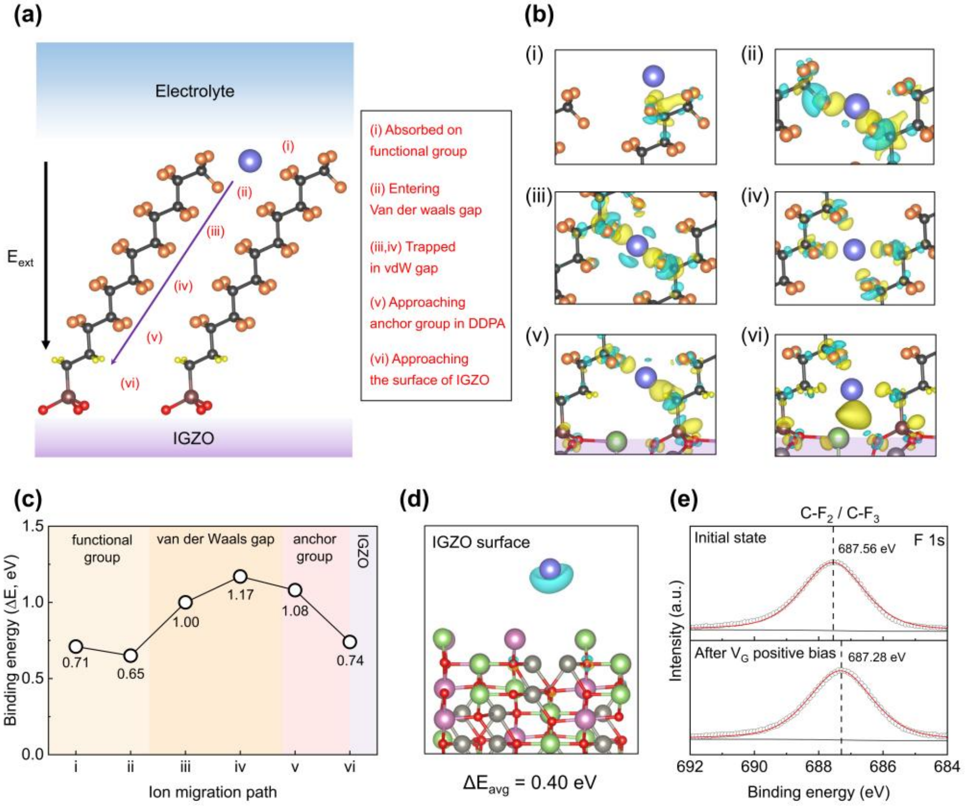

Figure 2.30. (a) Schematic image of each lithium migration path for calculating binding energy (ΔE) derived from density functional theory (DFT) calculation. (b) Differential charge density (Δρ) associated with each migration path of lithium in F_{21}-DDPAs. purple: lithium (Li), black: carbon (C), orange: fluorine (F), brown: phosphorus (P), yellow: hydrogen (H), red: oxygen (O), green: zinc (Zn), pink: indium (In), gray: gallium (Ga), purple background: IGZO region. Yellow and blue graphics indicate charge accumulation and depletion, respectively. isosurface: 0.002 e $Å^{-3}$. The surface of crystalline spinel-IGZO is (111) for simplifying DFT calculation.[2] (c) Calculated ΔE according to lithium migration path. (d) Differential Δρ associated with the absorption of lithium on the surface of IGZO. isosurface: 0.001 e $Å^{-3}$. (e) XPS spectra of F 1s in the initial state and the state after applying positive bias for 30 s of F_{21}-DDPA.

So far, I carried out investigations on the physisorption of lithium ions through the introduction of F_{21}-DDPA. The thickness of the stern layer in EDL is formed by lithium ions at the interface, and the formation of EDL is maintained, thereby demonstrating a long-term conductance state. To verify whether electrochemical doping of lithium ions occurs in a-IGZO, I investigated an electrochemical impedance spectroscopy (EIS) measurement to investigate whether an electrochemical reaction occurred with lithium ions in a-IGZO. Here, determining whether the reaction occurs at the channel/electrolyte interface is crucial. I constructed, therefore, a two-terminal device as a MIM structure, ITO(+)/Electrolyte/F_{21}-DDPA/a-IGZO/ITO(-), to verify electrochemical reactions. I examined the changes in capacitance and impedance with respect to frequency to understand how the introduction of F_{21}-DDPA influenced the behavior of lithium ions. I applied an AC bias of 25 mV to ITO(+) from 0.1 Hz to 10^6 Hz.

The impedance (Z) with respect to frequency has the following relationship with the capacitance (C),[12], [100]

$$\frac{d\log|Z|}{d\log f} \sim -S\frac{d\log C}{d\log f} + A \qquad (2.16)$$

where S and A are constant. Through the changes corresponding to the value of $\frac{d\log|Z|}{d\log f}$, I can infer how the ion-induced effects are occurring at the interface.

As shown in Figure 2.31a,b, the changes in capacitance and impedance with respect to frequency can be divided into four regions; (i) bulk capacitance, (ii) charging of EDL, (iii) EDL capacitance, and (iv) pesudocapacitance. In region i, due to the high frequency of the AC bias, it is difficult for ions to exhibit a gating effect, thereby only the bulk capacitance of the electrolyte has an influence. Since the bulk capacitance does not change with changes in frequency, the value of $\frac{d\log|Z|}{d\log f}$ is shown to be close to 0. In region ii, as the applied AC frequency decreases, the gating effect of the EDL formed at the interface increases, thus, the value of $\frac{d\log|Z|}{d\log f}$ slightly increases. In region iii, as the ions influencing the formation of the EDL at the interface saturate, the increase in capacitance decreases with lower frequency, which is manifested as an increase in the internal impedance. Consequently, the slope value of $\frac{d\log|Z|}{d\log f}$ increases. In region iv, where I inspected the effects occurring at the interface, it is observed that the slope of $\frac{d\log|Z|}{d\log f}$ is similar to that in region iv. This can be interpreted as an influence of the EDL formation, with minimal electrochemical reaction between lithium ions and a-IGZO at the interface. Hence, based on the data, regardless of the presence of F_{21}-DDPA, an electrochemical reaction is inhibited between lithium ions and a-IGZO. Rather, Figure 2.31c suggests that the introduction of F_{21}-DDPA effectively suppresses the electrochemical reaction. I divided the impedance according to frequency into imaginary and real parts, and by applying these to the equivalent circuit, I differentiated into three resistance components: bulk resistance (R_b), charge transfer resistance (R_{ct}), and Warburg impedance. Here, due to the complexity of analyzing the Warburg impedance in the current device structure, I limit our investigation to the other resistance components. Regardless of the presence of F_{21}-DDPA, R_b exhibits a value of approximately 1 kiloohms, whereas R_{ct} increases from about 1.3 kiloohms to 2.2 kiloohms upon the introduction of F_{21}-DDPA. This implies that F_{21}-DDPA further suppresses the charge transfer occurring at the interface, indicating the changes in conductance in FLEGT are not due to electrochemical doping but controlled by the formation of EDL. Such analysis of interfacial reactions through EIS measurements provides evidence for our claims.

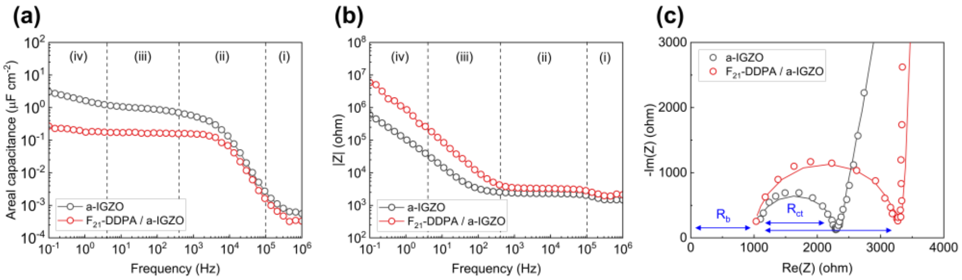

Figure 2.31. (a) Areal capacitance and (b) impedance as a function of applied AC voltage frequency. (c) Nyquist plot of the MIM structures.

Finally, the electrical characteristics of the ionic liquid ($[\mathrm{EMIM}]^+[\mathrm{TFSI}]^-$)-gated a-IGZO EGT with F_{21}-DDPA is investigated to confirm the dependency on ion size in the ion-trapping effect. Here, the ionic radius of lithium is 90 pm, and the dimensions of $[\mathrm{EMIM}]^+$ are characterized by a major axis of approximately 800 pm and a minor axis measuring around 500 pm. As shown in Figure 2.32, a noticeable hysteresis window was hardly observed in the double-swept transfer curve when an ionic liquid was employed as the gating electrolyte. Furthermore, upon application of V_G pulses of 1-3 V, not only does the I_{DS} response exhibit negligible presence of retention states, but poor linearity was found during conductance updates. Consequently, these findings suggest that the ability of F_{21}-DDPA to trap cations is not merely a result of charge interactions with cations.

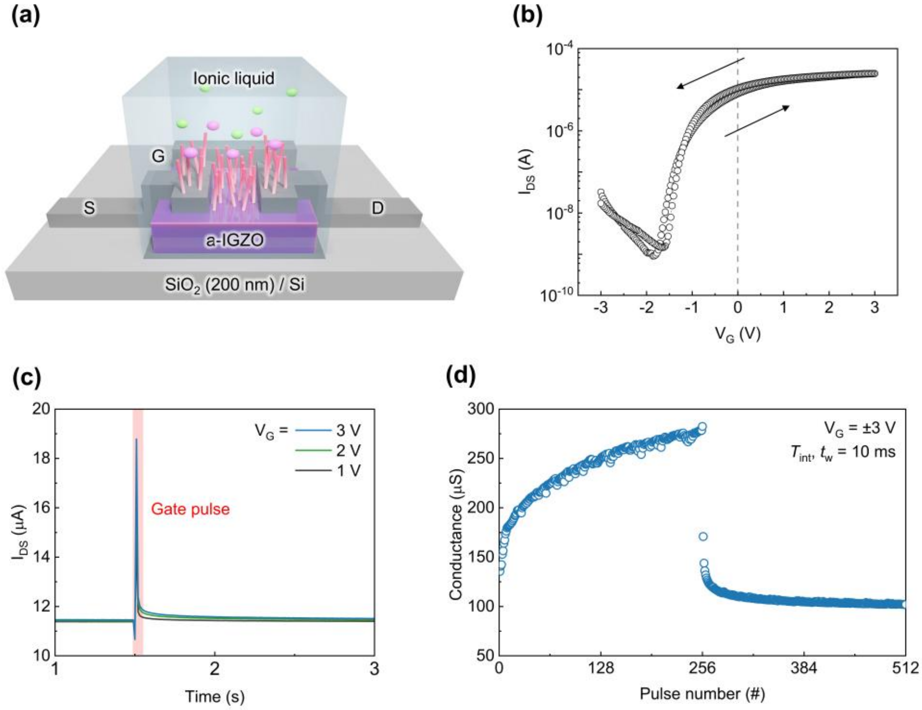

Figure 2.32. (a) Schematic illustration of the ionic liquid ($[EMIM]^+[TFSI]^-$)-gated a-IGZO transistor with F_{21}-DDPA interlayer. (b) Transfer curve for the ionic liquid-gated a-IGZO transistor at a fixed scan rate of 0.8 V s^{-1} (V_{DS} = 0.1 V). (c) Current responses by a single gate pulse with amplitudes varying from 1 V to 3 V (t_w= 10 ms, V_{DS} = 0.1 V). (d) Conductance updates in LEGT with fixed input parameters (V_G = 3 V, # = 256, T_{int}, t_w = 10 ms).

2.3.5. Inference tasks for device performance using CNN

To verify the applicability of the enhanced synaptic characteristics of FLEGT, I carried out training and inference tasks based on the CIFAR-10 dataset using convolutional neural network (CNN). I utilized an open-source platform 'DNN+NeuroSim V2.1,' an integrated framework to benchmark neuromorphic accelerators for deep neural networks.[101] Here, the experimentally obtained NL, dynamic range, cycle-to-cycle variations, device-to-device variations, input voltage, and pulse width/interval were used as the characteristics of the resistor that modulate synaptic weight in carrying out inference tasks. As shown in Figure 2.33a, the CIFAR-10 dataset as input data consists of a 32 × 32-pixel size and each image has 3 colors (red, green, blue). The dataset contains 10 categories, such as dog, airplane, cat, ship, etc, and consists of 50,000 training and 10,000 inference/testing images. I set the CNN size which contains 6 convolution layers (1-6), 3 pooling layers (2, 4, 6), and fully connected layers (7, 8). The feature extraction is conducted in convolution and pooling layers, and the image recognition and classification are conducted in fully connected layers. Each neuron in the fully connected layers (input, hidden, output layers) is connected through synapses, where the synaptic characteristics of FLEGT obtained experimentally are utilized to modulate the synaptic weight.[101], [102]

After conducting training tasks with 50,000 images, the inference accuracy based on the synaptic characteristics of FLEGT obtained experimentally was found to be 85.87% when conducting 10,000 inference tasks, as shown in Figure 2.33b,c. The accuracy of FLEGT, while not reaching the 91.77% obtained in the ideal case (NL and variations are 0), still demonstrated a respectable performance of FLEGT.

This high inference accuracy can be attributed to the high linearity and sufficient dynamic range inherent to FLEGT, in conjunction with its low cycle-to-cycle and device-to-device variations. Given that inference accuracy is influenced by the values of parameters during conductance updates, it is established that FLEGT exhibits advantageous synaptic characteristics.

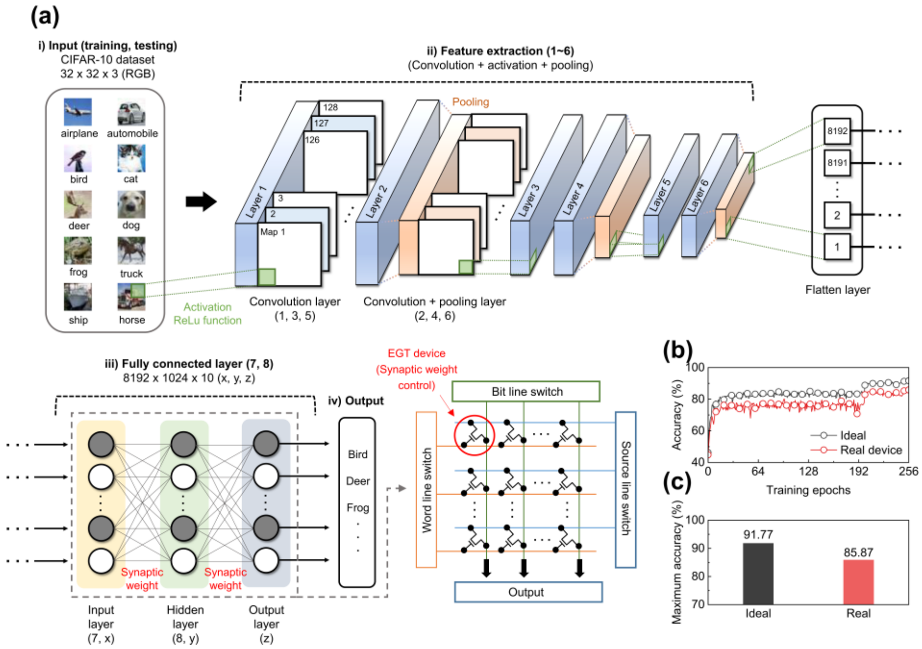

Figure 2.33. (a) The configuration of each layer in CNN and process steps for training and testing tasks of input data. The input data is derived from the CIFAR-10 dataset, which consists of 10 classes of images, each sized 32 x 32 pixels and featuring 3 colors (red, green, blue). The gray dashed line indicates a schematic illustration of the artificial neural network composed of the EGT devices in a crossbar circuit, corresponding to the fully connected layer (7, 8). (b) Inference accuracy and (c) maximum accuracy during training and classification tasks for both an ideal device (gray) and an experimental device (red). An ideal device is defined by a nonlinearity of 0, and a deviation value of the device being 0 %.

2.3.6. Experimental method

Materials**:** B-doped p^{++} Si wafers with 200 nm-thick thermally grown SiO_2 were used as the device substrate. Lithium trifluoromethanesulfonate (LiOTf, 99.995 % purity), Poly(ethylene glycol) dimethacrylate (PEGDMA, Mw ~ 550) and 2-hydroxy-2-methylpropiophenone (HOMPP, 97 % purity), Heneicosafluorododecylphosphonic acid (F_{21}-DDPA, > 97 % purity), and 1-Ethyl-3-methylimidazolium bis(trifluoromethylsulfonyl)imide (EMIM-TFSI, > 97 % purity) were purchased from Sigma-Aldrich. Lithium bis(trifluoromethanesulfonyl)imide (LiTFSI, > 98 % purity) was purchased from TCI Chemicals.

Preparation of lithium electrolytes**:** 21 M LiTFSI and 7 M LiOTf were dissolved in deionized (DI) water, followed by the addition of PEGDMA at a weight ratio of 1:1 with the solution. To facilitate UV curing and solidification, HMOPP was added into the mixture at a 2 wt%. The prepared electrolyte was then stirred vigorously for 3 hr. After that, the prepared electrolyte was stored in a refrigerator at 4 °C.

Fabrication of FLEGTs**:** The SiO_2/Si substrate was carried out in a cleaning process, including sequential ultrasonication in detergent for 15 min, rinsing in DI water for 15 min, ultrasonication in acetone, and isopropanol for 15 min each. This was followed by UVO treatment (184, 254 nm with an intensity of 100 mW cm^{-2}) for 15 min. Subsequently, the a-IGZO channel layer was deposited onto the cleaned substrate using radio-frequency (RF) magnetron sputtering. The RF sputtering was performed under a flow of Ar gas (25 sccm), with a target power of 90 W applied to the a-IGZO target (In:Ga:Zn:O = 1:1:1:4 at%) under working pressure of 10^{-6} mTorr at a room temperature. The thickness of the sputtered a-IGZO layer was approximately 20 nm. Following deposition, the a-IGZO layer was annealed at 250 °C for 90 s using a rapid thermal annealing (RTA) system. The annealed a-IGZO layer was then patterned using photolithography and wet etching processes to define the channel region. Al source, drain, and side gate electrodes were deposited to achieve a thickness of approximately 100 nm through a thermal evaporation system. The distance between the side gate electrode and the a-IGZO channel measured about 400 μm. The channel width and length were 500 μm and 100 μm, respectively. To deposit F_{21}-DDPA onto the surface of a-IGZO channel, the fabricated device was subjected to UVO treatment for 15 min. A metal mask was used during this process to expose only the channel region. Subsequently, the UVO-treated a-IGZO device was immersed in a glass vessel containing F_{21}-DDPA solution (0.01 mM in toluene) at room temperature for 24 hr. During this deposition process of F_{21}-DDPA, the glass vessel was placed in a sealed Teflon desiccator. Following the deposition of F_{21}-DDPA, the device was rinsed with IPA to remove any residual substances. The prepared lithium electrolyte mixture was applied between the channel and the gate electrode using the drop-casting method. Subsequently, the electrolyte was cured under exposure to a UV lamp at 365 nm (600 mJ cm^{-2}) for 10 s.

***Device characterizations and measurements*:** The roughness of the films was investigated using AFM (XE100, PSIA). During measurement, the surface was examined with a low-noise AFM. Topological AFM images were obtained in tapping mode using a silicon probe with a cantilever spring constant of 42 N m^{-1}. To characterize the surface potential of the films, zeta potential measurements (ELSZ-2000Z, Otsuka Electronics) were performed under a solution of pH 7. The areal capacitance of the lithium electrolyte was measured using electrochemical impedance spectroscopy under an AC voltage bias of 25 mV (Biologic, VSP). The chemical properties of the films, including elemental species, binding states, and distribution of specific elements, were investigated from X-ray photoelectron spectroscopy (XPS) (AXIS SUPRA+, Kratos). All samples were measured under 5 × 10^{-10} torr and excited by a monochromatic Al Kα source (1486.6 eV) with operating 15 kV. The binding energy of XPS spectra was calibrated using a sp^2 C peak at 284.5 eV as a reference. The transfer characteristics and pulse measurements for all devices were characterized by an Agilent 4155B semiconductor analyzer and a Keysight 2902B source/measure unit.

2.4. Conclusion

This section proposed tailoring electrostatic interaction by ions at the interface for the development of high-fidelity EGT-based artificial synapses, thereby signifying its prospective applicability in neuromorphic accelerators. The FLEGTs exhibit remarkable characteristics, including over 30 minutes of conductance retention, exceptional endurance of over 100 cycles, high dynamic range, and near-linear synaptic weight updates. Moreover, these devices demonstrate a high accuracy when carrying out simulations of image recognition and classification based on the MNIST dataset using ANN and CIFAR-10 dataset using CNN. By investigating the chemical analysis and DFT calculation, the ion-dipole force, resulting from the coulombic interaction between the fluorinated self-assembled monolayer and lithium ions, effectively traps the ions in the van der Waals gap among fluoroalkyl chains. Nevertheless, the integration of F-SAM is proven to be highly effective in developing EGTs for high-precision artificial synapses, and considering surface potential is crucial to emulating near-linear tunable conductance updates with long-term retention. These findings establish a scientific design principle in the realm of artificial synapses based on EGTs for high-fidelity neuromorphic computing.

Chapter 3. Ferroelectrically modulated ion dynamics for analog computing

3.1. Introduction

One of the strategies for the development of EGT-based artificial synapses with high fidelity is the introduction of the ion-modulating channel-electrolyte interlayer, such as graphene[103], hexagonal boron nitride[104], aluminum oxide[105], and poly methyl methacrylate[106]. Herein, a poly(vinylidene fluoride-*co*-trifluoroethylene) (PVDF-TrFE) ferroelectric polymer thin-film is introduced into the Li^+ EGT as a channel-electrolyte interlayer (ferroelectric polymer-EGT; FP-EGT). The introduction of ferroelectric material as the interlayer has the merit of increasing the ionic conductivity at the interface and reducing the charge transfer resistance between oxide and electrolyte.[107], [108] Among various ferroelectric materials, PVDF-TrFE has good ferroelectric properties, compatibility with oxide semiconductors, availability of thin-film fabrication, low chemical activity with Li^+ ions, and high mechanical durability.[109]–[111] I emphasize the availability of Li^+ FP-EGTs with enhanced synaptic functions and the introduction of PVDF-TrFE interlayer has the following advantages: i) Due to the ferroelectric polarization, PVDF-TrFE thin-film is less likely to interfere with the transport of Li^+ ions, but effectively encourages Li^+ ion hopping along the fluorine (F) sites in PVDF-TrFE. ii) PVDF-TrFE interlayer prevents abrupt changes in ion transport at the interface, rather than allowing gradual Li^+ penetration from the electrolyte to the oxide channel because of the partial polarization switching of domains by the applied gate pulses. iii) Once the Li^+ ions are doped into the oxide channel by the positive gate bias, the self-discharge of Li^+ ions is suppressed by the downward polarized ferroelectric domains. To investigate the role of PVDF-TrFE, zinc oxide (ZnO) is used as an oxide channel, which has good electrochemical activity with Li^+, and Li^+ water-in-bisalt/polymer electrolyte as the gate insulator where the electrolyte features a higher ionic conductivity and areal capacitance.[112] Consequently, the LTP characteristic is clearly observed and due to enabling the sequential transport of Li^+ ions at the interface, conductance update with a dynamic range ($G_{\mathrm{max}}/G_{\mathrm{min}}$) of 92.42 and high linearity is achieved in Li^+ EGT. The ferroelectric polymer-integration method provides new material integration and a perspective on the development of EGT-based artificial synapses for application to practical neuromorphic computing.

3.2. Device configuration

Figure 3.1a shows a structural illustration of Li^+ EGT with PVDF-TrFE interlayer (Li^+ FP-EGT). The channel layer is solution-processed zinc oxide (ZnO) with a surface roughness (R_{rms}) of 0.75 nm, and top-contacted aluminum (Al) is used as the electrode of the source and drain. Li^+ electrolyte is implemented as a gate insulator and Li^+ ions control the electrical conductance (i.e., synaptic weight) of ZnO. Here, Li^+ ions mimic the role of neurotransmitters in the biological synapse.[27] PVDF-TrFE ferroelectric polymer is introduced between the channel and the electrolyte, which can potentially modulate the movement of Li^+ ions at the interface. PVDF-TrFE is spin-coated on the channel and Al electrode, and its thickness is about 18.06 nm. PVDF-TrFE copolymer consists of vinylidene fluoride (CF_2–CF_2) and trifluoroethylene (CF_2–CHF) with alkyl backbone chains. The ferroelectricity of PVDF-TrFE originates from the large difference in electronegativity between –CH_2

(δ^+) and –CF_2 (δ^-), and its unit cells form ferroelectric domains and they exhibit switchable permanent polarization by an external electric field. Here, most importantly, the annealing temperature of PVDF-TrFE is a critical parameter in the formation of crystalline β-phase (all-trans conformation), which exhibits the highest ferroelectricity. In the β-phase, a large spontaneous polarization is exhibited parallel to the C–F dipole moment, and perpendicular to the alkyl backbone chains.[113] When PVDF-TrFE is annealed between Curie and melting temperatures, PVDF-TrFE exhibits a thermodynamically stable β-phase.[114] To obtain the high crystalline β-phase, PVDF-TrFE is annealed at a temperature of 135 °C. We confirm the β-phase of PVDF-TrFE by X-ray Diffraction (XRD) spectrum in Figure 3.1b. The spectrum shows a distinct diffraction peak at $2\theta = 19.8°$, which is the peak of β-phase and indicates the (110) and (200) direction of the crystal plane. The capacitance-electric field hysteresis is shown in Figure 3.1c, which also indicates that PVDF-TrFE is successfully formed in the β-phase with a coercive field of 0.35 MV cm^{-1}. This hysteresis originates from remnant polarization of ferroelectric domains by an electric field, so hysteresis in capacitance depends on the crystallinity of β-phase and the size of ferroelectric domains.

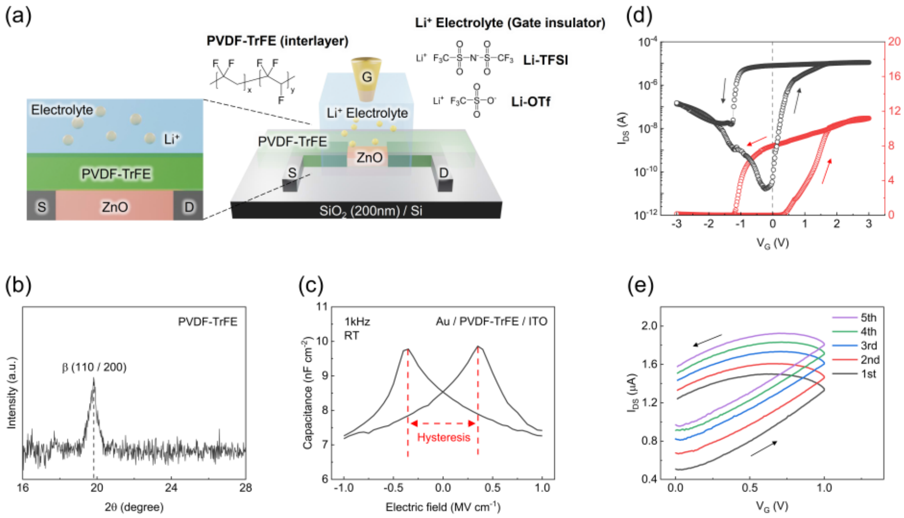

Figure 3.1. (a) Schematic illustration of 3-terminal Li^+ FP-EGT. Al is used as the electrode for the source and drain, and the Au probe tip is used as an electrode for the gate. (b) XRD spectrum of PVDF-TrFE thin film annealed at 135 °C. (c) Capacitance-electric field analysis of PVDF-TrFE capacitors with a structure of metal-ferroelectric-metal (MFM) at an AC voltage frequency of 1 kHz and a double sweep of an electric field from -1 MV cm^{-1} to 1 MV cm^{-1}. (d) Transfer curve for Li^+ FP-EGT at a 0.8 V s^{-1} fixed scan rate (V_{DS} = 0.1 V). (e) Changes in I_{DS} during 5 consecutive V_G double sweeps (0 V → 1 V → 0 V).

When PVDF-TrFE is annealed below the Curie temperature or above melting temperature, the non-polar phase is mainly formed, showing weak ferroelectric characteristics.[114] Surface morphologies of PVDF-TrFE with varying annealing temperatures are also confirmed by atomic force microscopy (AFM) measurement, as shown in Figure 3.2. All profiles show pores or pinholes in PVDF-TrFE thin film, and their sizes become larger as the annealing temperature increases. The surface morphology of aligned PVDF-TrFE is shown when the annealing temperature is above 135 ℃, meaning aligned high crystallinity of β-phase. In the case of an annealing temperature of 185 ℃ which is above the melting temperature of PVDF-TrFE, the crystal structure of PVDF-TrFE shows α- and γ-phase, which have non-polar characteristics.[114]

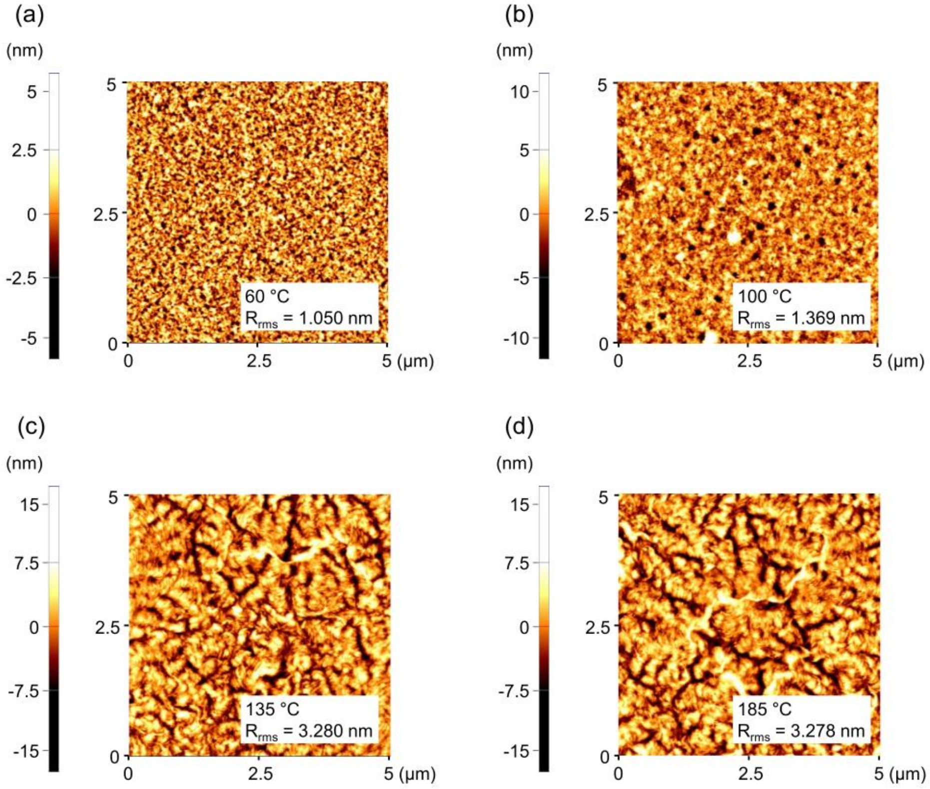

Figure 3.2. Surface morphology profiles of PVDF-TrFE annealed at (a) 60 ℃, (b) 100 ℃, (c) 135 ℃, and (d) 185 ℃ by AFM measurement.

Figure 3.1d shows the transfer curve of Li^+ FP-EGT when the gate voltage is double-swept from -3 V to 3 V with the scan rate of 0.8 V s^{-1}. Here, the hysteresis is found in the transfer curve with an on/off ratio of 10^5 at V_G = 0 V, indicating a memristive behavior of the channel conductance. This effect is crucial for emulating synaptic characteristics, including LTP and conductance update with a large dynamic range. As shown in Figure 3.1e, gradually increasing I_{DS} by consecutive V_G double sweeps also presents the potential of demonstrating multi-level conductance states. Meanwhile, the hysteresis window in the transfer curve is affected by the crystallinity of the β-phase of PVDF-TrFE, as shown in Figure 3.3. The on/off ratio at V_G = 0 V is the largest at an annealing temperature of 135 °C. From investigating electrical characteristics, it is expected that, therefore, the polarization of ferroelectric domains affects the behavior of Li^+ ions in the electrolyte.

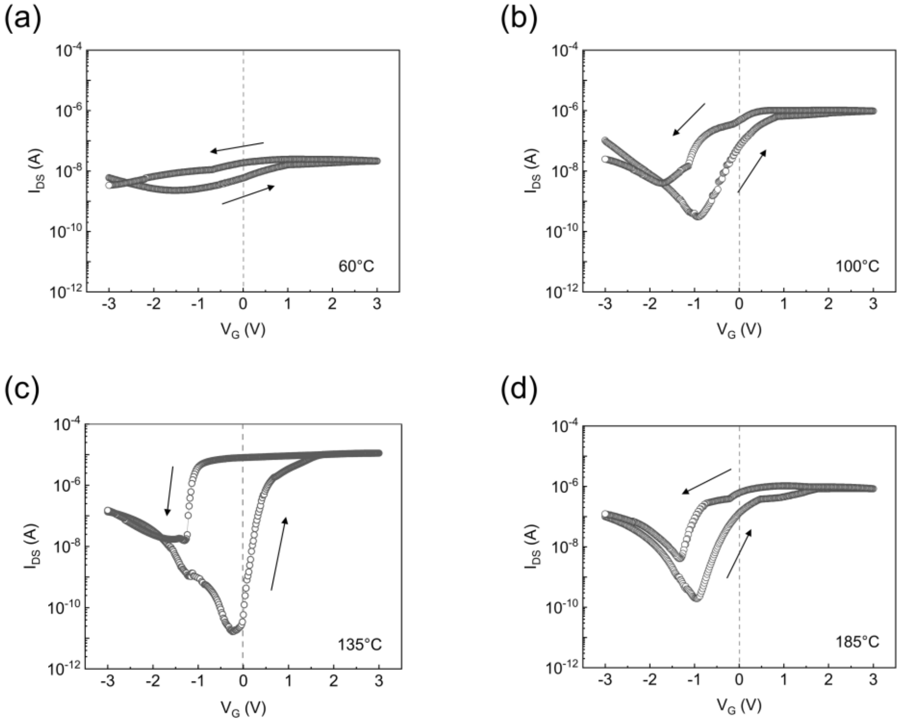

Figure 3.3. Transfer curves of Li$^+$ FP-EGTs with varying annealing temperatures of (a) 60 °C, (b) 100 °C, (c) 135 °C, and (d) 185 °C of PVDF-TrFE at a scan rate of 0.8 V s^{-1} (V_{DS} = 0.1 V).

3.3. Analysis of the working mechanism of Li^+ FP-EGT

Figure 3.4a,b show the elemental depth profile of each layer of Li^+ FP-EGT by Time-of-flight secondary ion mass spectroscopy (ToF-SIMS) measurement. Before the measurement, the Li^+ electrolyte is mechanically peeled off to mainly investigate the doped Li^+ ions. In the initial state, little intensity of Li is observed throughout the overall layers. This means that any diffusion or permeation of Li^+ ions is less likely to occur in the initial state at room temperature. After applying positive gate bias, however, the intensity of Li is increased in the ZnO layer. This result indicates that Li^+ ions are doped into ZnO. The electrochemical doping of Li^+ ions into the ZnO layer is referred to as pseudocapacitance and this reaction can be described by the following chemical equation[68]

$$xZnO + (2x+1)Li^{+} + (2x+1)e^{-} \leftrightarrow xLi_{2}O + LiZn_{x} \qquad (3.1)$$

During this reaction, two possibilities exist: (i) Li^+ locates at the substitutional site of Zn, and (ii) Li^+ locates at the interstitial site and forms the interstitial defects. Indeed, Li^+ preferentially locates at the interstitial sites in the ZnO matrix. Because of the small radius (~90 pm) of Li^+ ions, exchange with Zn requires higher activation energy than penetration to the interstitial site.[115],[116] This interstitial Li creates a shallow donor level in the band gap of n-type ZnO and Li is transformed into lithium oxide and lithium-zinc alloy, thereby increasing the electrical conductance of the ZnO layer.[116],[117] The electrical conductance of ZnO is, therefore, changed by the amount of doped Li^+ ions. Interestingly, Li intensity is not observed in PVDF-TrFE in both cases, indicating that Li^+ ions are likely to be neither trapped nor reacted in PVDF-TrFE. Although the reaction between Li^+ ions and C–F groups of PVDF-TrFE has a possibility of producing lithium fluoride,[118] applied electrical potential is not sufficient to break C–F bonds in PVDF-TrFE in this work. The possibility of reacting Li^+ ions and PVDF-TrFE, therefore, is significantly low. Furthermore, as shown in Figure 3.4c, no significant peak shifts in the F 1s region of PVDF-TrFE (CF_2–CF_2 or CF_2–CHF of 688.20 eV) in X-ray Photoelectron Spectroscopy (XPS) spectra are observed. Also, peaks of LiF (685.0 eV) in the F 1s region are not identified. This result supports the explanation of the chemical reactions by Li^+ ions.

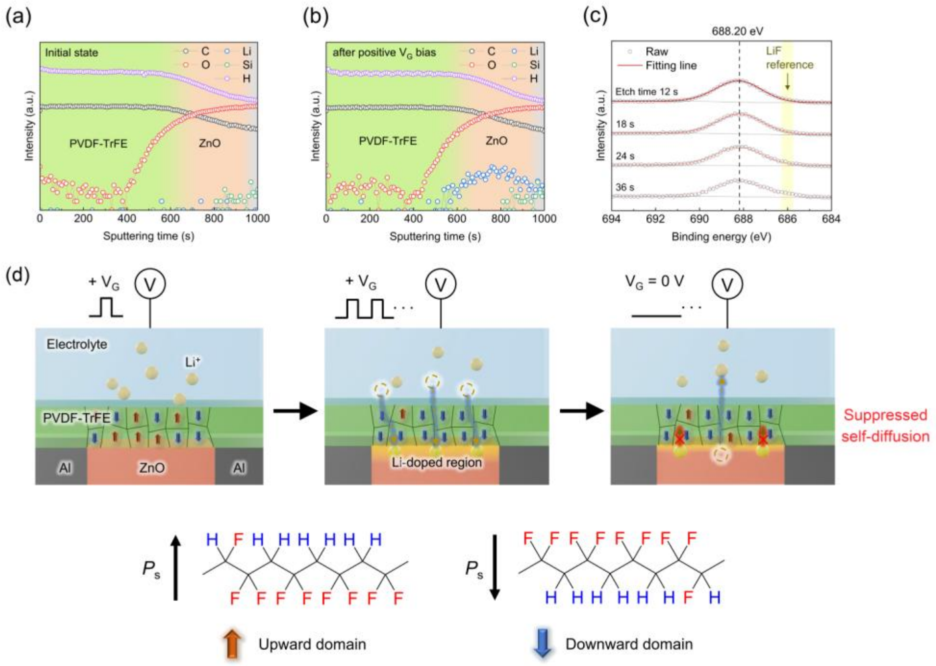

Figure 3.4. Elemental depth profile of Li FP-EGT (a) in an initial state and (b) after applying positive gate bias. To confirm the difference in Li intensity, a gate bias of 3 V amplitude is applied for 10 s. (c) XPS depth profile of F 1s region in PVDF-TrFE layer. (d) Working mechanisms of Li^+ FP-EGT. The partial polarization switching occurs sequentially in the ferroelectric domains of PVDF-TrFE by the applied gate pulses and Li^+ ions are also transported from the electrolyte to ZnO. Polarized domains also suppress the self-diffusion of Li^+ ions electrochemically doped in the ZnO layer.

Identifying the main factor for changes in the conductance of ZnO is crucial for not only realizing high-fidelity synaptic devices but also device fabrication. To investigate whether Li^+ ions are doped in the ZnO layer and the role of PVDF-TrFE, we use electrochemical impedance spectroscopy (EIS) to identify the electrochemical reaction. Bin-Wei Yao and co-authors successfully analyzed the behavior of Li^+ ions through frequency-varying capacitance and impedance.[119] They have shown that EIS measurement is an effective method for analyzing the behavior of ions and understanding the working mechanism of the EGT devices.

Here, due to the limitations of the experimental method, it is difficult to measure EIS in a three-terminal device structure.[120] We construct, therefore, a two-terminal structure, ITO(+)/electrolyte/PVDF-TrFE/ZnO/ITO(-), and investigate its parameters. The capacitance and impedance are measured with an AC voltage bias of 25 mV from 0.05 Hz to 10^6 Hz. Here, because the structure of the device and the applied AC voltage are different from the actual Li^+ FP-EGT, we focus on the behavior of Li^+ ions and the role of PVDF-TrFE. As shown in Figure 3.5, capacitance and impedance as a function of frequency can be divided into three distinct regions, I: bulk capacitance of the electrolyte, II: capacitance of EDL by Li^+ ions, and III: pseudocapacitance by Li^+ ions. To more accurately investigate the changes in capacitance, we confirm the impedance through correspondence with the capacitance. The impedance Z is expressed by the following equation[121]

$$Z = Z_R + Z_c \qquad (3.2)$$

$$Z_c = -j\frac{1}{\omega C} \qquad (3.3)$$

where Z_R is the resistance of the resistor, Z_c is the impedance of a capacitor, ω is the angular frequency ($\omega = 2\pi f$), and C is the capacitance of the capacitor. The magnitude of the impedance is

$$|Z|^2 = |Z_R|^2 + |Z_c|^2 \tag{3.4}$$

To confirm the change of impedance for frequency, the slope of log(Z)-log(f) is expressed as follows

$$\frac{d\log|Z|}{d\log f} \sim -S\frac{d\log C}{d\log f} + A \tag{3.5}$$

where S and A are constant.

To identify the role of PVDF-TrFE, we first investigate the capacitance and impedance of the electrolyte/PVDF-TrFE/ZnO device (blue points), as shown in Figure 3.5. In the high-frequency region (I), the capacitance is almost constant. In the middle frequency region (II), the capacitance increases rapidly as the frequency decreases. Below 10^3 Hz, however, the capacitance changes to almost constant again. This means that the charging of EDL is saturated with the formation of the stern layer (and effective diffuse layer) by ions at the interface below a certain frequency. In the low-frequency region (III), the capacitance additionally increases as the frequency decreases, indicating the presence of pseudocapacitance. In the case of electrolyte/ZnO (gray points), the capacitance of EDL dramatically increases compared to that of electrolyte/PVDF-TrFE/ZnO in region II. However, it is difficult to determine the pseudocapacitance in electrolyte/ZnO even when the frequency decreases after the charging of EDL is saturated. This difference can be speculated that the PVDF-TrFE layer enhances the formation of pseudocapacitance by electrochemically reacting Li^+ ions at the channel-electrolyte interface.[119], [121] Moreover, the behavior of Li^+ ions under an external electric field can be inferred from the value of impedance. Changes in capacitance, therefore, can be also inferred from the value of $\frac{d\log|Z|}{d\log f}$, as shown in Figure 3.5(b). These results of changes in $\frac{d\log|Z|}{d\log f}$ support the explanation of the electrochemical process by Li^+ ions. In the actual device, the operating voltage is higher (up to 3 V), so pseudocapacitance is likely to be found even at a high frequency above 30 Hz.

We additionally confirm the changes in charge transfer resistance (R_{ct}) by the introduction of the PVDF-TrFE interlayer. Nyquist plots are obtained with the same measurement method as in Figure 3.5. The equivalent circuit of the device is quite complex, we use a simplified circuit, based on the Randles cell, as shown in Figure 3.6.[122] As mentioned earlier, we focus only on the changes in charge transfer resistance because it is difficult to exactly investigate other parameters, such as bulk resistance (R_b), constant phase element (CPE_{ct}), and Warburg impedance (Z), in the proposed device structure. As shown in Figure 3.6(b), the measured Nyquist plot is fitted to the presented circuit to confirm R_b and R_{ct}. The measured R_b value in the device with PVDF-TrFE is 537 Ω, which is slightly higher than the R_b value of 412 Ω when PVDF-TrFE is absent. This increase is due to the addition of an electrical insulator between the electrolyte and the channel. However, the measured R_{ct} with PVDF-TrFE is 1357 Ω, which is significantly reduced compared to the values of 2199 Ω without PVDF-TrFE. These findings support the enhanced charge transfer of Li^+ ions by ferroelectric domains in PVDF-TrFE. The ion concentration at the channel/electrolyte interface increased, which can be attributed to the orientation of the dipoles within the ferroelectric domain. Also, the negative charge of the F-terminated surface allows Li^+ ions to easily penetrate the PVDF-TrFE layer because the F atoms in PVDF-TrFE give strong charge interaction between C–F groups and Li^+ ions.[118] Consequently, aligned F atoms provide transport paths that help Li^+ ions hop across the β-phase PVDF-TrFE interlayer. Meanwhile, a local electric field in downward polarized domains facilitates the transport of Li^+ ions, because electrons on the F-terminated surface are depleted and electrons on the H-terminated surface are excessed as the domains are polarized downward.[123], [124] The charge transfer is, therefore, enhanced in PVDF-TrFE along the direction of polarized domains, and the transport of Li^+ ions is more facilitated. These results support the working mechanism of Li^+ FP-EGT assisted by ferroelectric domains in PVDF-TrFE.

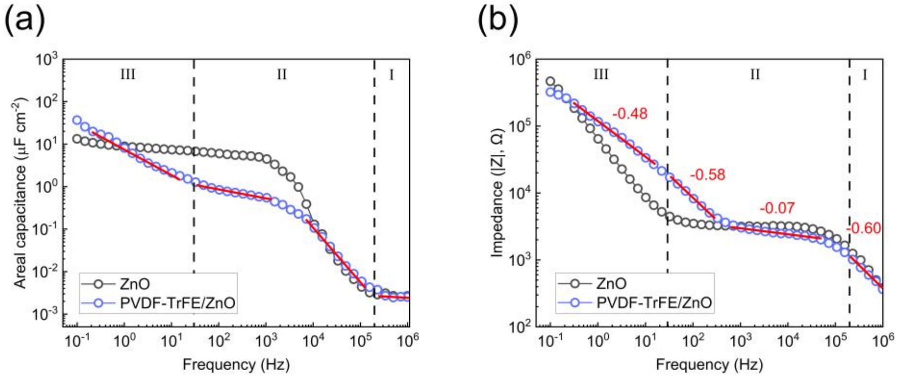

Figure 3.5. (a) Areal capacitance and (b) impedance as a function of applied AC voltage frequency. The capacitance and impedance of electrolyte/PVDF-TrFE/ZnO are measured with a 2-terminal structure, ITO/insulator/ITO. Inset values indicate the value of $\frac{d\log|Z|}{d\log f}$ in each process. In electrolyte/PVDF-TrFE/ZnO (blue points), When the changes in capacitance are almost constant, $\frac{d\log|Z|}{d\log f}$ shows a value of about -0.60 (fully charged EDL shows a value of -0.58). Reduced $\frac{d\log|Z|}{d\log f}$ indicates the capacitance is affected by a specific process by Li$^+$ ions.

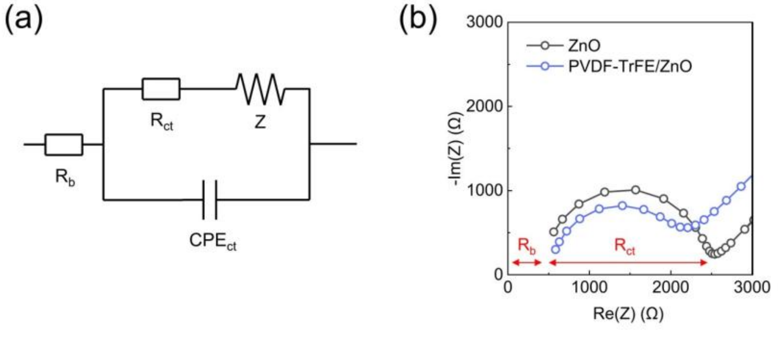

Figure 3.6. (a) Equivalent circuit for analysis of the difference in charge transfer resistance (R_{ct}). (b) Nyquist plot of the electrolyte/PVDF-TrFE/ZnO with 2-terminal structure, ITO/insulator/ITO.

As shown in Figure 3.4d, polarization switching of domains is partially occurred by applied gate pulses.[109],[114] This means that sequential conductance update is possible by the gradual transport of Li^+ ions at the channel-electrolyte interface. Also, spatiotemporal conductance changes in the ZnO layer are dominant by the effect of Li^+ ions. Because polarization switching of domains in PVDF-TrFE is much faster than a movement of Li^+ ions by an electric field.[125],[126] Self-diffusion of doped Li^+ ions in the ZnO layer to the electrolyte is also suppressed by downward polarized domains. This phenomenon is beneficial for demonstrating long-term synaptic plasticity. We speculate that Li^+ FP-EGT has a great advantage in demonstrating synaptic characteristics through analysis of the working mechanism for Li^+ FP-EGT.

3.4. Synaptic characteristics in Li^+ FP-EGT

In Li^+ EGT-based synaptic devices, Li^+ ions act as neurotransmitters (Na^+ or K^+) at the synaptic cleft in the biological synapse. The synaptic functions are triggered via electrical action potentials and the depolarization causes releasing of neurotransmitters between the adjacent two neurons, the presynaptic neuron and the postsynaptic neuron. Neurotransmitters can either excite or inhibit the potential of the postsynaptic neuron, which is destined by the number of released neurotransmitters.[3],[16],[27] Such flow of ions can be expressed by excitatory postsynaptic current (EPSC) and EPSC is expressed by the source-drain current (i.e., the channel current, I_{DS}) in EGTs. The working mechanism is mimicked in synaptic devices and emulating synaptic plasticity is crucial to synaptic devices for neuromorphic computing. Figure 3.7a shows EPSC responses in Li^+ FP-EGT by single gate pulse with various amplitudes at a fixed pulse width (t_w) of 10 ms. EPSC shows the peak as the gate pulse is applied, thereafter rapidly decreasing to a slightly excited value compared to the initial state, indicating short-term synaptic plasticity (STP). This behavior is induced by EDL because EDL is abruptly formed by an applied external electric field and easily dissipated after applying an electric field due to charge asymmetry in the electrolyte.

Specifically, when a positive gate pulse is applied to the Li^+ electrolyte, a 2-step process occurs: i) formation of EDL at the channel (or PVDF-TrFE)/electrolyte interface and ii) gradually penetrate PVDF-TrFE and doped into the ZnO channel.[127] To quantitatively analyze changes in the effect of each process, we define the change ratio of current compared to the initial value: peak current (I_P ratio = I_p/I_0) and remanent current (I_r ratio = I_r/I_0) at 3 s after the applying gate pulse. As the amplitude of the gate pulse increases, the EPSC exponentially increases in both cases of I_p and I_r ratio, as shown in Figure 3.7b. This indicates that the major gating effect is due to the movement of Li^+ ions, rather than due to the bulk capacitance of the electrolyte.[56] Also, the EPSC is gradually saturated as the pulse width increases, as shown in Figure 3.7c. Because Li^+ ions exhibiting the gating effect mainly exist as a stern layer of EDL at the channel-electrolyte interface.[92], [93] The effective concentration of Li^+ ions at the interface, therefore, is saturated following the increase in pulse width. As mentioned above, the overall I_r ratio, however, is much smaller than the I_p ratio. As mentioned above, although the peak current originates from the formation of EDL at the channel-electrolyte interface, the main cause of the remanent current after the gate pulse is most likely the doping effect of Li^+ ions in ZnO.

Most importantly, emulating LTP characteristics is an essential key factor in the characterization of synaptic devices. As shown in Figure 3.7e,f, EPSCs are triggered by various amplitudes and pulse numbers of gate pulses. The maximum peak value of EPSCs increases as the amplitude or number of applied gate pulses increases with a similar tendency shown in Figure 3.7b,c. Unlike the EPSC driven by a single gate pulse shown in Figure 3.7a, however, increased EPSC does not decrease rapidly to their initial state, but rather last for over 500 s. When positive gate pulses with high amplitude or large numbers are applied, Li^+ ions can have sufficient energy to penetrate the PVDF-TrFE and become doped into the ZnO. In other words, penetration of PVDF-TrFE and doping into the ZnO matrix requires a certain activation energy. Therefore, if the amplitude of the applied gate pulse is high or the number of gate pulses is large, the number of Li^+ ions that overcome the activation energy also increases, resulting in LTP. During this process, ferroelectric domains in PVDF-TrFE can help reduce the activation energy (which is related to charge transfer resistance in Figure 3.6, thereby prominent LTP characteristics that can be observed. Overall, Li^+ FP-EGT shows synaptic characteristics by successfully mimicking the biological synaptic behavior.

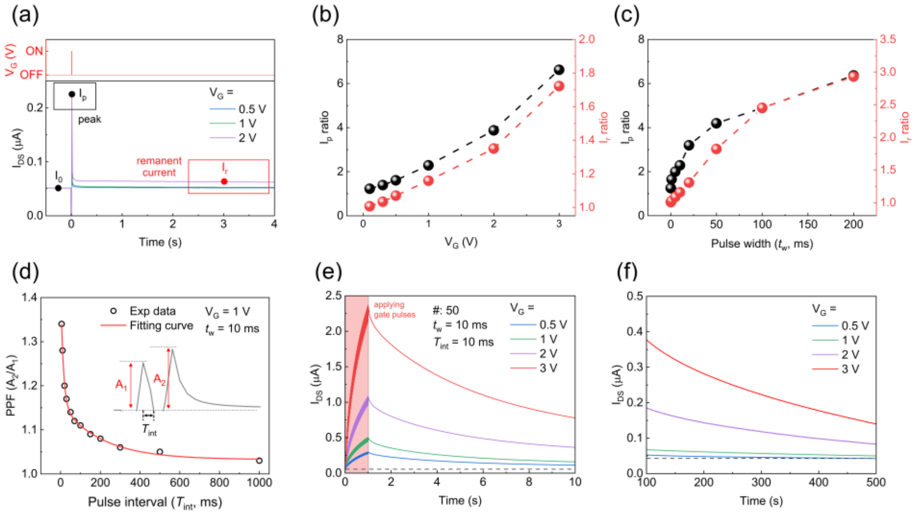

Figure 3.7. (a) EPSC responses by a single gate voltage pulse with amplitudes of 0.5 to 2 V (t_w = 10 ms) at channel voltage (V_{DS}) = 0.1 V. Dependence of ratio of channel current as a function of (b) the amplitude of the gate voltage pulse and (c) the width (t_w) of the gate voltage pulse. (d) Dependence of paired-pulse facilitation (PPF) on pulse interval (T_{int}) by 2 consecutive gate pulses. (e) LTP characteristics as a function of the amplitudes of gate voltage pulses and (f) its retention tests for 500 s.

3.5. Identifying the origin of LTP characteristics

As the partially polarized domains inhibit self-diffusion of Li^+ ions doped in ZnO to the electrolyte, the LTP characteristics are maintained for up to hundreds of seconds, where the mechanism is previously explained in the analysis in Figure 3.4. We additionally investigate the electrical characteristics of Li^+ EGT without PVDF-TrFE and FP-EGT with an ionic liquid (IL FP-EGT) to identify the origin of LTP characteristics. As shown in Figure 3.8, Li^+ EGT shows a small hysteresis window in the transfer curve, and rapidly decaying I_{DS} behaviors are found in EPSC responses (LTP characteristics are only maintained for a few tens of seconds). This indicates that PVDF-TrFE greatly influences the LTP characteristics. We also investigate the effect of cation size to demonstrate LTP characteristics. The electrical characteristics of FP-EGT with ionic liquid ($[EMIM]^+[TFSI]^-$) is shown in Figure 3.9. Here, the ionic radius of Li is about 90 pm (6-coordinate) and the length of the shortest axis of $[EMIM]^+$ is about 500 pm. Penetration of $[EMIM]^+$ into the ZnO lattice, therefore, is quite difficult due to its size, and also low electrochemical activity with ZnO. Not only Li^+ ions but also $[EMIM]^+$ can, however, penetrate PVDF-TrFE because of its high free volume and large pores in the polymer matrix.[128], [129] Nevertheless, in IL FP-EGT, hysteresis in the transfer curve and LTP characteristics in EPSC response are hardly found. Overall, the demonstration of the LTP characteristic is less likely due to the ferroelectric gating of PVDF-TrFE or EDL by Li^+ ions but rather the doping effect by Li^+ ions is dominant.

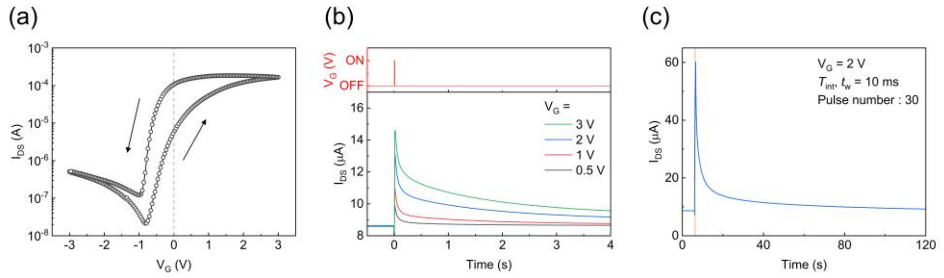

Figure 3.8. Electrical characteristics of Li^+ EGT without PVDF-TrFE. (a) Transfer curve of Li^+ EGT at 0.8 V s^{-1} fixed scan rate (V_{DS} = 0.1 V). (b) STP characteristics by a single gate voltage pulse with amplitudes of 0.5 to 3 V (t_w = 10 ms) at channel voltage (V_{DS}) = 0.1 V. (c) LTP characteristic by 30 consecutive gate pulses.

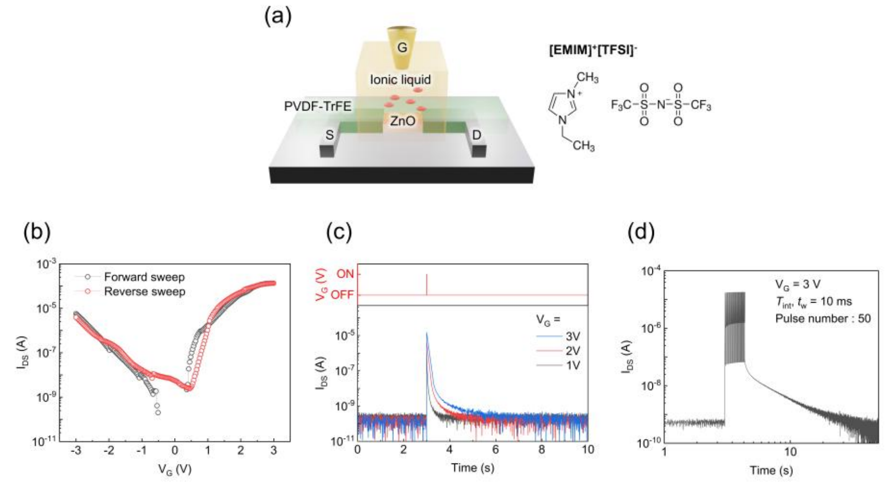

Figure 3.9. Electrical characteristics of IL FP-EGT. (a) Schematic illustration of IL FP-EGT. (b) Transfer curve of IL FP-EGT at a 0.8 V s^{-1} fixed scan rate (V_{DS} = 0.1 V). (c) STP characteristics by a single gate voltage pulse with amplitudes of 1 to 3 V (t_w = 10 ms) at channel voltage (V_{DS}) = 0.1 V. (d) LTP characteristic by 50 consecutive gate pulses.

3.6. Conductance update in Li^+ FP-EGT

Modulating multi-level conductance is the main feature in the artificial synapse for high-fidelity analog neuromorphic computing. Herein, during conductance update, achieving high linearity and large dynamic range with low operation voltage is the most crucial goal for the successful development of energy-efficient synaptic devices. Figure 3.10a shows the conductance update in Li^+ FP-EGTs with different measurement conditions. We fixed t_w and T_int to 10 ms during conductance update, and vary the amplitude of gate voltage pulse (2 V/-1 V, 3 V/-1.5 V) on the long-term potentiation (LTP)/long-term depression (LTD) side. We confirm that a successful conductance update is obtained even with the amplitude of 3 V/1.5 V and pulse number (#) 256/256 of gate voltage pulses. To determine the number of effective conductance states, we present an effective number of states (NS_eff), which is defined as follows[14]

$$\text{NS}_\text{eff} = \text{ the number of } G_n \text{ of } \frac{G_n - G_{n-1}}{G_{max} - G_{min}} > 0.0005 \ (n = 1, 2, 3 \ldots) \quad (3.6)$$

where G_{max} is the maximum conductance in conductance update, G_{min} is the minimum conductance, and n is the pulse number. As presented in Figure 3.10a, all of the conductance states in conductance updates of #64 and #128 are effective (the number of all states = NS_eff). NS_eff on the LTD side of conductance updates of #256 is, however, quite different from the number of states, 206 at 2 V/-1 V and 234 at 3 V/-1.5 V. Also, Li^+ FP-EGT operates stably over 100 cycles in conductance update without significant degradation, as shown in Figure 3.10b.

To quantitatively investigate each conductance update, we extract parameters for each measurement condition. Figure 3.10c-h shows extracted parameter values from Figure 3.10a, including nonlinearity (NL), asymmetry (AS), and dynamic range

(G_{max}/G_{min}). We obtain the parameter values by fitting each equation to the conductance data (Details of each fitting equation in supplementary material Note 3). Specifically, as the amplitude of the applied gate voltage or the pulse number is increased, dynamic range and nonlinearity are increased. These results can be explained by the concentration of electrochemically doped Li^+ ions in the ZnO layer. When Li^+ ions from the electrolyte penetrate the ZnO layer, they occupy the interstitial sites of the ZnO matrix mostly toward the surface. The changes in the electrical conductivity of ZnO, therefore, tend to be saturated. As a result, nonlinearity during conductance update increases. Likewise, as the amplitude of the applied voltage pulse increases or the pulse number increases, the amount of Li^+ ions doped in the ZnO matrix also increases. A large dynamic range, therefore, can be obtained. Li^+ FP-EGT shows, as shown in Figure 3.10c,d, the lowest NL_P of 0.19 at 2 V/1 V and #64, and also shows a value of 1 or less under most measurement conditions. Also, as shown in Figure 3.10e,f, most values of AS are less than 0.3, except #256, indicating conductance update in Li^+ FP-EGT shows high symmetry between LTP and LTD. The largest value of the dynamic range is 92.42 at 3 V/-1.5 V and #256, which is sufficiently high for high-fidelity analog computing.

Fig. 3.10i shows the 20 device-to-device distribution of conductance update for the 100th cycle at 3 V/-1.5 V and #256. It is confirmed that there is not much variation between each device. Although the parameter value of each device shows a little deviation, it is less than about 8.6%. It can be expected that the output deviation will not appear significantly when Li^+ FP-EGTs are implemented in the parallel circuit array.

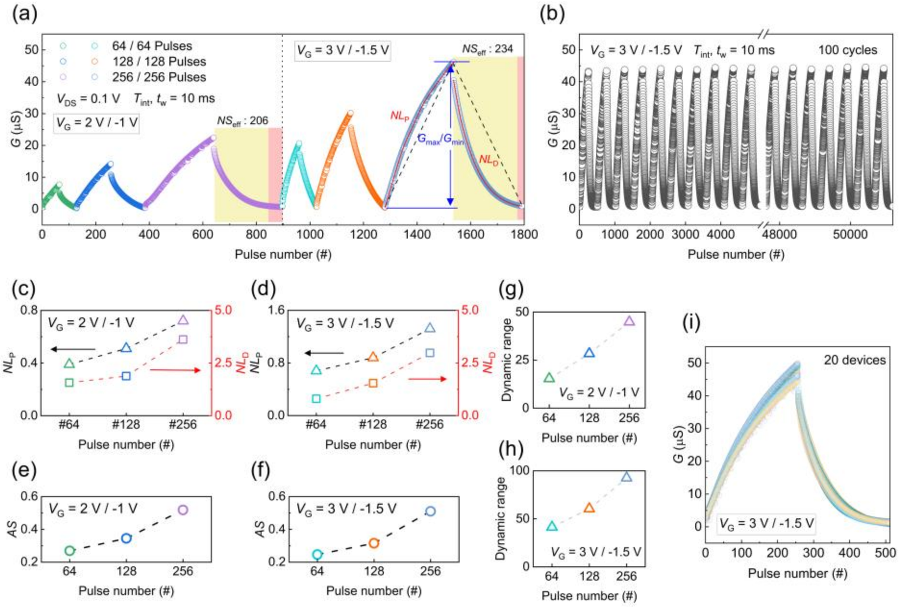

Figure 3.10. (a) LTP/LTD characteristics with varying amplitudes and numbers (#) of gate voltage pulses. (b) Cycle-to-cycle distribution test over 100 cycles. Extracted parameter values from Fig. 4(a), including (c,d) nonlinearity on the LTP/LTD side (NL_P/NL_D), (e,f) asymmetry (AS), and (g,h) dynamic range (G_{max}/G_{min}) in each measurement condition of conductance update. (i) The 20 device-to-device distributions of conductance update at the 100th cycle.

3.7. Mechanical and environmental stability test

The application of synaptic devices on the flexible substrate expands the possibilities of specific neuronal devices such as wearable, bio-implantable electronics.[130] PVDF-TrFE and Li^+ electrolytes have the advantage of high flexibility and good mechanical durability. We fabricate Li^+ FP-EGTs on a polyimide (PI) substrate and investigate their conductance update. As shown in Figure 3.11a, conductance is measured in the introduction of tensile stress at a bending radius of 1.0 cm, 0.8 cm, and 0.6 cm. The measured conductance update in each device is shown in Figure 3.11b. Although the conductance update of Li^+ FP-EGT in the flat condition (shown in Figure 3.10a) and the bent condition is slightly different, no significant degradation is found. As shown in Figure 3.11c-e, comparing parameters in conductance update, including NL, AS, and dynamic range, although a slight increase in NL can be found, it is acceptable for a small difference in each parameter. As mechanical stress exists in PVDF-TrFE, surface energy is larger than in flat conditions (increased pore size), which is speculated to be the cause of the decreased dynamic range and the increased NL. Furthermore, even after bending the device over 1000 cycles at a bending radius of 0.6 cm, Li^+ FP-EGT shows similar conductance update as the initial state despite a slight degradation, as shown in Figure 3.11f,g.

We also investigate the thermal and humidity stability of Li^+ FP-EGT. As shown in Figure 3.12, a slight degradation can be observed when Li^+ FP-EGT is operating at temperatures above 60 °C. Particularly, above 80 °C, the operation of Li^+ FP-EGT fails with significant deterioration. Also, as shown in Figure 3.13, in high humidity environments, the result in conductance update with low fidelity can be found. Low stability to high temperatures (above 40 °C) is likely to be improved by replacing the electrolyte, such as LiPON or $LiSiO_2$,[105], [131] and stability for high humidity conditions can be improved via device encapsulation.

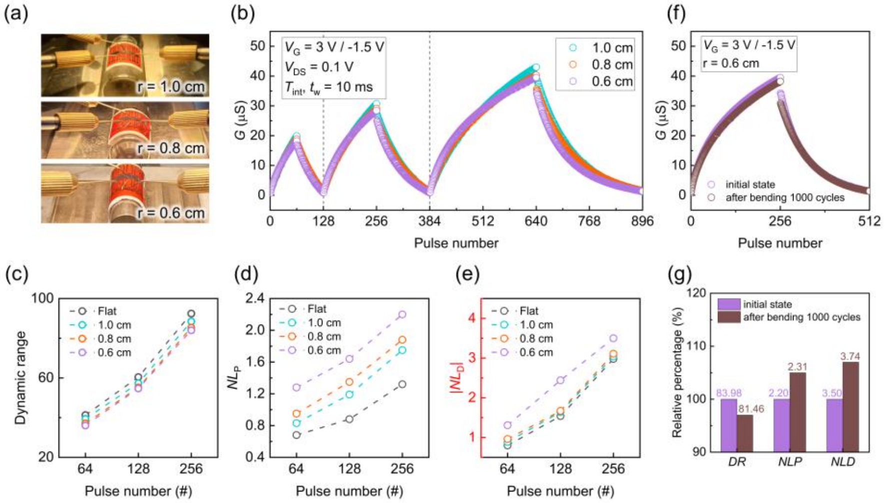

Figure 3.11. (a) Actual image of Li^+ FP-EGT on the polyimide (PI) substrate. (b) LTP/LTD characteristics in each bent condition at bending radii 1.0 cm, 0.8 cm, and 0.6 cm. Extracted parameter values from Figure 3.11b, including (c) dynamic range and (d,e) nonlinearity on the LTP/LTD side. (f) Comparison of the difference in conductance update between the initial state and the state after bending 1000 cycles. (g) Relative comparison of each parameter value from Figure 3.11f, where relative parameter values in the initial state are 100%.

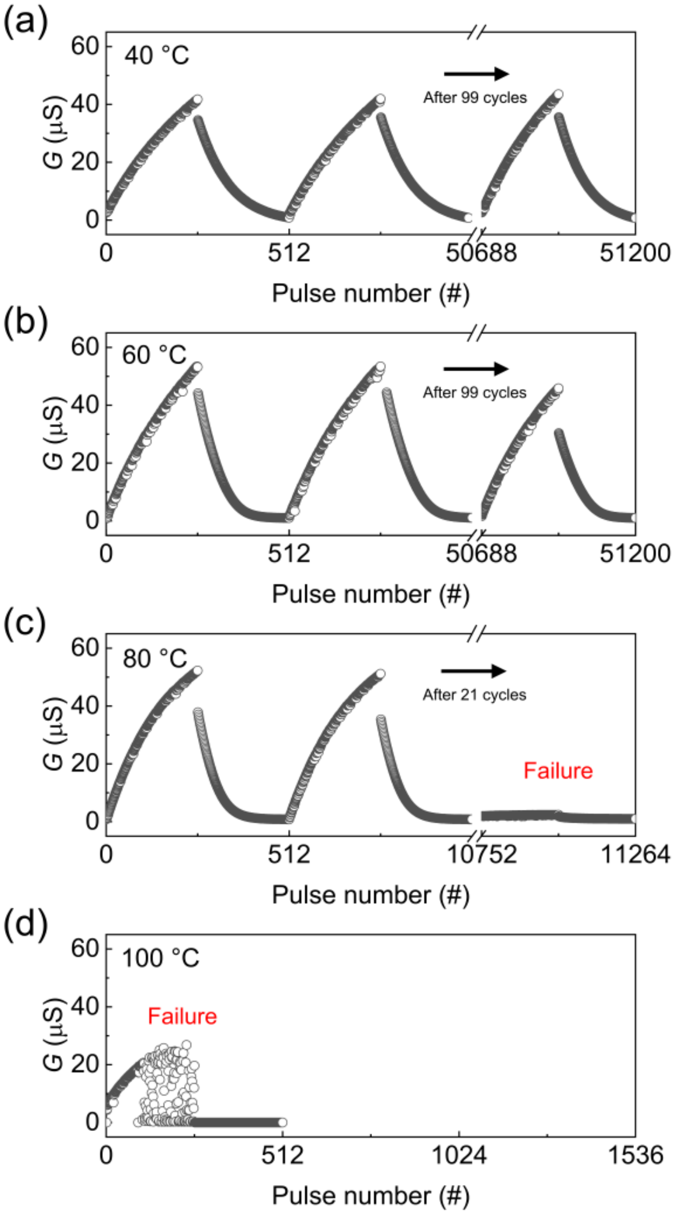

Figure 3.12. Thermal stability test for Li$^+$ FP-EGT at a temperature of (a) 40 °C, (b) 60 °C, (c) 80 °C, and (d) 100 °C. The measured electrical condition is the same as Figure 3.10b.

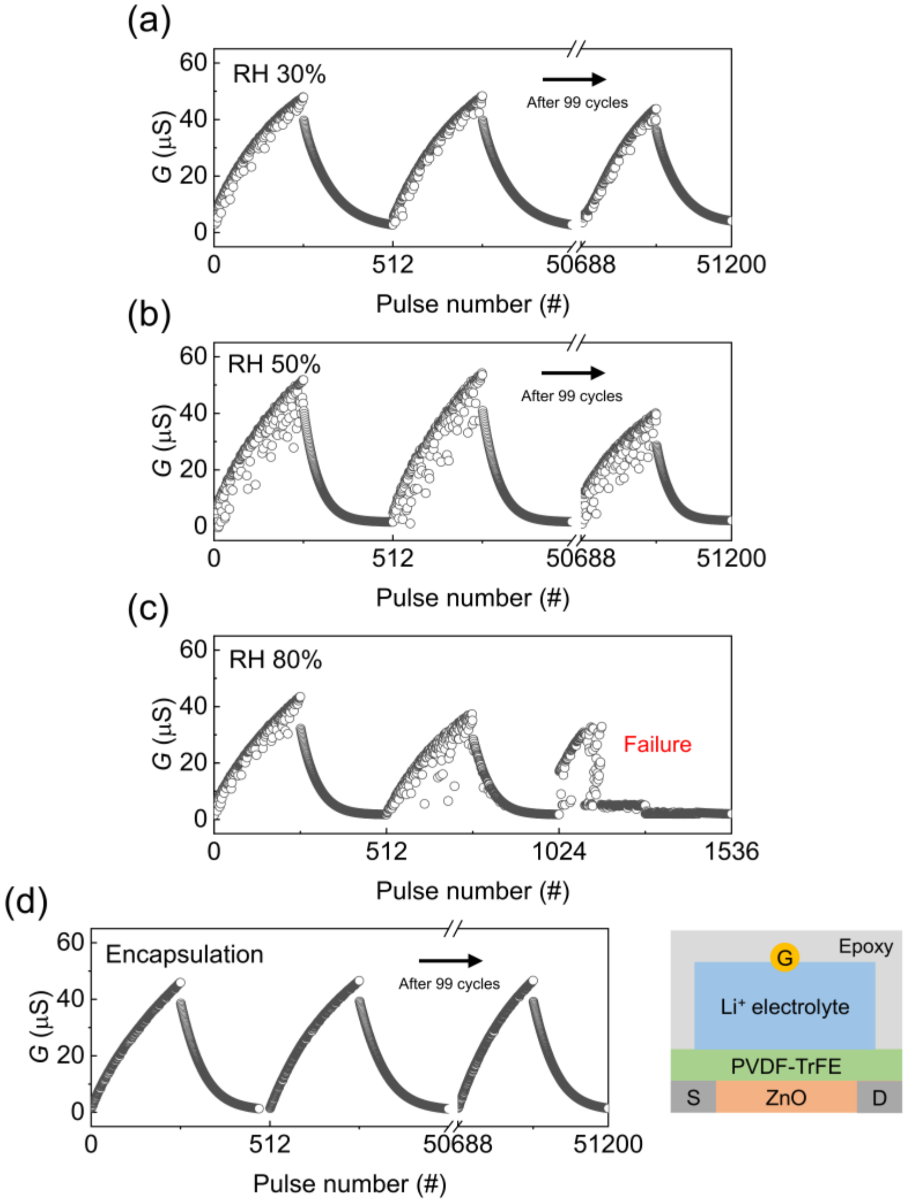

Figure 3.13. Humidity stability test for Li^+ FP-EGT at a relative humidity (RH) of (a) 30%, (b) 50%, (c) 80%, and (d) 80% with device encapsulation. The measured electrical condition is the same as Figure 3.10b. Here, for encapsulation, we use epoxy to cover the entire device and Au wire is used as a gate electrode.

3.8. Application for inference tasks using CNN

Based on the synaptic characteristics in Li^+ FP-EGT, we conduct the simulation of the recognition tasks using a convolution neural network (CNN) to confirm the performance of Li^+ FP-EGT.[101], [132] In the simulation, inference accuracy is obtained for the CIFAR-10 dataset. As shown in Figure 3.14a, the CIFAR-10 dataset contains 10 class categories (truck, airplane, horse, etc.), where the images consist of 32 × 32 pixels and each image has 3 colors; red, green, and blue (32 × 32 × 3). CNN consists of 8-layers, including convolution, pooling, and fully connected layers, and synaptic weights in convolution layers and fully connected layers are modulated by Li^+ FP-EGTs based on the conductance update in Figure 3.10. In the simulation, 50000 training and 10000 inference/feed-forwarding processes per epoch are conducted for a total of 256 epochs. The circuit diagram composed of Li^+ FP-EGT arrays corresponding to the fully-connected layers is shown in Figure 3.14b.

Before the conducting recognition task using CNN, a simulation of the multilayer perceptron, which is a class of feed-forward artificial neural network (ANN), is conducted to determine which measurement condition during conductance update is suitable.[133] As a result of the inference accuracy of CNN, as shown in Figure 3.14c, we confirm that the maximum recognition accuracy is 89.13%, and the value of the ideal device is 91.22%. Due to the high linearity and large dynamic ratio of Li^+ FP-EGT during conductance update, the accuracy of Li^+ FP-EGT is almost close to the value of the ideal device. Moreover, the achieved accuracies in the bent condition (at r = 0.6 cm) are 85.27% in the initial state, and 83.59% after the bending 1000 cycles, as shown in Figure 3.14d. The reason for the lowered accuracy in the bent condition is the nonlinearity of the LTP has increased. Nevertheless, it shows that Li^+ FP-EGT is suitable for an artificial synapse even in a flexible system because it maintains an accuracy of over 80%.

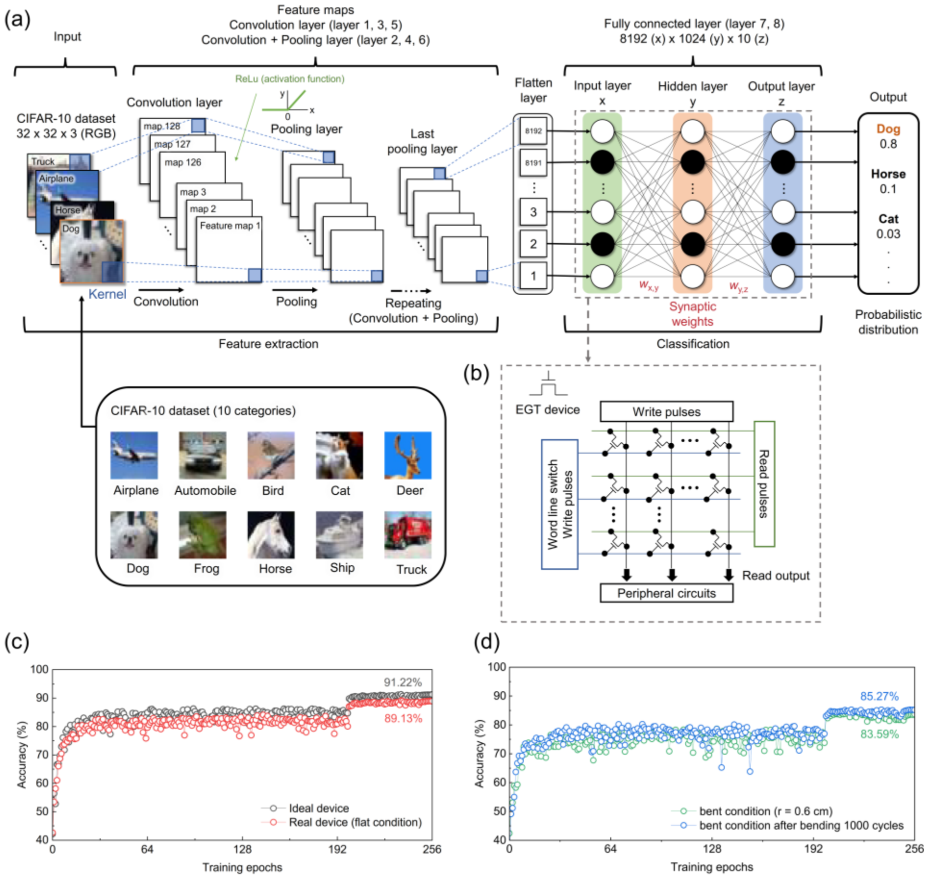

Figure 3.14. (a) Convolution neural networks consisted of convolution layers, pooling layers, and fully connected layers. (b) Circuit diagram showing fully connected layers composed of Li^+ FP-EGT arrays and the peripheral circuit. (c) Inference accuracies in the ideal case of the device (gray) and the experimental case of the device (red). An ideal device indicates a case where nonlinearity is 0 and cycle-to-cycle distribution and device-to-device distribution are 0%. (d) Inference accuracies in the bent case of the device (blue) and bent case after bending 1000 cycles of the device (green).

3.9. Experimental method

***Materials*:** Boron-doped p^{++} Si wafers (< 0.001 Ω) with 200 nm-thick thermally grown SiO_2 and polyimide (0.07 mm thickness) were used as the substrate. Zinc nitrate hexahydrate ($Zn(NO_3)_2 \cdot 6H_2O$, > 99% purity), sodium hydroxide (NaOH, 99.99% purity), lithium trifluoromethanesulfonate (LiOTf, 99.995% purity), Poly(ethylene glycol) dimethacrylate (PEGDMA, M_w ~ 550), 2-hydroxy-2-methylpropiophenone (HOMPP, 97% purity), Poly(vinylidene fluoride-co-trifluoroethylene) (PVDF-TrFE, 70:30 in mol %), Au wire (0.25 mm, 99.99% purity), epoxy resin were purchased from Sigma-Aldrich. Ammonium hydroxide (NH_4OH, 25-28% purity) and 2-butanone (99% purity) were purchased from Daejung Chemicals. Lithium bis(trifluoromethanesulfonyl)imide (LiTFSI, > 98% purity) and 1-Ethyl-3-methylimidazolium bis(trifluoromethanesulfonyl)imide ($[EMIM]^+[TFSI]^-$, >98% purity) were purchased from TCI.

***Preparation of the ZnO solution*:** 0.5 M $Zn(NO_3)_2 \cdot 6H_2O$ was dissolved in 15 mL de-ionized (DI) water. 2.5 M NaOH in 10 mL DI water was added to the ZnO solution. After mixing the prepared solution, the solution was centrifuged five times with DI water at 5000 rpm for 5 min. After centrifugation, the precipitate was collected, and dissolved in 20 mL NH_4OH with 25 mL DI water.

Preparation of Li$^+$ electrolyte: 21 M LiTFSI and 7 M LiOTf were dissolved in DI water, and PEGDMA was added at a weight ratio of 1:1 with the solution. To solidify by UV curing, HMOPP was added in a 2 wt% to the mixture. Then the electrolyte mixture was stirred for 6 hr vigorously. The prepared electrolyte was stored in a refrigerator at 4 ℃.

***Preparation of $[EMIM]^+[TFSI]^-$ electrolyte*:** $[EMIM]^+[TFSI]^-$, PEGDMA, and HMOPP were mixed at a weight ratio of 22:2:1. Then the electrolyte mixture was stirred for 6 hr vigorously. The prepared electrolyte was stored in a refrigerator at 4 ℃.

Device fabrication: The SiO_2/Si substrate was cleaned by subsequent sonication in detergent for 15 min, DI water rinsing for 15 min, sonication in acetone, and isopropanol for 15 min each, followed by UVO treatment for 15 min. The prepared ZnO solution was spin-coated at 3000 rpm for 30 s on the SiO_2/Si substrate. The ZnO-coated substrate was heated to 300 ℃ for 1 h to sinter the ZnO films. The thickness of the ZnO layer was about ~ 6 nm. After then, the channel region was patterned using photolithography and a wet etching process to define the channel region. The Al source, drain, and side gate electrodes were deposited to a thickness of 100 nm using thermal evaporation and patterned by the lift-off process. The channel width and length were 500 μm and 100 μm, respectively. Then, the PVDF-TrFE solution was spin-coated on the fabricated device in a glove box. Subsequently, the device was heated to 135 ℃ for 4 h to obtain the crystalline β-phase of PVDF-TrFE. After spin-coating, the prepared Li^+ electrolyte mixture was spin-coated at 500 rpm for 15 s, and then the device was placed in an atmosphere of humidity under 3% for 30 min to allow the electrolyte to sufficiently permeate on PVDF-TrFE. Finally, to solidify the electrolyte, the electrolyte was cured with a UV lamp at 365 nm (600 mJ cm^{-2}) for 10 s. A gold probe tip was used as a gate electrode during measuring electrical characteristics by perpendicularly contacting the center of the channel.

***Device characterizations and measurements*:** The roughness of PVDF-TrFE thin films is investigated using AFM (XE100, PSIA). Especially, the surface was examined utilizing low-noise AFM. The topological AFM images were obtained in tapping mode using a silicon probe with a cantilever spring constant of 42 N m^{-1}. PVDF-TrFE thin-films were scanned and recorded using an X-ray diffractometer (D8 ADVANCE, Bruker Corporation) with an X-ray generator from 15 to 40 of 2θ (diffraction angle) using 40 kV and 150 mA (λ =0.154 nm) of Cu Kα radiation in grazing-incidence mode. The areal capacitance of the devices was measured using electrochemical impedance spectroscopy (Biologic, VSP) and a precision LCR meter (Agilent 4284A) in an AC voltage bias of 25 mV. ToF-SIMS analysis with the depth profile mode was performed to evaluate the ion-trapping tendency of Li^+ ions at a pressure below 3.8×10^{-9} Torr (TOF.SIMS-5, ION-TOF). A Bi^+ (30 keV, 0.6 pA) ion beam was used as the primary source for detecting the composition of facile-section, and sputtering with Ar gas cluster ion source (2.5 keV, 0.9 nA) was used for depth profiling analysis in negative polarity (analysis area; 100 × 100 μm^2, etching area; 300 × 300 μm^2). The chemical properties of PVDF-TrFE films were characterized from XPS measurement (AXIS Supra+, Kratos). The transfer characteristics and pulse measurements of devices were characterized by Agilent 4155B semiconductor parameter analyzer and Keysight B2902A source/measure unit.

3.10. Conclusion

In conclusion, we demonstrate Li^+ EGTs integrated with PVDF-TrFE as a channel-electrolyte interlayer that shows enhanced long-term plasticity (>500 s), high linearity, and large dynamic range (up to 92.42) during conductance update. PVDF-TrFE gives the transport path of Li^+ ions at the channel-electrolyte interface with reduced charge transfer resistance by ferroelectric polarization of domains, confirmed by ToF-SIMS and capacitance-impedance measurement. Also, high linearity in conductance update is obtained by gradual penetration of Li^+ ions in the ZnO layer through partial polarization switching of ferroelectric domains. As the polarized domains are maintained once an electric field is applied, the self-diffusion of Li^+ ions doped in the ZnO layer is also suppressed, thereby strongly enhancing LTP characteristics. Simulation of inference accuracy based on convolution neural network shows Li^+ FP-EGT is suitable for application as an artificial synapse with an accuracy of 89.13%, which is comparable to the value of the ideal device of 91.22%. Even in the bent condition on the polyimide substrate, the achieved accuracy of Li^+ FP-EGT is 85.27% without any significant degradations due to its high mechanical flexibility. We emphasize that ferroelectric domains can effectively modulate the transport of Li^+ ions at the channel-electrolyte interface, implying that considering the dynamics of ions at the interface is crucial to developing an EGT-based artificial synapse. These findings will give a new methodological design rule and remarkable applicability of EGTs in the field of artificial synapses for neuromorphic computing.

Chapter 4. Conclusion and outlook

Based on the fundamental principles of electrostatic interactions, Chapter 2 of this dissertation presents the incorporation of F-SAM as an interlayer, inducing electrostatic attraction with lithium ions to investigate the electrical characteristics with nonvolatility. In Chapter 3, the introduction of a ferroelectric polymer is explored to examine the changes in ion dynamics at the interface.

Chapter 2 demonstrated lithium electrolyte-gated EGTs with F-SAMs that emulates non-volatile conductance update with a long retention time, high linearity, and a high dynamic range. Through investigating the electrical analysis and chemical analysis, we elucidate that major ion-trapping sites are fluoroalkyl chains of F-SAM, which significantly increase the retention time of lithium ions at the channel-electrolyte interface. Also, fluoroalkyl chains sequentially trap and de-trap lithium ions via coulombic attraction between lithium ions and C−F bonds, which enables non-volatile conductance update with high linearity and symmetry. The introduction of the F-SAM interlayer is robustly effective in developing synaptic devices based on EGTs, and dealing with charge interaction is essential to improve synaptic characteristics. In summary, I emphasize that electrostatic interactions can control the movement of ions at the interface, and discussed how this phenomenon influences the electrical characteristic changes in EGT devices.

In Chapter 3, I investigated whether the ferroelectric domains can effectively enhance ion penetration at the interface and potentially hinder self-discharge of doped lithium ion. This effect is also attributed to the internal electric field by the dipoles that form the domain. Additionally, I examined the relationship between domain switching and ion penetration. Through considering the changes in ion dynamics and physical properties of ferroelectric material, I successfully achieved the required electrical characteristics in artificial synapse devices for analog computing. In summary, my research was focused on making EGT devices suitable for artificial synapses, resulting in the development of a device with long-term retention characteristic sas well as a near-linear conductance update capability, making it suitable for analog computing, which were previously lacking in EGT devices.

Research on artificial synapses has the potential to significantly impact various industries by advancing technologies in electronics, artificial intelligence, and neuromorphic computing. As artificial synapses mimic the function of biological synapses, they enable the development of more energy-efficient, flexible, and adaptive computing systems. In the semiconductor industry, they could lead to the creation of next-generation processors that require less power while offering greater processing speeds, which is crucial for applications in edge computing and the Internet of Things (IoT). In artificial intelligence, artificial synapses could improve machine learning models, allowing for faster learning and more accurate predictions with lower energy consumption. Additionally, the development of neuromorphic systems could revolutionize robotics, enabling machines to learn and respond to their environments in a more human-like manner. Industries such as healthcare, autonomous vehicles, and smart cities could benefit from these advancements, leading to innovations in medical diagnostics, driver assistance systems, and urban infrastructure management. Overall, I emphasized that artificial synapse research offers significant potential for transforming the landscape of computing and its practical applications in industry.

In this dissertation, I successfully demonstrated EGT-based artificial synapses based on electrostatic interactions. However, the limitation of these researches lies in demonstrating experimental characteristics at the device level. Therefore, for this research to emphasize its practical points, it is necessary to demonstrate that the proposed ideas can be applied to integrated systems, such as crossbar arrays or more complicated systems. Also, there are some remained problems in EGT devices, such as slow computing speed, low stability and complexity of fabricating process, compared to conventional processors. These issues are related to the physical and chemical properties of the materials in EGTs, and further research is needed to enhance ion conductivity or to develop solid electrolytes that are better suited for artificial synapse applications. By overcoming these challenges, it would be possible to make significant progress toward the commercialization of computing chips based on EGT devices. Nevertheless, this dissertation holds significant research value as it addresses the crucial aspect of charge interaction in the development of EGT devices. I believe it could serve as a key idea in future EGT-related researches.

Bibliography

[1] W. Zhang *et al.*, “Neuro-inspired computing chips,” *Nat. Electron.*, vol. 3, no. 7, pp. 371–382, 2020, doi: 10.1038/s41928-020-0435-7.

[2] M. J. van Setten *et al.*, “Oxygen Defect Stability in Amorphous, C-Axis Aligned, and Spinel IGZO,” *ACS Appl. Electron. Mater.*, vol. 3, no. 9, pp. 4037–4046, Sep. 2021, doi: 10.1021/acsaelm.1c00553.

[3] I. Chakraborty, A. Jaiswal, A. K. Saha, S. K. Gupta, and K. Roy, “Pathways to efficient neuromorphic computing with non-volatile memory technologies,” *Appl. Phys. Rev.*, vol. 7, no. 2, p. 021308, 2020, doi: 10.1063/1.5113536.

[4] Y. Choi, S. Oh, C. Qian, J.-H. Park, and J. H. Cho, “Vertical organic synapse expandable to 3D crossbar array,” *Nat. Commun.*, vol. 11, no. 1, p. 4595, 2020, doi: 10.1038/s41467-020-17850-w.

[5] V. K. Sangwan and M. C. Hersam, “Neuromorphic nanoelectronic materials,” *Nat. Nanotechnol.*, vol. 15, no. 7, pp. 517–528, 2020, doi: 10.1038/s41565-020-0647-z.

[6] I. Chakraborty, A. Jaiswal, A. K. Saha, S. K. Gupta, and K. Roy, “Pathways to efficient neuromorphic computing with non-volatile memory technologies,” *Appl. Phys. Rev.*, vol. 7, no. 2, 2020, doi: 10.1063/1.5113536.

[7] Y. Li *et al.*, “Anomalous resistive switching in memristors based on two-dimensional palladium diselenide using heterophase grain boundaries,” *Nat. Electron.*, vol. 4, no. 5, pp. 348–356, 2021, doi: 10.1038/s41928-021-00573-1.

[8] S. Choi *et al.*, “SiGe epitaxial memory for neuromorphic computing with reproducible high performance based on engineered dislocations,” *Nat. Mater.*, vol. 17, no. 4, pp. 335–340, 2018, doi: 10.1038/s41563-017-0001-5.

[9] S. G. Kim *et al.*, “Dual-Phase All-Inorganic Cesium Halide Perovskites for Conducting-Bridge Memory-Based Artificial Synapses,” *Adv. Funct. Mater.*, vol. 29, no. 49, p. 1906686, 2019, doi: 10.1002/adfm.201906686.

[10] Q. Wang *et al.*, “Phase Change Random Access Memory for Neuro-Inspired Computing,” *Adv. Electron. Mater.*, vol. 7, no. 6, p. 2001241, 2021, doi: 10.1002/aelm.202001241.

[11] P. Rzeszut, J. Chęciński, I. Brzozowski, S. Ziętek, W. Skowroński, and T. Stobiecki, “Multi-state MRAM cells for hardware neuromorphic computing,” *Sci. Rep.*, vol. 12, no. 1, p. 7178, 2022, doi: 10.1038/s41598-022-11199-4.

[12] C. Sen Yang *et al.*, “All-Solid-State Synaptic Transistor with Ultralow Conductance for Neuromorphic Computing,” *Adv. Funct. Mater.*, vol. 28, no. 42, p. 1804170, 2018, doi: 10.1002/adfm.201804170.

[13] M. P. Sah, C. Yang, H. Kim, B. Muthuswamy, J. Jevtic, and L. Chua, “A generic model of memristors with parasitic components,” *IEEE Trans. Circuits Syst. I Regul. Pap.*, vol. 62, no. 3, pp. 891–898, 2015, doi: 10.1109/TCSI.2014.2373674.

[14] S. Oh *et al.*, “Electrolyte-Gated Vertical Synapse Array based on Van Der Waals Heterostructure for Parallel Computing,” *Adv. Sci.*, vol. 9, no. 6, p. 2103808, 2022, doi: https://doi.org/10.1002/advs.202103808.

[15] L. Shi, G. Zheng, B. Tian, B. Dkhil, and C. Duan, “Research progress on solutions to the sneak path issue in memristor crossbar arrays,” *Nanoscale Adv.*, vol. 2, no. 5, pp. 1811–1827, 2020, doi: 10.1039/D0NA00100G.

[16] S. Dai *et al.*, “Recent Advances in Transistor-Based Artificial Synapses,” *Adv. Funct. Mater.*, vol. 29, no. 42, p. 1903700, 2019, doi: 10.1002/adfm.201903700.

[17] E. J. Fuller *et al.*, “Li-Ion Synaptic Transistor for Low Power Analog Computing,” *Adv. Mater.*, vol. 29, no. 4, p. 1604310, 2017, doi: 10.1002/adma.201604310.

[18] L. Danial *et al.*, “Two-terminal floating-gate transistors with a low-power memristive operation mode for analogue neuromorphic computing,” *Nat. Electron.*, vol. 2, no. 12, pp. 596–605, 2019, doi: 10.1038/s41928-019-0331-1.

[19] L. Danial, V. Gupta, E. Pikhay, Y. Roizin, and S. Kvatinsky, “Modeling a Floating-Gate Memristive Device for Computer Aided Design of Neuromorphic Computing,” in *2020 Design, Automation & Test in Europe Conference & Exhibition (DATE)*, 2020, pp. 472–477. doi: 10.23919/DATE48585.2020.9116354.

[20] E. J. Fuller *et al.*, “Parallel programming of an ionic floating-gate memory

array for scalable neuromorphic computing," *Science.*, vol. 364, no. 6440, pp. 570–574, May 2019, doi: 10.1126/science.aaw5581.

[21] I.-J. Kim and J.-S. Lee, "Ferroelectric Transistors for Memory and Neuromorphic Device Applications," *Adv. Mater.*, vol. 35, no. 22, p. 2206864, Jun. 2023, doi: https://doi.org/10.1002/adma.202206864.

[22] S. Wang *et al.*, "Two-dimensional ferroelectric channel transistors integrating ultra-fast memory and neural computing," *Nat. Commun.*, vol. 12, no. 1, p. 53, 2021, doi: 10.1038/s41467-020-20257-2.

[23] R. D. Nikam, J. Lee, K. Lee, and H. Hwang, "Exploring the Cutting-Edge Frontiers of Electrochemical Random Access Memories (ECRAMs) for Neuromorphic Computing: Revolutionary Advances in Material-to-Device Engineering," *Small*, vol. 19, no. 40, p. 2302593, Oct. 2023, doi: https://doi.org/10.1002/smll.202302593.

[24] V. K. Sangwan and M. C. Hersam, "Neuromorphic nanoelectronic materials," *Nat. Nanotechnol.*, vol. 15, no. 7, pp. 517–528, 2020, doi: 10.1038/s41565-020-0647-z.

[25] H. Ling, D. A. Koutsouras, S. Kazemzadeh, Y. Van De Burgt, F. Yan, and P. Gkoupidenis, "Electrolyte-gated transistors for synaptic electronics, neuromorphic computing, and adaptable biointerfacing," *Appl. Phys. Rev.*, vol. 7, no. 1, 2020, doi: 10.1063/1.5122249.

[26] X. Deng *et al.*, "A Flexible Mott Synaptic Transistor for Nociceptor Simulation and Neuromorphic Computing," *Adv. Funct. Mater.*, vol. 31, no. 23, p. 2101099, 2021, doi: 10.1002/adfm.202101099.

[27] Y. Zhu, G. Liu, Z. Xin, C. Fu, Q. Wan, and F. Shan, "Solution-Processed, Electrolyte-Gated In2O3 Flexible Synaptic Transistors for Brain-Inspired Neuromorphic Applications," *ACS Appl. Mater. Interfaces*, vol. 12, no. 1, pp. 1061–1068, 2020, doi: 10.1021/acsami.9b18605.

[28] R. D. Nikam, M. Kwak, J. Lee, K. G. Rajput, and H. Hwang, "Controlled Ionic Tunneling in Lithium Nanoionic Synaptic Transistor through Atomically Thin Graphene Layer for Neuromorphic Computing," *Adv. Electron. Mater.*, vol. 6, no. 2, p. 1901100, 2020, doi: 10.1002/aelm.201901100.

[29] R. D. Nikam *et al.*, “Ionic Sieving Through One-Atom-Thick 2D Material Enables Analog Nonvolatile Memory for Neuromorphic Computing,” *Small*, vol. 17, no. 44, p. 2103543, Nov. 2021, doi: https://doi.org/10.1002/smll.202103543.

[30] R. D. Nikam, M. Kwak, J. Lee, K. G. Rajput, W. Banerjee, and H. Hwang, “Near ideal synaptic functionalities in Li ion synaptic transistor using Li3POxSex electrolyte with high ionic conductivity,” *Sci. Rep.*, vol. 9, no. 1, p. 18883, 2019, doi: 10.1038/s41598-019-55310-8.

[31] E. J. Fuller *et al.*, “Li-Ion Synaptic Transistor for Low Power Analog Computing,” *Adv. Mater.*, vol. 29, no. 4, pp. 1–8, 2017, doi: 10.1002/adma.201604310.

[32] J. H. Baek *et al.*, “Two-Terminal Lithium-Mediated Artificial Synapses with Enhanced Weight Modulation for Feasible Hardware Neural Networks,” *Nano-Micro Lett.*, vol. 15, no. 1, p. 69, 2023, doi: 10.1007/s40820-023-01035-3.

[33] Y. Zhu, G. Liu, Z. Xin, C. Fu, Q. Wan, and F. Shan, “Solution-Processed, Electrolyte-Gated In2O3 Flexible Synaptic Transistors for Brain-Inspired Neuromorphic Applications,” *ACS Appl. Mater. Interfaces*, vol. 12, no. 1, pp. 1061–1068, 2020, doi: 10.1021/acsami.9b18605.

[34] Y. Park, M.-K. Kim, and J.-S. Lee, “Ion-gating synaptic transistors with long-term synaptic weight modulation,” *J. Mater. Chem. C*, vol. 9, no. 16, pp. 5396–5402, 2021, doi: 10.1039/D1TC00048A.

[35] H. Wei *et al.*, “Flexible electro-optical neuromorphic transistors with tunable synaptic plasticity and nociceptive behavior,” *Nano Energy*, vol. 81, no. December 2020, 2021, doi: 10.1016/j.nanoen.2020.105648.

[36] J. Wu, “Understanding the Electric Double-Layer Structure, Capacitance, and Charging Dynamics,” *Chem. Rev.*, vol. 122, no. 12, pp. 10821–10859, Jun. 2022, doi: 10.1021/acs.chemrev.2c00097.

[37] R. Funari, A. Matsumoto, J. R. de Bruyn, and A. Q. Shen, “Rheology of the Electric Double Layer in Electrolyte Solutions,” *Anal. Chem.*, vol. 92, no. 12, pp. 8244–8253, Jun. 2020, doi: 10.1021/acs.analchem.0c00475.

[38] T. Shirai, S. Yamauchi, H. Kikuchi, H. Fukumoto, H. Tsukada, and T. Agou,

"Synthesis, characterization, and formation of self-assembled monolayers of a phosphonic acid bearing a vinylene-bridged fluoroalkyl chain," *Appl. Surf. Sci.*, vol. 577, p. 151959, 2022, doi: https://doi.org/10.1016/j.apsusc.2021.151959.

[39] O. Zenasni, A. C. Jamison, and T. R. Lee, "The impact of fluorination on the structure and properties of self-assembled monolayer films," *Soft Matter*, vol. 9, no. 28, pp. 6356–6370, 2013, doi: 10.1039/C3SM00054K.

[40] L. Jiang *et al.*, "Low-Temperature and Solution-Processable Zinc Oxide Transistors for Transparent Electronics," *ACS Omega*, vol. 2, no. 12, pp. 8990–8996, Dec. 2017, doi: 10.1021/acsomega.7b01420.

[41] C. Im *et al.*, "Analysis of Interface Phenomena for High-Performance Dual-Stacked Oxide Thin-Film Transistors via Equivalent Circuit Modeling," *ACS Appl. Mater. Interfaces*, vol. 13, no. 43, pp. 51266–51278, Nov. 2021, doi: 10.1021/acsami.1c17351.

[42] S.-E. Lee *et al.*, "The effect of surface energy characterized functional groups of self-assembled monolayers for enhancing the electrical stability of oxide semiconductor thin film transistors," *Nanotechnology*, vol. 31, no. 47, p. 475203, 2020, doi: 10.1088/1361-6528/abad5e.

[43] L. Suo *et al.*, "Advanced High-Voltage Aqueous Lithium-Ion Battery Enabled by 'Water-in-Bisalt' Electrolyte," *Angew. Chemie Int. Ed.*, vol. 55, no. 25, pp. 7136–7141, Jun. 2016, doi: https://doi.org/10.1002/anie.201602397.

[44] E. G. Lee *et al.*, "Superconcentrated aqueous electrolyte and UV curable polymer composite as gate dielectric for high-performance oxide semiconductor thin-film transistors," *Appl. Phys. Lett.*, vol. 114, no. 17, p. 172903, Apr. 2019, doi: 10.1063/1.5093741.

[45] L. Suo *et al.*, "Advanced High-Voltage Aqueous Lithium-Ion Battery Enabled by 'Water-in-Bisalt' Electrolyte," *Angew. Chemie - Int. Ed.*, vol. 55, no. 25, pp. 7136–7141, 2016, doi: 10.1002/anie.201602397.

[46] E. G. Lee *et al.*, "Superconcentrated aqueous electrolyte and UV curable polymer composite as gate dielectric for high-performance oxide semiconductor thin-film transistors," *Appl. Phys. Lett.*, vol. 114, no. 17, p.

172903, 2019, doi: 10.1063/1.5093741.

[47] J. Park, S. Song, Y. Yang, S. H. Kwon, E. Sim, and Y. S. Kim, “Identification of Droplet-Flow-Induced Electric Energy on Electrolyte-Insulator-Semiconductor Structure,” *J. Am. Chem. Soc.*, vol. 139, no. 32, pp. 10968–10971, 2017, doi: 10.1021/jacs.7b05030.

[48] X. Li *et al.*, “Water Splitting: From Electrode to Green Energy System,” *Nano-Micro Lett.*, vol. 12, no. 1, pp. 1–29, 2020, doi: 10.1007/s40820-020-00469-3.

[49] H. J. Na *et al.*, “Nanometer-Thick Cs2SnI6Perovskite-Polyethylene Glycol Dimethacrylate Composite Films for Highly Stable Broad-Band Photodetectors,” *ACS Appl. Nano Mater.*, vol. 4, no. 5, pp. 5309–5318, 2021, doi: 10.1021/acsanm.1c00660.

[50] N.-K. Cho, H.-J. Na, J. Yoo, and Y. S. Kim, “Long-term stability in γ-CsPbI3 perovskite via an ultraviolet-curable polymer network,” *Commun. Mater.*, vol. 2, no. 1, pp. 1–8, 2021, doi: 10.1038/s43246-021-00134-1.

[51] B. W. Yao *et al.*, “Non-Volatile Electrolyte-Gated Transistors Based on Graphdiyne/MoS2 with Robust Stability for Low-Power Neuromorphic Computing and Logic-In-Memory,” *Adv. Funct. Mater.*, vol. 31, no. 25, p. 2100069, 2021, doi: 10.1002/adfm.202100069.

[52] A. Ehrl, J. Landesfeind, W. A. Wall, and H. A. Gasteiger, “Determination of Transport Parameters in Liquid Binary Lithium Ion Battery Electrolytes,” *J. Electrochem. Soc.*, vol. 164, no. 4, pp. A826–A836, 2017, doi: 10.1149/2.1131704jes.

[53] L. Q. Zhu, C. J. Wan, L. Q. Guo, Y. Shi, and Q. Wan, “Artificial synapse network on inorganic proton conductor for neuromorphic systems,” *Nat. Commun.*, vol. 5, 2014, doi: 10.1038/ncomms4158.

[54] W. C. Abraham, O. D. Jones, and D. L. Glanzman, “Is plasticity of synapses the mechanism of long-term memory storage?,” *npj Sci. Learn.*, vol. 4, no. 1, p. 9, 2019, doi: 10.1038/s41539-019-0048-y.

[55] D. G. Seo *et al.*, “Versatile neuromorphic electronics by modulating synaptic decay of single organic synaptic transistor: From artificial neural networks to neuro-prosthetics,” *Nano Energy*, vol. 65, no. June, p. 104035, 2019, doi:

10.1016/j.nanoen.2019.104035.

[56] K. Xu, M. M. Islam, D. Guzman, A. C. Seabaugh, A. Strachan, and S. K. Fullerton-Shirey, “Pulse Dynamics of Electric Double Layer Formation on All-Solid-State Graphene Field-Effect Transistors,” *ACS Appl. Mater. Interfaces,* vol. 10, no. 49, pp. 43166–43176, 2018, doi: 10.1021/acsami.8b13649.

[57] J. Li *et al.*, “Flexible transparent InZnO synapse transistor based on Li1.3Al0.3Ti0.7(PO4)3/polyvinyl pyrrolidone nanocomposites electrolyte film for neuromorphic computing,” *Mater. Today Phys.*, vol. 15, p. 100264, 2020, doi: https://doi.org/10.1016/j.mtphys.2020.100264.

[58] X. Yao *et al.*, “Protonic solid-state electrochemical synapse for physical neural networks,” *Nat. Commun.*, vol. 11, no. 1, p. 3134, 2020, doi: 10.1038/s41467-020-16866-6.

[59] R. D. Nikam, M. Kwak, J. Lee, K. G. Rajput, W. Banerjee, and H. Hwang, “Near ideal synaptic functionalities in Li ion synaptic transistor using Li3POxSex electrolyte with high ionic conductivity,” *Sci. Rep.*, vol. 9, no. 1, pp. 1–11, 2019, doi: 10.1038/s41598-019-55310-8.

[60] K. C. Lee *et al.*, “Inverse paired-pulse facilitation in neuroplasticity based on interface-boosted charge trapping layered electronics,” *Nano Energy*, vol. 77, no. June, p. 105258, 2020, doi: 10.1016/j.nanoen.2020.105258.

[61] R. S. Zucker and W. G. Regehr, “Short-term synaptic plasticity,” *Annu. Rev. Physiol.*, vol. 64, pp. 355–405, 2002, doi: 10.1146/annurev.physiol.64.092501.114547.

[62] Y. Li *et al.*, “Oxide-Based Electrolyte-Gated Transistors for Spatiotemporal Information Processing,” *Adv. Mater.*, vol. 32, no. 47, p. 2003018, 2020, doi: 10.1002/adma.202003018.

[63] D. M. Alloway *et al.*, “Interface dipoles arising from self-assembled monolayers on gold: UV-photoemission studies of alkanethiols and partially fluorinated alkanethiols,” *J. Phys. Chem. B*, vol. 107, no. 42, pp. 11690–11699, 2003, doi: 10.1021/jp034665+.

[64] H. Wang, Y. Wu, C. Cong, J. Shang, and T. Yu, “Hysteresis of electronic transport in graphene transistors,” *ACS Nano*, vol. 4, no. 12, pp. 7221–7228,

2010, doi: 10.1021/nn101950n.

[65] D. O'hagan, "Understanding organofluorine chemistry. An introduction to the C–F bond," *Chem. Soc. Rev.*, vol. 37, no. 2, pp. 308–319, 2008, doi: 10.1039/b711844a.

[66] H. Takemura, N. Kon, M. Yasutake, S. Nakashima, T. Shinmyozu, and T. Inazu, "The C-F cation interaction: An ammonium complex of a hexafluoro macrocyclic cage compound," *Chem. Eur. J.*, vol. 6, no. 13, p. 2334, 2000, doi: 10.1002/1521-3765(20000703)6:13<2334::AID-CHEM2334>3.0.CO;2-A.

[67] H. Takemura, N. Kon, M. Yasutake, H. Kariyazono, T. Shinmyozu, and T. Inazu, "A potassium complex of a fluorine-containing macrocyclic cage compound: Interactions between fluorine atoms and metal ions," *Angew. Chemie - Int. Ed.*, vol. 38, no. 7, pp. 959–961, 1999, doi: 10.1002/(SICI)1521-3773(19990401)38:7<959::AID-ANIE959>3.0.CO;2-8.

[68] M. G. Park, G. K. Sung, N. E. Sung, J. H. Kim, and C. M. Park, "Partially reversible Li2O formation in ZnO: A critical finding supporting realization of highly reversible metal oxide electrodes," *J. Power Sources*, vol. 328, pp. 607–614, 2016, doi: 10.1016/j.jpowsour.2016.08.053.

[69] S. G. Yoon *et al.*, "Probing an Interfacial Ionic Pairing-Induced Molecular Dipole Effect in Ionovoltaic System," *Small Methods*, vol. 5, no. 7, pp. 1–7, 2021, doi: 10.1002/smtd.202100323.

[70] J. Han, S. G. Yoon, W. H. Lee, H. Jin, Y. H. Cho, and Y. S. Kim, "Ionic Diffusion-Driven Ionovoltaic Transducer for Probing Ion-Molecular Interactions at Solid–Liquid Interface," *Adv. Sci.*, vol. 9, no. 1, p. 2103038, Jan. 2022, doi: https://doi.org/10.1002/advs.202103038.

[71] T. Cremer *et al.*, "Towards a Molecular Understanding of Cation–Anion Interactions—Probing the Electronic Structure of Imidazolium Ionic Liquids by NMR Spectroscopy, X-ray Photoelectron Spectroscopy and Theoretical Calculations," *Chem. – A Eur. J.*, vol. 16, no. 30, pp. 9018–9033, Aug. 2010, doi: https://doi.org/10.1002/chem.201001032.

[72] T. M. W. J. Bandara *et al.*, "Effect of the alkaline cation size on the conductivity in gel polymer electrolytes and their influence on photo

electrochemical solar cells," *Phys. Chem. Chem. Phys.*, vol. 18, no. 16, pp. 10873–10881, 2016, doi: 10.1039/c6cp00013d.

[73] Y. Charles-Blin, H. Todoki, N. Zettsu, and K. Teshima, "Molecular gate effects observed in fluoroalkylsilane self-assembled monolayers grafted on LiNi0.5Mn1.5O4cathodes: An application to efficient ion-exchange reactions," *Mater. Adv.*, vol. 2, no. 16, pp. 5406–5414, 2021, doi: 10.1039/d1ma00426c.

[74] H. Dietrich, S. Scheiner, L. Portilla, D. Zahn, and M. Halik, "Improving the Performance of Organic Thin-Film Transistors by Ion Doping of Ethylene-Glycol-Based Self-Assembled Monolayer Hybrid Dielectrics," *Adv. Mater.*, vol. 27, no. 48, p. 8023, 2015, doi: 10.1002/adma.201503911.

[75] J. Park *et al.*, "Ion Specificity on Electric Energy Generated by Flowing Water Droplets," *Angew. Chemie - Int. Ed.*, vol. 57, no. 8, pp. 2091–2095, 2018, doi: 10.1002/anie.201711505.

[76] Y. Choi, S. Oh, C. Qian, J. H. Park, and J. H. Cho, "Vertical organic synapse expandable to 3D crossbar array," *Nat. Commun.*, vol. 11, no. 1, pp. 1–9, 2020, doi: 10.1038/s41467-020-17850-w.

[77] P. Y. Chen, X. Peng, and S. Yu, "NeuroSim: A circuit-level macro model for benchmarking neuro-inspired architectures in online learning," *IEEE Trans. Comput. Des. Integr. Circuits Syst.*, vol. 37, no. 12, pp. 3067–3080, 2018, doi: 10.1109/TCAD.2018.2789723.

[78] Y. Park, M. K. Kim, and J. S. Lee, "Ion-gating synaptic transistors with long-term synaptic weight modulation," *J. Mater. Chem. C*, vol. 9, no. 16, pp. 5396–5402, 2021, doi: 10.1039/d1tc00048a.

[79] S. Yu, "Neuro-Inspired Computing with Emerging Nonvolatile Memorys," *Proc. IEEE*, vol. 106, no. 2, pp. 260–285, 2018, doi: 10.1109/JPROC.2018.2790840.

[80] H. Yeon *et al.*, "Alloying conducting channels for reliable neuromorphic computing," *Nat. Nanotechnol.*, vol. 15, no. 7, pp. 574–579, 2020, doi: 10.1038/s41565-020-0694-5.

[81] X. Wan *et al.*, "Thermal Stability of Phosphonic Acid Self-Assembled Monolayers on Alumina Substrates," *J. Phys. Chem. C*, vol. 124, no. 4, pp.

2531–2542, Jan. 2020, doi: 10.1021/acs.jpcc.9b10628.

[82] R. Quiñones *et al.*, “Study of Perfluorophosphonic Acid Surface Modifications on Zinc Oxide Nanoparticles,” *Materials*, vol. 10, no. 12. 2017. doi: 10.3390/ma10121363.

[83] Y. Li *et al.*, “Oxide-Based Electrolyte-Gated Transistors for Spatiotemporal Information Processing,” *Adv. Mater.*, vol. 32, no. 47, p. 2003018, Nov. 2020, doi: https://doi.org/10.1002/adma.202003018.

[84] R. Acharya, B. Peng, P. K. L. Chan, G. Schmitz, and H. Klauk, “Achieving Ultralow Turn-On Voltages in Organic Thin-Film Transistors: Investigating Fluoroalkylphosphonic Acid Self-Assembled Monolayer Hybrid Dielectrics,” *ACS Appl. Mater. Interfaces*, vol. 11, no. 30, pp. 27104–27111, Jul. 2019, doi: 10.1021/acsami.9b04361.

[85] M. S. Góes, H. Rahman, J. Ryall, J. J. Davis, and P. R. Bueno, “A Dielectric Model of Self-Assembled Monolayer Interfaces by Capacitive Spectroscopy,” *Langmuir*, vol. 28, no. 25, pp. 9689–9699, Jun. 2012, doi: 10.1021/la301281y.

[86] M. Jin *et al.*, “Interfacial Ion-Trapping Electrolyte-Gated Transistors for High-Fidelity Neuromorphic Computing,” *Adv. Funct. Mater.*, vol. 32, no. 24, p. 2201048, Jun. 2022, doi: https://doi.org/10.1002/adfm.202201048.

[87] L. Q. Zhu, C. J. Wan, L. Q. Guo, Y. Shi, and Q. Wan, “Artificial synapse network on inorganic proton conductor for neuromorphic systems,” *Nat. Commun.*, vol. 5, no. 1, p. 3158, 2014, doi: 10.1038/ncomms4158.

[88] M. Onen *et al.*, “Nanosecond protonic programmable resistors for analog deep learning,” *Science.*, vol. 377, no. 6605, pp. 539–543, Jul. 2022, doi: 10.1126/science.abp8064.

[89] M.-K. Kim, I.-J. Kim, and J.-S. Lee, “CMOS-compatible compute-in-memory accelerators based on integrated ferroelectric synaptic arrays for convolution neural networks,” *Sci. Adv.*, vol. 8, no. 14, p. eabm8537, Oct. 2023, doi: 10.1126/sciadv.abm8537.

[90] P.-Y. Chen, X. Peng, and S. Yu, “NeuroSim: A Circuit-Level Macro Model for Benchmarking Neuro-Inspired Architectures in Online Learning,” *IEEE Trans. Comput. Des. Integr. Circuits Syst.*, vol. 37, no. 12, pp. 3067–3080, 2018, doi: 10.1109/TCAD.2018.2789723.

[91] R. Yi, Y. Mao, Y. Shen, and L. Chen, “Self-Assembled Monolayers for Batteries,” *J. Am. Chem. Soc.*, vol. 143, no. 33, pp. 12897–12912, Aug. 2021, doi: 10.1021/jacs.1c04416.

[92] M. A. Brown, A. Goel, and Z. Abbas, “Effect of Electrolyte Concentration on the Stern Layer Thickness at a Charged Interface,” *Angew. Chemie Int. Ed.*, vol. 55, no. 11, pp. 3790–3794, Mar. 2016, doi: https://doi.org/10.1002/anie.201512025.

[93] J. Park *et al.*, “Ion Specificity on Electric Energy Generated by Flowing Water Droplets,” *Angew. Chemie Int. Ed.*, vol. 57, no. 8, pp. 2091–2095, Feb. 2018, doi: https://doi.org/10.1002/anie.201711505.

[94] P. Giannozzi *et al.*, “QUANTUM ESPRESSO: a modular and open-source software project for quantum simulations of materials,” *J. Phys. Condens. Matter*, vol. 21, no. 39, p. 395502, 2009, doi: 10.1088/0953-8984/21/39/395502.

[95] C.-J. Chu *et al.*, “Improving Nanowire Sensing Capability by Electrical Field Alignment of Surface Probing Molecules,” *Nano Lett.*, vol. 13, no. 6, pp. 2564–2569, Jun. 2013, doi: 10.1021/nl400645j.

[96] D. Koretomo, S. Hamada, Y. Magari, and M. Furuta, “Quantum Confinement Effect in Amorphous In–Ga–Zn–O Heterojunction Channels for Thin-Film Transistors,” *Materials*, vol. 13, no. 8. 2020. doi: 10.3390/ma13081935.

[97] H. Takemura, S. Nakashima, N. Kon, M. Yasutake, T. Shinmyozu, and T. Inazu, “A Study of C−F⋯M+ Interaction: Metal Complexes of Fluorine-Containing Cage Compounds,” *J. Am. Chem. Soc.*, vol. 123, no. 38, pp. 9293–9298, Sep. 2001, doi: 10.1021/ja0043587.

[98] F. Rao, Z. Wang, B. Xu, L. Chen, and C. Ouyang, “First-Principles Study of Lithium and Sodium Atoms Intercalation in Fluorinated Graphite,” *Engineering*, vol. 1, no. 2, pp. 243–246, 2015, doi: https://doi.org/10.15302/J-ENG-2015039.

[99] W. Yu, Z. Yu, Y. Cui, and Z. Bao, “Degradation and Speciation of Li Salts during XPS Analysis for Battery Research,” *ACS Energy Lett.*, vol. 7, no. 10, pp. 3270–3275, Oct. 2022, doi: 10.1021/acsenergylett.2c01587.

[100] M. Jin *et al.*, “Ferroelectrically modulated ion dynamics in Li+ electrolyte-

gated transistors for neuromorphic computing," *Appl. Phys. Rev.*, vol. 10, no. 1, p. 11407, Feb. 2023, doi: 10.1063/5.0130742.

[101] X. Peng, S. Huang, Y. Luo, X. Sun, and S. Yu, "DNN+NeuroSim: An End-to-End Benchmarking Framework for Compute-in-Memory Accelerators with Versatile Device Technologies," in *2019 IEEE International Electron Devices Meeting (IEDM)*, 2019, pp. 32.5.1-32.5.4. doi: 10.1109/IEDM19573.2019.8993491.

[102] J.-M. Yang *et al.*, "Mixed-Dimensional Formamidinium Bismuth Iodides Featuring In-Situ Formed Type-I Band Structure for Convolution Neural Networks," *Adv. Sci.*, vol. 9, no. 14, p. 2200168, May 2022, doi: https://doi.org/10.1002/advs.202200168.

[103] R. D. Nikam, M. Kwak, J. Lee, K. G. Rajput, and H. Hwang, "Controlled Ionic Tunneling in Lithium Nanoionic Synaptic Transistor through Atomically Thin Graphene Layer for Neuromorphic Computing," *Adv. Electron. Mater.*, vol. 6, no. 2, p. 1901100, Feb. 2020, doi: https://doi.org/10.1002/aelm.201901100.

[104] R. D. Nikam *et al.*, "Ionic Sieving Through One-Atom-Thick 2D Material Enables Analog Nonvolatile Memory for Neuromorphic Computing," *Small*, vol. 17, no. 44, p. 2103543, Nov. 2021, doi: https://doi.org/10.1002/smll.202103543.

[105] K. Lee *et al.*, "Improved synaptic functionalities of Li-based nano-ionic synaptic transistor with ultralow conductance enabled by Al_2O_3 barrier layer," *Nanotechnology*, vol. 32, no. 27, p. 275201, Jul. 2021, doi: 10.1088/1361-6528/abf071.

[106] H. Wei *et al.*, "Flexible electro-optical neuromorphic transistors with tunable synaptic plasticity and nociceptive behavior," *Nano Energy*, vol. 81, p. 105648, 2021, doi: https://doi.org/10.1016/j.nanoen.2020.105648.

[107] C. Hwang *et al.*, "A Three-Dimensional Nano-web Scaffold of Ferroelectric Beta-PVDF Fibers for Lithium Metal Plating and Stripping," *ACS Appl. Mater. Interfaces*, vol. 12, no. 26, pp. 29235–29241, 2020, doi: 10.1021/acsami.0c05065.

[108] L. Wang *et al.*, "In-situ visualization of the space-charge-layer effect on

interfacial lithium-ion transport in all-solid-state batteries," *Nat. Commun.*, vol. 11, no. 1, p. 5889, 2020, doi: 10.1038/s41467-020-19726-5.

[109] Y. Sun, N. He, Y. Wang, Q. Yuan, and D. Wen, "Multilevel memory and artificial synaptic plasticity in P(VDF-TrFE)-based ferroelectric field effect transistors," *Nano Energy*, vol. 98, no. April, p. 107252, 2022, doi: 10.1016/j.nanoen.2022.107252.

[110] K. Müller, D. Mandal, K. Henkel, I. Paloumpa, and D. Schmeisser, "Ferroelectric properties of spin-coated ultrathin (down to 10 nm) copolymer films," *Appl. Phys. Lett.*, vol. 93, no. 11, p. 112901, Sep. 2008, doi: 10.1063/1.2975159.

[111] X. Zhang, C. Liu, L. Li, H. Yuan, and H. Xu, "Switching dynamics enhancement in P(VDF-TrFE) copolymer ultrathin films with symmetric organic film electrodes," *Org. Electron.*, vol. 66, no. December 2018, pp. 81–85, 2019, doi: 10.1016/j.orgel.2018.12.017.

[112] E. G. Lee *et al.*, "Superconcentrated aqueous electrolyte and UV curable polymer composite as gate dielectric for high-performance oxide semiconductor thin-film transistors," *Appl. Phys. Lett.*, vol. 114, no. 17, p. 172903, Apr. 2019, doi: 10.1063/1.5093741.

[113] Z. Hu, M. Tian, B. Nysten, and A. M. Jonas, "Regular arrays of highly ordered ferroelectric polymer nanostructures for non-volatile low-voltage memories," *Nat. Mater.*, vol. 8, no. 1, pp. 62–67, 2009, doi: 10.1038/nmat2339.

[114] S. Kim *et al.*, "Ferroelectric polymer-based artificial synapse for neuromorphic computing," *Nanoscale Horizons*, vol. 6, no. 2, pp. 139–147, 2021, doi: 10.1039/d0nh00559b.

[115] J.-R. Duclère *et al.*, "Properties of Li-, P- and N-doped ZnO thin films prepared by pulsed laser deposition," *Superlattices Microstruct.*, vol. 38, no. 4, pp. 397–405, 2005, doi: https://doi.org/10.1016/j.spmi.2005.08.011.

[116] K.-H. Lim, K. Kim, S. Kim, S. Y. Park, H. Kim, and Y. S. Kim, "UV–Visible Spectroscopic Analysis of Electrical Properties in Alkali Metal-Doped Amorphous Zinc Tin Oxide Thin-Film Transistors," *Adv. Mater.*, vol. 25, no. 21, pp. 2994–3000, Jun. 2013, doi: https://doi.org/10.1002/adma.201204236.

[117] F. Huang, S. Zhu, F. Wang, T. Li, and W. Zheng, “Can We Transform Any Insulators into Semiconductors? Theory, Strategy, and Example in ZnO,” *Matter,* vol. 2, no. 5, pp. 1091–1105, 2020, doi: 10.1016/j.matt.2020.03.002.

[118] J. Luo, C.-C. Fang, and N.-L. Wu, “High Polarity Poly(vinylidene difluoride) Thin Coating for Dendrite-Free and High-Performance Lithium Metal Anodes,” *Adv. Energy Mater.*, vol. 8, no. 2, p. 1701482, Jan. 2018, doi: https://doi.org/10.1002/aenm.201701482.

[119] B.-W. Yao *et al.*, “Non-Volatile Electrolyte-Gated Transistors Based on Graphdiyne/MoS2 with Robust Stability for Low-Power Neuromorphic Computing and Logic-In-Memory,” *Adv. Funct. Mater.*, vol. 31, no. 25, p. 2100069, Jun. 2021, doi: https://doi.org/10.1002/adfm.202100069.

[120] K. Lee *et al.*, “Improved synaptic functionalities of Li-based nano-ionic synaptic transistor with ultralow conductance enabled by Al_2O_3 barrier layer,” *Nanotechnology,* vol. 32, no. 27, p. 275201, 2021, doi: 10.1088/1361-6528/abf071.

[121] C.-S. Yang *et al.*, “All-Solid-State Synaptic Transistor with Ultralow Conductance for Neuromorphic Computing,” *Adv. Funct. Mater.*, vol. 28, no. 42, p. 1804170, Oct. 2018, doi: https://doi.org/10.1002/adfm.201804170.

[122] W. Choi, H.-C. Shin, J. M. Kim, J.-Y. Choi, and W.-S. Yoon, “Modeling and Applications of Electrochemical Impedance Spectroscopy (EIS) for Lithium-ion Batteries,” *J. Electrochem. Sci. Technol*, vol. 11, no. 1, pp. 1–13, Feb. 2020, doi: 10.33961/jecst.2019.00528.

[123] M. Kundu, C. M. Costa, J. Dias, A. Maceiras, J. L. Vilas, and S. Lanceros-Méndez, “On the Relevance of the Polar β-Phase of Poly(vinylidene fluoride) for High Performance Lithium-Ion Battery Separators,” *J. Phys. Chem. C*, vol. 121, no. 47, pp. 26216–26225, 2017, doi: 10.1021/acs.jpcc.7b09227.

[124] W. J. Song *et al.*, “Significance of ferroelectric polarization in poly (vinylidene difluoride) binder for high-rate Li-ion diffusion,” *Nano Energy*, vol. 32, no. December 2016, pp. 255–262, 2017, doi: 10.1016/j.nanoen.2016.12.037.

[125] A. C. Choi *et al.*, “Polarization Mechanisms in P(VDF-TrFE) Ferroelectric Thin Films,” *Phys. status solidi – Rapid Res. Lett.*, vol. 12, no. 10, p. 1800340,

Oct. 2018, doi: https://doi.org/10.1002/pssr.201800340.

[126] X. Niu, B. Tian, Q. Zhu, B. Dkhil, and C. Duan, “Ferroelectric polymers for neuromorphic computing,” *Appl. Phys. Rev.*, vol. 9, no. 2, p. 21309, May 2022, doi: 10.1063/5.0073085.

[127] X. Deng *et al.*, “A Flexible Mott Synaptic Transistor for Nociceptor Simulation and Neuromorphic Computing,” *Adv. Funct. Mater.*, vol. 31, no. 23, p. 2101099, Jun. 2021, doi: https://doi.org/10.1002/adfm.202101099.

[128] J. C. Dias *et al.*, “Improved response of ionic liquid-based bending actuators by tailored interaction with the polar fluorinated polymer matrix,” *Electrochim. Acta*, vol. 296, pp. 598–607, 2019, doi: 10.1016/j.electacta.2018.11.049.

[129] S. Kim *et al.*, “Artificial stimulus-response system capable of conscious response,” *Sci. Adv.*, vol. 7, no. 15, p. eabe3996, Nov. 2022, doi: 10.1126/sciadv.abe3996.

[130] L. Liu *et al.*, “Stretchable Neuromorphic Transistor That Combines Multisensing and Information Processing for Epidermal Gesture Recognition,” *ACS Nano*, vol. 16, no. 2, pp. 2282–2291, Feb. 2022, doi: 10.1021/acsnano.1c08482.

[131] Y. Li *et al.*, “Oxide-Based Electrolyte-Gated Transistors for Spatiotemporal Information Processing,” *Adv. Mater.*, vol. 32, no. 47, p. 2003018, Nov. 2020, doi: https://doi.org/10.1002/adma.202003018.

[132] T. P. Xiao, C. H. Bennett, B. Feinberg, S. Agarwal, and M. J. Marinella, “Analog architectures for neural network acceleration based on non-volatile memory,” *Appl. Phys. Rev.*, vol. 7, no. 3, p. 031301, Jul. 2020, doi: 10.1063/1.5143815.

[133] P.-Y. Chen, X. Peng, and S. Yu, “NeuroSim+: An integrated device-to-algorithm framework for benchmarking synaptic devices and array architectures,” in *2017 IEEE International Electron Devices Meeting (IEDM)*, 2017, pp. 6.1.1-6.1.4. doi: 10.1109/IEDM.2017.8268337.

List of publications

First author

[1] H. Lee *et al.*, “Implementation of Synaptic Device Using Ultraviolet Ozone Treated Water-in-Bisalt/Polymer Electrolyte-Gated Transistor,” *Adv. Funct. Mater.*, vol. 32, no. 15, p. 2110591, Apr. 2022, doi: https://doi.org/10.1002/adfm.202110591.

[2] M. Jin *et al.*, “Interfacial Ion-Trapping Electrolyte-Gated Transistors for High-Fidelity Neuromorphic Computing,” *Adv. Funct. Mater.*, vol. 32, no. 24, p. 2201048, Jun. 2022, doi: https://doi.org/10.1002/adfm.202201048.

[3] M. Jin *et al.*, “Ferroelectrically modulated ion dynamics in Li+ electrolyte-gated transistors for neuromorphic computing,” *Appl. Phys. Rev.*, vol. 10, no. 1, p. 11407, Feb. 2023, doi: 10.1063/5.0130742.

[4] Y. H. Cho *et al.*, “Efficient Ionovoltaic Energy Harvesting via Water-Induced p–n Junction in Reduced Graphene Oxide,” *Adv. Sci.*, vol. n/a, no. n/a, p. 2404893, Aug. 2024, doi: https://doi.org/10.1002/advs.202404893.

Co-author

[1] C. Im *et al.*, “Excitatory postsynaptic current model for synaptic thin-film transistors,” *J. Appl. Phys.*, vol. 132, no. 4, p. 44503, Jul. 2022, doi: 10.1063/5.0101168.

[2] J. Kim *et al.*, “Solvent-assisted sulfur vacancy engineering method in MoS2 for a neuromorphic synaptic memristor,” *Nanoscale Horizons*, vol. 8, no. 10, pp. 1417–1427, 2023, doi: 10.1039/D3NH00201B.

[3] J. H. Lee *et al.*, “Cu2O p-type Thin-Film Transistors with Enhanced Switching Characteristics for CMOS Logic Circuit by Controlling Deposition Condition and Annealing in the N2 Atmosphere,” *ACS Appl. Electron. Mater.*, vol. 5, no. 2, pp. 1123–1130, Feb. 2023, doi: 10.1021/acsaelm.2c01589.

[4] J. Lee *et al.*, “Machine Learning Driven Channel Thickness Optimization in Dual-Layer Oxide Thin-Film Transistors for Advanced Electrical Performance,” *Adv. Sci.*, vol. 10, no. 36, p. 2303589, Dec. 2023, doi: https://doi.org/10.1002/advs.202303589.

[5] Y. H. Cho *et al.*, “Investigation of carrier density modulation in water motion-induced ionovoltaic electricity generation,” *Nano Energy*, vol. 118, p. 108982, 2023, doi: https://doi.org/10.1016/j.nanoen.2023.108982.

[6] J. C. Shin *et al.*, “Oxide Semiconductor Heterojunction Transistor with Negative Differential Transconductance for Multivalued Logic Circuits,” *ACS Nano*, vol. 18, no. 2, pp. 1543–1554, Jan. 2024, doi: 10.1021/acsnano.3c09168.

[7] H. Lee *et al.*, “Electrochemical Analysis of Ion Effects on Electrolyte-Gated Synaptic Transistor Characteristics,” *ACS Nano*, vol. 18, no. 7, pp. 5383–5395, Feb. 2024, doi: 10.1021/acsnano.3c10082.

[8] W. You *et al.*, “Machine Learning Strategy for Optimizing Multiple Electrical Characteristics in Dual-Layer Oxide Thin Film Transistors,” *ACS Appl. Mater. Interfaces*, Dec. 2024, doi: 10.1021/acsami.4c17179.

초록 (국문)

계면 쌍극자에 의한 이온 작동 인공 시냅스에서의 이온 동역학 제어

다수의 연구에서 전해질-게이트 트랜지스터가 아날로그 뉴로모픽 컴퓨팅(Neuromorphic Computing)을 위한 인공 시냅스의 유망한 후보로 주목받고 있으며, 이는 빠른 이온 반응, 낮은 에너지 소모, 유연 전자 기기에의 적용 가능성과 같은 우수한 특성 때문이다. 그러나 EGT는 인공 시냅스로서 중요한 한계점에 직면해 있다. 이는 순간적으로 인가된 전기장 하에서 이온의 이동이 급격하게 변화하는 현상 때문이다. 이러한 EGT의 고유한 특성은 장기 시냅스 가소성 특성이 떨어지고, 비선형적 및 비대칭적인 전기 전도도 변화를 나타내어 인공 시냅스로서의 실질적인 응용에 한계가 된다. 따라서, EGT 소자의 본질적인 문제를 해결하려면 이온 역학을 정밀하게 조절하기 위한 전기적 상호작용에 대한 종합적인 이해가 필요하다. 이에 본 연구에서는 EGT의 채널/전해질 계면에 쌍극자를 가진 중간층을 도입하여 양이온과의 쿨롱 상호작용을 통해 이온 역학을 정밀하게 제어하는 새로운 방법을 제안한다. 양이온과의 쿨롱 상호작용이 가능한 쌍극자 모멘트를 가진 유기 물질을 중간층으로 사용하며, (i) 플루오린화된 자기조립 단분자막(F-SAM)과 (ii) 강유전성 고분자가 그 사례이다.

첫째로, F-SAM은 이온 수용체로 도입되어, EGT의 채널/전해질

계면에서 양이온과 음전하를 띤 F-SAM 간의 강한 이온-쌍극자 상호작용을 유도한다. F-SAM이 도입된 EGT에서는 양이온이 계면에 효과적으로 포획되어, 거의 선형적이고 조정 가능한 다중 모드 도체 상태를 유지할 수 있다. 전기적 및 화학적 분석 결과, 플루오로알킬 사슬은 양이온과 플루오린화 탄소 간의 쿨롱 인력에 의해 채널-전해질 계면에서 순차적인 이온 포획을 가능하게 함을 확인하였다. 그 결과, F-SAM이 도입된 EGT의 전기 전도도의 비휘발성 특성이 향상되었으며, 높은 선형성과 대칭성을 갖춘 안정적이고 비휘발성의 채널 전도도 상태 변화를 나타내었다.

둘째로, PVDF-TrFE 강유전성 고분자를 채널/전해질 중간층으로 도입된 EGT를 제시하였다. PVDF-TrFE의 분극 된 강유전체 도메인은 계면에서 양이온의 이동을 촉진시켜 채널 내로의 양이온 침투를 용이하게 한다. 또한, 반대 방향으로 분극 된 도메인은 양이온이 채널에서 전해질로 다시 확산되는 것을 억제한다. 그 결과, 이러한 EGT는 흥분성 시냅스 후 전류(Excitatory postsynaptic current), 장기 시냅스 가소성(Long-Term Synaptic Plasticity), 그리고 거의 선형적인 전도도 가변을 포함한 필수적이며 우수한 시냅스 특성을 보여준다.

본 연구는 인공 시냅스와 뉴로모픽 컴퓨팅 시스템의 실용화를 위해 계면에서 이온 역학을 조절하는 새로운 방법론적 접근을 제시한다. 기존 연구들은 EGT를 인공 시냅스로 응용하는 것에 대해 탐구해왔으나, 이온 역학에 대한 근본적인 이해를 바탕으로 한 연구는 제한적이었다. 따라서

본 연구는 이온 역학 조절의 중요성을 강조하며, EGT를 인공 시냅스로 응용하기 위한 핵심 통찰을 제공하기 위해 이온과 전하 상호작용에 대한 종합적인 이해가 필수적임을 강조한다.

주요어: 뉴로모픽 컴퓨팅, 인공 시냅스, 전해질-게이트 트랜지스터, 이온-쌍극자 상호작용, 이온 역학